UNIVERSITY OF CALIFORNIA, MERCED

Model Systems of Dysregulated Metabolic States

by

Keedrian Isaac Olmstead

A dissertation submitted in partial satisfaction of the requirements for the degree of Doctor of Philosophy

in

Quantitative and Systems Biology

School of Natural Sciences

2021

Committee in charge:

Professor Chris T Amemiya, Advisor

Professor Katrina Hoyer, Chair

Professor Miriam Barlow

Professor Marcos E. García-Ojeda

The Dissertation of Keedrian Isaac Olmstead is approved, and it is acceptable in quality and form for publication on microfilm and electronically:

_____

Professor Chris T Amemiya, Advisor

_____

Professor Miriam Barlow

_____

Professor Marcos E. García-Ojeda

_____

Professor Katrina Hoyer, Chair

University of California, Merced

2021

This work is the culmination of my studies and labor, and as such it was only possible with the help of everyone who supported me in my journey.

My parents, Dr Thomas Olmstead and Dr Kay Olmstead, were the first to inspire me to follow a career in science. Their constant encouragement and advice throughout the years was immeasurably helpful, and their example was a bright star to strive for.

My initial advisor, Dr Fabian Filipp, saw potential in me first as an undergraduate intern and then as a graduate student. His mentorship enabled me to reach these heights, and his leadership taught me lessons not soon to be forgotten. My final advisor, Dr Chris T Amemiya, helped me navigate a turbulent transition, and it is only because of his aid that I did not fall through the cracks.

My thesis committee members, Dr Katrina Hoyer, Dr Marcos E. García-Ojeda, and Dr Miriam Barlow, helped structure my thoughts and writings into a coherent opus, and challenged me where I was weak. I am a better scientist because of their guidance.

My fellow graduate students and other members of the Systems Biology and Cancer Metabolism group gave me the joy, friendship, and camaraderie that empowered me to persevere in my studies. Without them, the path would have been cheerless, and one I likely would not have completed.

Finally, my spouse, James York, provided a deep well of emotional support that kept me going in my darkest days.

Table of Contents

Acknowledgements vii
Curriculum Vita ix
Abstract xi
Chapter One: Introduction 1
1.1 Overview of metabolism 1
1.2 Dysregulated metabolism states: Warburg effect 1
1.3 Dysregulated metabolism states: diabetes 2
1.4 Dysregulated metabolism states: long-term fasting 3
1.5 In summary 3
1.5 References 5
Chapter Two: Methodology 7
2.1 Cell culture 7
2.2 Animal studies (Northern elephant seals) 11
2.3 Metabolomics 12
2.4 Statistical analyses 16
2.5 Transcriptome profiling of Huh7 and Huh7-*GCK*$^{+}$/*HK2*$^{-}$ cell lines 18
2.6 References 19
Chapter Three: Insulin induces a shift in lipid and primary carbon metabolites in a model of fasting-induced insulin resistance 23
Abstract 23
3.1 Introduction 24
3.2 Methods 25
3.3 Results 30
3.4 Discussion 32
3.5 Significance Statement 37
3.6 Supplementary Material 37
3.7 Acknowledgments 37
3.8 References 39
Chapter Four: A hexokinase isoenzyme switch in human liver cancer cells promotes lipogenesis and enhances innate immunity 52
Abstract 52
4.1 Introduction 53
4.2 Results 54
4.3 Discussion 57

4.4 Methods 59
4.5 Data availability 64
4.6 Acknowledgements 64
4.7 References 66
Chapter Five: Conclusions 83
5.1 Summary of contributions 83
5.2 Insulin induces a shift in lipid and primary carbon metabolites in a model of fasting-induced insulin resistance 83
5.3 A hexokinase isoenzyme switch in human liver cancer cells promotes lipogenesis and enhances innate immunity 87
5.4 Conclusions 90
5.5 References 92

Acknowledgements

Chapter One: Introduction

I thank Dr Miriam Barlow for her advice and support when this chapter was written.

This chapter was supported by Graduate Student Researcher funds from the University of California, Merced, School of Natural Sciences to K.O.

Chapter Two: Methodology

This chapter was supported by Graduate Student Researcher funds from the University of California, Merced, School of Natural Sciences to K.O.

Chapter Three: Insulin induces a shift in lipid and primary carbon metabolites in a model of fasting-induced insulin resistance

The text of this chapter is a reprint of the material as it appears in the journal *Metabolomics*. Originally published in *Metabolomics*. Keedrian Olmstead, Michael R La Frano, Johannes Fahrmann, Dmitry Grapov, José A Viscarra, John W Newman, Oliver Fiehn, Daniel E Crocker, Fabian V Filipp, Rudy M Ortiz. Insulin induces a shift in lipid and primary carbon metabolites in a model of fasting-induced insulin resistance. *Metabolomics*. 2017;13(5):60. PMID: 28757815. Copyright © 2017 Springer Nature Group.

This work was supported by a National Institutes of Health National Heart, Lung, and Blood Institute Supplement to Support Diversity (R01HL09176-S) to J.A.V., the N.I.H. N.H.L.B.I. Career Development Award (K02HL103787) to R.M.O., grant CA154887 from the National Institutes of Health, National Cancer Institute, University of California, Cancer Research Coordinating Committee CRN-17-427258, National Science Foundation, University of California Senate Graduate Research Council, and Health Science Research Institute program grants to F.V.F., USDA Intramural Project 2032-51530-022-00D to J.W.N., N.I.H. N.H.L.B.I. grant R01HL09176, and N.I.H. West Coast Metabolomics Center grant U24 DK097154.

Chapter Four: A hexokinase isoenzyme switch in human liver cancer cells promotes lipogenesis and enhances innate immunity

The text of this chapter is a partial reprint of the material as it appears in the journal *Communications Biology*. Originally published in *Communications Biology*. Laure Perrin-Cocon, Pierre-Olivier Vidalain, Clémence Jacquemin, Anne Aublin-Gex, Keedrian Olmstead, Baptiste Panthu, Gilles Jeans Philippe Rautureau, Patrice André, Piotr Nyczka, Marc-Thorsten Hütt, Nivea Amoedo, Rodrigue Rossignol, Fabian V Filipp, Vincent Lotteau, Olivier Diaz. Hexokinase

isoenzyme switch in human liver cancer cells promotes lipogenesis and enhances innate immunity. *Communications Biol*. 2021;4(1):217. PMID: 33594203.

This work was supported by grants CA154887, GM115293, CRN-17-427258, NSF GRFP, and the Science Alliance on Precision Medicine and Cancer Prevention by the German Federal Foreign Office, implemented by the Goethe-Institute, Washington, DC, USA, and supported by the Federation of German Industries (BDI), Berlin, Germany, to F.V.F., as well as the Fondation pour la Recherche Médicale (FRM) grant DEQ20160334893 to V.L., and Graduate Student Researcher funds from the University of California, Merced, School of Natural Sciences and the QSB Summer Research Fellowship to K.O.

Chapter Five: Conclusions

This chapter was supported by Graduate Student Researcher funds from the University of California, Merced, School of Natural Sciences to K.O.

Curriculum Vita

Keedrian Olmstead

Education and Research

2010 – 2013	Bachelor of Science, Molecular and Cell Biology University of California, Merced School of Natural Sciences
2012	Bachelor of Science (semester abroad) University of Copenhagen Department of Biology
2012	Research intern Tocagen, Inc, R&D Group
2013	Undergraduate researcher University of California, Merced School of Natural Sciences Laboratory of Dr Fabian Filipp
2014	Graduate student researcher Lawrence Berkeley National Laboratory Joint Genome Institute Laboratory of Dr Axel Visel
2014 – 2020	Doctor of Philosophy, Quantitative and Systems Biology University of California, Merced School of Natural Sciences Laboratory of Dr Fabian Filipp
2020 – 2021	Doctor of Philosophy, Quantitative and Systems Biology University of California, Merced School of Natural Sciences Laboratory of Dr Chris T Amemiya

Grants, fellowships, and awards

2014 – 2020	Teaching Assistant University of California, Merced School of Natural Sciences
2018	QSB Summer Research Fellowship University of California, Merced

2019 QSB Summer Research Fellowship
University of California, Merced

Publications and presentations

Olmstead K, La Frano M, Fahrmann J, et al. Metabolic shift in response to fasting and insulin infusion in a large mammalian model of insulin resistance. Abstract presented as a poster at the Metabolomics Society Annual Conference (2015). Burlingame, CA.

Hung S, Olmstead K, La Frano M, Newman J, Ojcius D, Filipp FV. Oxylipin epoxide-mediated inflammatory response to *Fusobacterium nucleatum* infection in gingival epithelial cells. Abstract presented as a poster at Southern California Systems Biology Conference (2016). Irvine, CA.

Olmstead K, La Frano M, Fahrmann J, Grapov D, Viscarra JA, Newman J, Fiehn O, Crocker DP, Filipp FV, Ortiz RM. Insulin induces a shift in lipid and primary carbon metabolites in a model of fasting-induced insulin resistance. *Metabolomics*. 2017;13(5):60. PMID: 28757815

Perrin-Cocon L, Vidalain P, Jacquemin C, Aublin-Gex A, **Olmstead K**, Panthu B, Rautureau GJP, André P, Nyczka P, Hütt M, Amoedo N, Rossignol R, Filipp FV, Lotteau V, Diaz O. Hexokinase isoenzyme switch in human liver cancer cells promotes lipogenesis and enhances innate immunity. *Communications Biol*. 2021;4(1):217. PMID: 33594203

Abstract

Model Systems of Dysregulated Metabolic States

by Keedrian Isaac Olmstead

Doctor of Philosophy in Quantitative and Systems Biology
University of California, Merced, 2021
Professor Katrina Hoyer, Committee Chair

Dysregulated metabolic states in human health are linked to chronic conditions such as diabetes, insulin resistance, and cancer, and can even impair immune function. Studying dysregulated metabolic states is a critical aspect in current biomedical research, as an aging population and a rise in emerging infectious diseases means that the prevention and management of these conditions is more important than ever. However, metabolism is a highly complex physiological phenomenon that is often inextricable in a practical sense from other systems such as immune function or hormone signaling. Therefore, models of altered metabolism are extremely useful for examining the effects of such perturbed metabolic states in comparative isolation, to elucidate the nature, role, and consequences of such states.

This dissertation presents two examples of model systems that can be used to investigate dysregulated metabolism. The first is the Northern elephant seal, which undergoes temporary, reversible, tissue-specific insulin resistance while it fasts as a normal part of its life cycle. The large-scale shifts in substrate utilization and insulin response observed during long-term fasting in the elephant seal indicate that it can be used to untangle some of the questions about the evolution and regulation of insulin signaling, and provide significant answers to addressing insulin resistance in a clinical context. The second is an engineered cellular model in hepatocellular carcinoma (HCC) cells, examining the hexokinase enzyme switch. As hepatocytes transform into HCC cells during carcinogenesis, they undergo a shift from GCK to HK2 as the main hexokinase enzyme catalyzing the initial step in glycolysis. A unique cellular model was generated by knocking out HK2 in Huh7 HCC cells while simultaneously restoring HK4 expression, thus reversing the isoenzyme switch. The Huh7-*GCK*$^{+}$/*HK2*$^{-}$ cell line displayed a rewired metabolic network, and restored metabolic functions of normal hepatocytes such as lipogenesis and VLDL secretion. It also displayed increased innate immune response and sensitivity to NK cells, indicating the wide-ranging effects of the isoenzyme switch.

Both approaches of model systems – identifying existing organisms with unique metabolic states and engineering specific cellular models – are explored in this work as an overview of the tools available to researchers in studying dysregulated metabolic states.

Chapter One: Introduction

1.1 Overview of metabolism

The classical understanding of central carbon metabolism in eukaryotic cells begins with glucose being imported to the cytosol by glucose transport proteins. In the cytosol, glucose is broken down into pyruvate through glycolysis, producing reduced nicotinamide adenine dinucleotide (NADH) and adenosine triphosphate (ATP)[1]. Pyruvate is converted to acetyl-CoA, which enters the tricarboxylic acid cycle (TCA cycle) in the mitochondrial matrix. The TCA cycle completes the oxidation of the carbon atoms, releasing them as carbon dioxide, and generating NADH, ATP, and reduced flavin adenine dinucleotide ($FADH_2$)[2]. The high-energy electrons carried by NADH and $FADH_2$ are fed into the electron transport chain (ETC), which pumps protons across the inner mitochondrial membrane, producing a proton gradient that is harnessed by ATP synthase to generate large amounts of ATP. The entire process, from glycolysis to ETC, generates a total of 36-38 molecules of ATP per molecule of glucose[3].

However, this simple framework belies the dynamic complexity of the metabolic network. Many of these reactions are reversible, so the direction of flux is not fixed. Additionally, the enzymes that catalyze the reactions are regulated both in their level of activity and their substrate specificity[4]. Most importantly, pathways for biosynthesis feed into and out of the pathways for energy generation at several key points, connecting these two cellular functions inextricably. Key metabolic enzymes can also have secondary roles in seemingly unrelated processes such as nuclear gene expression[5] or apoptosis[6]. Thus, when the metabolic network is dysregulated, the consequences are multifaceted.

1.2 Dysregulated metabolism states: Warburg effect

One of the most significant examples of dysregulated metabolism is the Warburg effect. Since the 1920s, it has been known that cancer cells express a unique metabolic state wherein the vast majority of glucose uptake is diverted to lactate fermentation after glycolysis, instead of the TCA cycle[7]. Pyruvate, instead of conversion to acetyl-CoA, undergoes conversion to lactate via a reducing process that also oxidizes NADH to NAD^+, thus replenishing the pool of NAD^+ that can be used for glycolysis. Without the TCA cycle and ETC, the combined processes of glycolysis and fermentation only produce 2 ATP per molar equivalent of glucose. In an apparent paradox, rapidly proliferating cancer cells, with their increased bioenergetic requirements, preferentially utilize a metabolic pathway that suffers a more than 18-fold reduction in efficiency.

The shift to glycolysis, however, allows the cell to divert TCA intermediates towards other pathways of biosynthesis, generating the building blocks to support rapid proliferation. Citrate is exported from the TCA cycle to serve as a building block for fatty acids which will ultimately become membrane lipids,

whereas amino acids like aspartate are derived from TCA intermediates. In order to replenish TCA intermediates, the cell upregulates the import of glutamine, which is deamidated to glutamate and then converted into α-ketoglutarate. The energetic inefficiency of glycolysis, meanwhile, is compensated by a dramatic upregulation of glucose uptake and glycolytic enzyme activity, resulting in much higher flux through the glycolysis pathway and thus faster production of ATP than might otherwise be expected.

This thorough reprogramming of cellular metabolism is so well associated with cellular malignancy that it is now considered one of the eight hallmarks of cancer[8]. However, in the century following Warburg's observations, it has been established that other, rapidly proliferating and non-malignant cell populations such as stem cells[9,10] and activated lymphocytes[11] also exhibit similar metabolism. This further supports the theory that this altered metabolism is a distinct metabolic state that promotes a replicative phenotype, rather than a consequence of defective mitochondria, as theorized by Warburg[12].

1.3 Dysregulated metabolism states: diabetes

In mammals, insulin is a hormone that has widespread effects on both cellular and whole-body metabolism. Insulin signaling promotes uptake of circulating glucose by liver, fat, and skeletal muscle cells. Insulin further promotes anabolic processes in these cells such as lipid synthesis and amino acid uptake, while inhibiting catabolic processes such as proteolysis, lipolysis, and autophagy. Type 2 diabetes is a metabolic disorder wherein insulin signaling is impaired due to low insulin secretion, insulin resistance in target tissues, or both. This causes high amounts of circulating glucose, as well as upsetting the expected patterns of metabolism in the peripheral tissue cells.

Insulin is secreted by β-cells in the pancreas in response to circulating glucose[13]. β-cells are highly sensitive to circulating glucose concentrations, and respond to glucose by upregulating glycolysis. A high concentration of mitochondrial shuttles ensures that most of the glycolytic output is funneled into the mitochondria for the TCA cycle and eventually oxidative phosphorylation. The high concentrations of ATP produced by mitochondrial respiration leads to the closure of ATP-sensitive K^+ channels, resulting in membrane depolarization and the opening of voltage-gated Ca^{2+} channels. The influx of Ca^{2+} ions stimulates exocytosis of insulin granules into the bloodstream[14]. Inhibition of oxidative phosphorylation blocks glucose-stimulated insulin secretion, indicating a link between mitochondrial function and insulin secretion[15]. In the β-cells of diabetic mice, glucose utilization is reduced at every stage, including glycolysis, the TCA cycle, and the ETC[16]. Peripheral tissues also face dysregulated metabolism in diabetes. Skeletal muscle cells exhibit downregulation in genes associated with glycolysis, the TCA cycle, and lipolysis in diabetic patients[17].

1.4 Dysregulated metabolism states: long-term fasting

During periods of fasting in humans (and mammals in general), whole-body metabolism shifts from a reliance on glucose to a reliance on lipids, and later protein as starvation continues[18]. Increased lipolysis in adipose tissue leads to higher concentrations of free fatty acids in circulation, to be utilized by the liver for gluconeogenesis[19]. Insulin and insulin signaling are thus repressed during fasting[20] as a part of this rewiring of metabolism. Skeletal muscle, in particular, is associated with insulin resistance in starvation, as it is the tissue most responsible for insulin-induced glucose uptake[21].

However, Northern elephant seals undergo a 3-month fast as part of their maturation from pups. During this fasting period, they rely exclusively on lipid oxidation, utilizing fat stores built up from the nursing period. Research indicates that, unlike the human model of starvation, Northern elephant seals exhibit whole-body insulin resistance, but maintain insulin sensitivity in skeletal muscle tissue[22]. Insulin resistance in adipose tissues allows for continued adipose secretion of fatty acids into circulating plasma, while insulin sensitivity in skeletal muscle may be an adaptation to prevent unnecessary proteolysis. This tissue-specific insulin resistance phenotype is then reversible, resulting in normal insulin sensitivity after the seals' fast ends. Elucidating the mechanisms behind the regulation of temporary, tissue-specific, and reversible insulin resistance in Northern elephant seals may lead to breakthroughs in the treatment of type 2 diabetes and other human metabolic disorders, in which chronic insulin resistance contributes to the pathological condition.

1.5 In summary

The dysregulated metabolism states illustrated above show that, although the cellular metabolic network is dynamic and robust, it can be distorted into alternate versions with distinct substrate preferences and outputs. Such permutations are usually a consequence of acute or systemic injurious conditions, and the dysregulated metabolic state can then further influence progression of organismal syndromes, which is especially seen in cancer[23,24] and diabetes[25]. As current biomedical research becomes increasingly more focused on the prevention and management of chronic health conditions, it thus becomes more important than ever to have in the scientist's toolbox an array of model systems with which to interrogate the dysregulated metabolism that underlies so many of those conditions. The ability to replicate an altered metabolic network allows for the study of its functions and mechanisms and the testing of novel treatments and inhibitors. The following chapters of this dissertation will outline two classes of model systems for dysregulated metabolism and discuss their use.

The Northern elephant seal, as mentioned previously, displays unique metabolic plasticity, characterized by transient, reversible, tissue-specific insulin resistance. This makes it useful as a model system to study the onset, progression, and nature of insulin resistance in a clinical setting as it relates to human obesity and diabetes. The elephant seal can be taken as an example of

an organism selected to be a model system because of its biological properties, and this approach is highlighted in Chapter Three.

Mutation in cancer cells is a complex and serpentine process, so each instance of tumorigenesis represents a *sui generis* genotype. There are, however, common mutational events that occur, especially within cancer types. Hepatocellular carcinoma (HCC), or cancer of the liver, is often characterized by a preferential switch from GCK to HK2 as the main isoform of the enzyme initiating glycolysis. This isoenzyme switch has knock-on effects throughout the cell that contribute to cancer progression in perhaps unusual areas. In order to study these consequences, I present an engineered cellular model wherein HK2 is knocked out and GCK expression restored, thus reversing the isoenzyme switch. The use of engineered cellular models to investigate extremely specific metabolic perturbations is explored in Chapter Four.

Both of these examples serve to test the hypothesis that the choice of model system is instrumental in obtaining high-quality data on a particular disorder of dysregulated metabolism. Multifaceted, multi-organ disorders such as diabetes, insulin resistance, and dyslipidemia are best studied with animal models specially suited for the condition in question, whereas more specific metabolic perturbations, such as single mutations found in cancer or genetic diseases, can be studied in comparative isolation, using engineered cellular models. Using an inappropriate model system may overly complicate method development or even lead to irrelevancy in the data generated. In Chapter Five, the two approaches are compared.

1.5 References

1. Bolaños JP, Almeida A, Moncada S. Glycolysis: a bioenergetic or a survival pathway? *Trends Biochem Sci*. 2010;35(3):145-9. PMID: 20006513.

2. Akram M. Citric acid cycle and role of its intermediates in metabolism. *Cell Biochem Biophys*. 2014;68(3):475-8. PMID: 24068518.

3. Watt IN, Montgomery MG, Runswick MJ, Leslie AGW, Walker JE. Bioenergetic cost of making an adenosine triphosphate molecule in animal mitochondria. *Proc Natl Acad Sci USA*. 2010;107(39):16823-7. PMID: 20847295.

4. Hung YP, Teragawa C, Kosaisawe N, et al. Akt regulation of glycolysis mediates bioenergetic stability in epithelial cells. *eLife*. 2017;6:e27293. PMID: 29239720.

5. Yang, J, Ren B, Yang G, et al. The enhancement of glycolysis regulates pancreatic cancer metastasis. *Cell Mol Life Sci*. 2020;77(2):305-321. PMID: 31432232.

6. Ow YP, Green DR, Hao Z, Mak TW. Cytochrome c: functions beyond respiration. *Nat Rev Mol Cell Biol*. 2008;9(7):532-42. PMID: 18568041.

7. Warburg O, Posener K, Negelein E. The metabolism of cancer cells. *Biochem Z*. 1924;152(1):319-344.

8. Hanahan D, Weinberg RA. Hallmarks of cancer: the next generation. *Cell*. 2011;144(5):646-74. PMID: 21376230.

9. Ochocki JD, Simon MC. Nutrient-sensing pathways and metabolic regulation in stem cells. *J Cell Biol*. 2013;203(1):23-33. PMID: 24127214.

10. Shyh-Chang N, Daley GQ, Cantley LC. Stem cell metabolism in tissue development and aging. *Development*. 2013;140(12):2535-47. PMID: 23715547.

11. Donnelly RP, Finlay DK. Glucose, glycolysis and lymphocyte responses. *Mol Immunol*. 2015;68(2 Pt C):513-9. PMID: 26260211.

12. Warburg O. On the origin of cancer cells. *Science*. 1956;123(3191):309-14. PMID: 13298683.

13. Maechler P, Wollheim CB. Mitochondrial function in normal and diabetic β-cells. *Nature*. 2001;414(6865):807-12. PMID: 11742413.

14. Rorsman P, Ashcroft FM. Pancreatic β-cell electrical activity and insulin secretion: Of mice and men. *Physiol Rev*. 2017;98(1):117-214. PMID: 29212789.

15. Prentki M, Matschinsky FM, Madiraju SRM. Metabolic signaling in fuel-induced insulin secretion. *Cell Metab*. 2013;18(2):162-85. PMID: 23791483.

16. Haythorne E, Rohm M, van de Bunt M, et al. Diabetes causes marked inhibition of mitochondrial metabolism in pancreatic β-cells. *Nat Commun*. 2019;10(1):2474. PMID: 31171772.

17. Patti ME, Butte AJ, Crunkhorn S, et al. Coordinated reduction of genes of oxidative metabolism in humans with insulin resistance and diabetes: Potential role of PGC1 and NRF1. *Proc Natl Acad Sci USA*. 2003;100(14):8466-71. PMID: 12832613.

18. Cahill GF Jr. Starvation in man. *N Engl J Med*. 1970;282(12):668-75. PMID: 4915800.

19. Boden G. Effects of free fatty acids on gluconeogenesis and glycogenolysis. *Life Sci*. 2003;72(9):977-88. PMID: 12495777.

20. DeFronzo R, Soman V, Sherwin RS, Hendler R, Felig P, et al. Insulin binding to monocytes and insulin action in human obesity, starvation, and refeeding. *J Clin Invest*. 1973;62(1):204-13. PMID: 350903.

21. Moller DE, Chang PY, Yaspelkis BB III, Flier JS, Wallberg-Henriksson H, Ivy JL. Transgenic mice with muscle-specific insulin resistance develop increased adiposity, impaired glucose tolerance, and dyslipidemia. *Endocrinology*. 1996;137(6):2397-405. PMID: 8641192.

22. Viscarra JA, Ortiz RM. Cellular mechanisms regulating fuel metabolism in mammals: Role of adipose tissue and lipids during prolonged food deprivation. Metabolism. 2013;62(7):889-97. PMID: 23357530.

23. Chang C, Qiu J, O'Sullivan D, et al. Metabolic competition in the tumor microenvironment is a driver of cancer progression. *Cell*. 2015;162(6):1229-41. PMID: 26321679.

24. Yang W, Xia Y, Ji H, et al. Nuclear PKM2 regulates β-catenin transactivation upon EGFR activation. *Nature*. 2011;480(7375):118-22. PMID: 22056988.

25. Hameed I, Masoodi SR, Mir SA, Nabi M, Ghazanfar K, Ganai BA. Type 2 diabetes mellitus: From a metabolic disorder to an inflammatory condition. *World J Diabetes*. 2015;6(4):598-612. PMID: 25987957.

Chapter Two: Methodology

2.1 Cell culture

Investigation of dysregulated metabolism in cancer was accomplished with *in vitro* cell cultures of cancer-derived cell lines.

2.1.1 Cell culture

Cell cultures were tested negative for mycoplasma contamination by PCR (mycoplasma check, eurofins). Huh7 cells were authenticated by Eurofins Medigenomix Forensik GmbH using PCR-single-locus-technology. 21 independent PCR-systems Amelogenin, D3S1358, D1S1656, D6S1043, D13S317, Penta E, D16S539, D18S51, D2S1338, CSF1PO, Penta D, TH01, vWA, D21S11, D7S820, D5S818, TPOX, D8S1179, D12S391, D19S433 and FGA (Promega, PowerPlex 21 PCR Kit) were investigated to determine their genetic characteristics. Huh7 cells and derivatives were grown as previously described in DMEM, 10% fetal calf serum (FCS), penicillin/streptomycin, 1 mM pyruvate, 2mM L-glutamine. Culture medium and additives were from Gibco except FCS (Dominique Dutcher).

2.1.2 Establishing novel cell lines

Huh7 cells (15×10^4) were transduced for GCK expression at different multiplicities of infection (lentiviral transduction using the pLEX-GCK construct). The Huh7-*GCK*$^+$/*HK2*$^+$ cells were then cultured for 7 days with puromycin (1 µg/mL) before amplification. HK2 knock-out was achieved using the CRISPR/Cas9 system as previously described[1] to obtain Huh7-*GCK*$^+$/*HK2*$^-$ cells. Briefly, a single guide RNA (sgRNA) pair was designed for double nicking using the CRISPR Design Tool (http://tools.genome-engineering.org). The guide sequence oligos (sgRNA$_1$(*HK2*): 5'-CACCGTGACCACATTGCCGAATGCC-3' and sgRNA$_2$(*HK2*): 5'-CACCGTTACCTCGTCTAGTTTAGTC-3') were cloned into a plasmid containing sequences for Cas9 expression and the sgRNA scaffold (pSpCas9(BB)-2A-GFP, Addgene plasmid #48138). 48 h post-transfection, cells were sorted by FACS based on the transient expression of GFP and cloned by limiting dilution. Effective deletion of HK2 was assessed by qPCR.

For *HK2* knock-down, Huh7-*GCK*$^+$/*HK2*$^+$ cells were transduced with lentiviral vectors expressing HK2-targeting shRNAs, and antibiotic selection was applied (hygromycin; 100 µg/ml). The *HK2*-targeting sequence 5'-CCGGCCAGAAGACATTAGAGCATCTCTCGAGAGATGCTCTAATGTCTTCTGGTTTTTT-3' was cloned in the pLKO.1 hygro vector (a gift from Bob Weinberg; Addgene plasmid #24150). HK2 expression in Huh7-GCK+/HK2+ and Huh7-*GCK*$^+$/*HK2*$^-$Sh was analyzed on cell lysates by western blotting.

2.1.3 Enzymatic activity assays

Cells were trypsinized, washed twice, and cell pellets were stored at −80°C. Protein extractions and assays were performed in specific buffers for hexokinase and pyruvate carboxylase assays as described below.

2.1.3.1 Hexokinase activity assay

The method used for monitoring HK activity in cells lysates was adapted from Kuang et al.[2-4] Cellular pellets stored at −80°C were thawed and immediately homogenized (2×10^6 cells/100 µl) in precooled reaction buffer (0.05 M Tris–HCl, 0.25 M sucrose, 0.005 M EDTA, 0.005 M 2-mercaptoethanol, pH = 7.4). After 20 min incubation on ice, homogenates were pulse-sonicated 15 s at half power (EpiShear Probe Sonicator). Homogenates were then centrifuged at 500 g for 20 min at 4 °C. Supernatants were immediately used for determination of HK activity, which was measured spectrophotometrically through $NADP^+$ reduction in the glucose 6-phosphate dehydrogenase-coupled reaction. HK activity was assayed in medium containing 50 mM triethanolamine (pH = 7.6), 10 mM $MgCl_2$, 1.4 mM $NADP^+$, with variable concentration of glucose and 1 U glucose 6-phosphate dehydrogenase (*S. cerevisiae*), equilibrated to 37 °C. The reaction was started by addition of ATP (final concentration 1.9 mM), and absorbance was continuously recorded for 30 min at 340 nm (TECAN Infinite M200).

2.1.3.2 Pyruvate carboxylase activity assay

The method used for quantification of PC activity was adapted from Payne et al.[5] Briefly, cells were centrifuged, washed twice with ice-cold PBS before homogenization in Tris-HCL 100 mM, pH = 8.0 using a Dounce homogenizer. Homogenates were pulse-sonicated 15 s at half power (EpiShear Probe Sonicator) before centrifugation at 500 g for 5 min. Supernatants were immediately used for the assay. PC activity was assayed in medium containing 100 mM Tris-HCl, 50 mM $NaHCO_3$, 5 mM $MgCl_2$, 0.1 mM Acetyl-CoA, 0.25 mM 6,6'-Dinitro-3,3'-dithiodibenzoic acid (DTNB), 5 mM ATP, 5 mM pyruvate, citrate synthase and cofactors. Reduction of DTNB by the generated free CoA was measured continuously by Abs at 412 nm and recorded for 30 min (TECAN Infinite M200). The same assay was performed in absence of pyruvate to subtract background signal.

2.1.4 Cell migration assay

Cells (2×10^4) were plated in the upper chamber of transwells (Sarstedt, PET 8.0-µm, TL - 833932800) with DMEM without FCS to allow migration for 24 h at 37 °C. DMEM with 10% FCS was distributed in each well, below the chamber. Chambers were gently picked up before a brief PBS rinse and 0.05% crystal violet coloration. The migrated cells were analyzed a Leica M50 microscope using a magnification factor of 20x. The number of cells that have migrated through the membrane and attached on the underside of the membrane were counted using the software Image J.

2.1.5 Intracellular lipid staining

For fluorescence microscopy staining of intracellular lipids, cells were seeded and cultured during 48 h before staining with Oil-Red-O. Cells were fixed 15 min at RT with a 4% formaldehyde solution, washed twice with water before a 5 min incubation with isopropanol 60%. Isopropanol was then removed and Oil-Red-O solution (Millipore Sigma-Aldrich) added on cells for 15 min at RT. Cells were then extensively washed with water to remove the exceeding dye before nucleus counterstaining with NucBlue Fixed Cell Stain ReadyProbes reagent (ThermoFisher Scientific) and observation with a Nikon Eclipse Ts2R microscope (x60). For the quantification of intracellular lipid droplets by flow cytometry, cells were stained with the BODIPY® 493/503 dye (Tocris BioTechne) after 48 h of culture. The cells were washed with PBS before being incubated for 5 min with a 5 µM BODIPY solution in PBS at 37 °C. Cells were then washed with PBS before trypsination and FACS analysis. A 7-AAD (BioLegend) staining of dead cells, prior to FACS analysis, allowed gating on living cells.

2.1.6 Protein, ApoB, and lipid quantification

Protein concentration was determined using the DC Protein Assay (Bio-Rad). ApoB concentration in medium and gradients fractions was determined by ELISA as previously described[6]. Total concentrations of cholesterol, phospholipids, and triglycerides (TG) were determined using specific assays from Millipore Sigma-Aldrich (ref. MAK043, MAK122 and MAK266 respectively). Free Fatty Acids were quantified using a specific assay kit from Abcam (ref. ab65341).

2.1.7 Western-blot analysis

Cell lysates from 10^6 cells were prepared in lysis buffer (1% Triton X-100, 5 mM EDTA in PBS with 1% protease inhibitor cocktail (P8340; Millipore Sigma-Aldrich) and 2 mM orthovanadate). After elimination of insoluble material, proteins were quantified, separated by SDS-PAGE and analyzed by western-blot on PVDF membrane. After saturation of the PVDF membrane in PBS-0.1% Tween 20 supplemented with 5% (w/v) non-fat milk powder, blots were incubated 1 h at room temperature with primary antibody in PBS-0.1% Tween 20 (1:2,000 dilution for all antibodies unless specified otherwise). Incubation with secondary antibody was performed after washing for 1 h at room temperature. HRP-labeled anti-goat (Santa Cruz Biotechnology), anti-rabbit (A0545, Millipore Sigma-Aldrich) or anti-mouse (Jackson ImmunoResearch Laboratories) antibodies were diluted 20,000-fold and detected by enhanced chemiluminescence reagents according to the manufacturer's instructions (SuperSignal Chemiluminescent Substrate, Thermo Fisher Scientific). Primary antibodies used for immunoblotting included mouse monoclonal antibody against human GCK (clone G-6, Santa Cruz Biotechnology), rabbit monoclonal antibody against human HK2 (Clone C64G5, Cell Signaling Technology), rabbit monoclonal antibody against human HK1 (C35C4, Cell Signaling), rabbit polyclonal antibody against human HK3 (HPA056743, Millipore Sigma-Aldrich), goat polyclonal antibody against human ACLY (SAB2500845, Millipore Sigma-Aldrich), rabbit polyclonal antibody against human pACLY (phospho S455, Cell

Signaling Technology), rabbit monoclonal antibody against human PDH α1 subunit (C54G1, Cell Signaling Technology), rabbit monoclonal antibody against human pPDH E1-alpha subunit (phosphor S293, Abcam), goat polyclonal antibody against human PC (SAB2500845, Millipore Sigma-Aldrich), rabbit monoclonal antibody against human GAPDH (D16H11, Cell Signaling Technology) and rabbit polyclonal antibody against human HIF-1α (NB100-134, Novus Biologicals; 1:500 dilution).

2.1.8 Respiration assay

Twenty-four hours prior measuring respiration in the Extracellular Flux Analyzer (Seahorse Bioscience), cells were seeded in XF 24-well cell culture microplates (Seahorse Bioscience) at 5×10^4 cells/well in 100 µL of DMEM medium supplemented with 10% FCS, 1 mM pyruvate, 2 mM L-glutamine, penicillin/streptomycin, and then incubated at 37 °C/5% CO_2 during 5 h for cell attachment. Medium volume was adjusted to 250 µL and cells incubated overnight. The assay was initiated by removing the growth medium from each well and replacing it with 500 µL of Seahorse assay medium (XF DMEM pH = 7.4 + 10 mM Glucose, 2 mM Glutamine and 1 mM sodium pyruvate) prewarmed at 37 °C. Cells were incubated at 37 °C for 1 h to allow media temperature and pH to reach equilibrium before the first measurement. The oxygen consumption rate (OCR) was measured using the following Seahorse running program: injection Port A – 1.5 µM Oligomycin; Injection Port B – 0.5 µM FCCP and injection Port C – 0.5 µM Rotenone; injection port D – 0.5 µM Antimycin A. The number of cells was determined at the end of the run after Hoechst staining and cell counting using Cytation 1 imaging reader (Biotek).

2.1.9 RLR stimulation

Cells were seeded in 96-well or 24-well plates. After 24 h, cells were co-transfected with indicated doses of the RIG-I ligand 3p-hpRNA or the MDA5/TLR3 ligand poly(I:C) HMW together with the pISRE-luc (1.25 µg/ml; Stratagene) and pRL-SV40 (0.125 µg/ml; Promega) reporter plasmids using the JetPEI-Hepatocyte reagent (Polyplus Transfection). Manufacturer's instructions were followed. After 48 h, supernatants were collected for cytokine quantification. Firefly and Renilla luciferase expressions within cells were determined using the Dual-Glo luciferase Assay system (Promega) and an Infinite M200 microplate reader (TECAN).

2.1.10 Cytokine assays

Clarified culture supernatants were collected and stored at −20 °C. IL-8 was quantified using the Cytometric Bead Array for human IL-8 (BD Biosciences). Other cytokines were assayed using the LEGENDplex multiplex assay (Human Anti-Virus Response Panel, BioLegend). Fluorescence was analyzed using a FACS Canto II (BD Biosciences).

2.1.11 Human NK cell purification

NK cells were isolated from human buffy coats of healthy donors obtained from the Etablissement Français du Sang. Informed consent was obtained from donors and experimental procedures were approved by the local institutional

review committee. PBMCs were isolated by standard density gradient centrifugation on Ficoll-Hypaque (Eurobio). Mononuclear cells were separated from peripheral blood lymphocytes (PBLs) by centrifugation on a 50% Percoll solution (GE Healthcare). NK cells were purified from PBLs by immunomagnetic depletion using pan-mouse IgG Dynabeads (Thermo Fisher Scientific) with a cocktail of depleting monoclonal antibodies: anti-CD19 (4G7 hybridoma), anti-CD3 (OKT3 hybridoma, ATCC, Manassas, VA, USA), anti-CD4, anti-CD14 and anti-glycophorin A (all from Beckman Coulter). NK purity was >70% as assessed by CD56 labeling.

2.1.12 NK cell cytotoxicity test

Huh7 or Huh7-*GCK*$^{+}$/*HK2*$^{-}$ were seeded at 1×10^{5} cells per well in a 24-well plate in RPMI-1640 (Gibco) with 10% FCS and 40 µg/ml gentamycin. After 24 h, 3×10^{5} or 3×10^{6} NK cells were added to the culture wells. The cytotoxicity assay was performed for 4 h at 37 °C, under 5% CO_2. Target hepatoma cells were harvested after trypsination, labeled with propidium iodide (PI) and analyzed by FACS. Cell death was monitored after morphological gating on hepatocytes.

2.2 Animal studies (Northern elephant seals)

All procedures were reviewed and approved by the Institutional Animal Care and Use Committees of the University of California, Merced and California State University, Sonoma. Northern elephant seal pups constituting two different cohorts at Año Nuevo State Reserve were studied at two postweaning periods (n = 5/period): early (1-2 weeks postweaning; 127 ± 1 kg) and late (6-7 weeks postweaning; 93 ± 4 kg). Pups were weighed, sedated, and infused in the field as previously described[7-9]. Briefly, pups were sedated with 1mg/kg Telazol (tiletamine/zolazepam HCl, Fort Dodge Labs, Ft Dodge, IA) administered intramuscularly. Once immobilized, an 18 gauge, 3.5 inch spinal needle was inserted into the extradural vein. Blood samples were obtained, and infusions performed from this site. Continuous immobilization was maintained with ~100mg bolus intravenous injections of ketamine as needed[10].

2.2.1 Insulin infusion protocol

To determine the metabolomic and lipidomic responses to insulin as a function of fasting-induced, adipose-specific insulin resistance, fasting seal pups were infused (i.v.) with a mass-specific dose (0.065 U insulin/kg) (Humulin; Eli Lilly, Indianapolis, IN) as previously described[9]. Time-course responses to insulin by comparing the differences of the area under the curve (AUC) values yield information about the metabolic plasticity of the animals in the context of fasting duration. Prior to each infusion, a pre-infusion blood sample (i.v.) was collected (baseline or T_0). Following the bolus infusion of insulin, blood samples collected at 10, 30, 60, and 120 min were used for this suite of metabolomic/lipidomic analyses. Procedures were terminated at 120 min out of concern for the safety of the animals. Immediately following the collection of the 120 min samples, glucose was infused slowly to assist in the restoration of pre-infusion levels. Blood samples were centrifuged on site for 15 min at 3000g, and the plasma

was transferred to cryo-vials, frozen by immersion in liquid nitrogen, and stored at −80°C.

2.2.2 Plasma sample preparation

Aliquots of plasma (30µL) stored at −80°C were thawed, extracted, derivatized, and the metabolite abundances quantified by gas chromatography time-of-flight (GCTOF) mass spectrometry (MS) as previously described[11]. Briefly, the aliquots were extracted with 1mL of degassed acetonitrile/isopropanol/water (3:3:2) solution at −20°C, centrifuged, the supernatant removed, and solvents evaporated to dryness under reduced pressure. To remove membrane lipids and triglycerides, dried samples were reconstituted with acetonitrile/water (1:1), decanted and taken to dryness under reduced pressure. Internal standards, C8-C30 fatty acid methyl esters, were added to samples and derivatized with methoxyamine hydrochloride in pyridine and subsequently by N-methyl-N-(trimethylsilyl) trifluoroacetamide (Sigma-Aldrich) for trimethylsilylation of acidic protons.

2.3 Metabolomics

GCMS and LCMS were utilized for metabolomic analyses of both cultured cells and plasma extracts. Chromatography allows for clear separation of distinct compounds with high resolution, while mass spectrometry offers rapid identification of analytes.

2.3.1 Metabolomics profiling

Cells were seeded at 13×10^5 cells per 75 cm^2 dishes. After 24 h, supernatant was removed and replaced by fresh culture medium. For quantification of metabolic flux from glucose, culture medium was supplemented with both [U-^{13}C]-glucose (Sigma-Aldrich; 389374-2 G) and unlabeled glucose at a 50:50 ratio (final concentration of 25 mM glucose). After 24 h, cells were harvested, washed twice with ice-cold PBS and cell pellets were frozen at -80 °C until metabolites extraction. Cell pellets were transferred into a pre-chilled microcentrifuge tube with 1 mL cold extraction buffer consisting of 50% methanol (A452, Fisher Scientific) in ultrapure water. Samples were then frozen in liquid nitrogen, thawed, and placed in a shaking dry bath (Thermo Fisher Scientific, Waltham, MA) set to 1100 rpm for 15 min at 4 °C. After centrifugation for 15 min at 12500 g and 4 °C (Sorvall, Thermo Fisher Scientific) using a fixed-angle F21-48×1.5 rotor, supernatants were collected and dried by vacuum centrifugation overnight. Dried metabolites were derivatized by addition of 20 µL of 2.0% methoxyaminehydrochloride in pyridine (MOX, TS-45950, Thermo Fisher Scientific) followed by incubation during 90 min in shaking dry bath at 30 °C and 1100 rpm. 90 µL of N-methyl-N-trimethylsilyltrifluoroacetamide (MSTFA, 701270.201, Macherey-Nagel) was added, and samples were incubated and shaken at 37 °C for 30 min before centrifugation for 5 min at 14,000 rpm and 4 °C. Metabolites contained in the supernatant were then separated by gas chromatography (GC, TRACE 1310, Thermo Fisher Scientific) coupled to a triple-quadrupole mass spectrometry system for analysis (QQQ GCMS, TSQ8000EI, TSQ8140403, Thermo Fisher Scientific), equipped with a 0.25 mm

inner diameter, 0.25 µm film thickness, 30 m length 5% diphenyl / 95% dimethyl polysiloxane capillary column (OPTIMA 5 MS Accent, 725820.30, Macherey-Nagel) and run under electron ionization at 70 eV. Using established separation methods[12-14], the GC was programed with an injection temperature of 250.0 °C and splitless injection volume of 1.0 µL. The GC oven temperature program started at 50 °C (323.15 K) for 1 min, rising at 10 K/min to 300.0 °C (573.15 K) with a final hold at this temperature for 6 min. The GC flow rate with helium carrier gas (HE, HE 5.0UHP, Praxair) was 1.2 mL/min. The transfer line temperature was set at 290.0 °C and ion source temperature at 295.0 °C. A range of 50-600 m/z was scanned with a scan time of 0.25 s.

2.3.2 Metabolomics data processing

Metabolites were identified using TraceFinder (v3.3, Thermo Fisher Scientific) based on libraries of metabolite retention times and fragmentation patterns (Metaflux, Merced, CA). Identified metabolites were quantified using the selected ion count peak area for specific mass ions, and standard curves generated from reference standards run in parallel. Peak intensities were median normalized. The mean and standard deviation for each quantified metabolite was calculated for each cell line and treatment condition. A univariate t-test was used to compare treatment conditions for each metabolite and cell line.

2.3.3 Metabolic network coherence computational analysis

In order to measure the consistency of differentially expressed genes with a metabolic network, we employed the metabolic network coherence measure introduced by Sonnenschein et al.[15] Here, we first extracted a gene-centric metabolic network from a given genome-scale metabolic model. This was achieved via the stoichiometric matrix and the gene-reaction associations contained in the metabolic model. We constructed the two projections of the bipartite graph represented by the stoichiometric matrix, yielding a metabolite-centric and a reaction-centric graph. The metabolite-centric graph allowed us to identify high-degree nodes ('currency metabolites' like H_2O, ATP, etc.), which are not informative about the network-like organization of the metabolic systems and need to be eliminated before interpreting the network architecture. The degree of a node is the number of neighbors the node has in the network. The percentage of remaining metabolites is one of the parameters of our analysis. Typical values are 90 to 98 percent (i.e., a removal of the highest 2 to 10% of metabolites with the highest degree as currency metabolites). After recomputing the reaction-centric graph based on the reduced number of metabolites, we can now evaluate the gene reaction associations to arrive at a gene-centric metabolic network. Given a set S of differentially expressed genes and the gene-centric metabolic network G, we can now analyze the subgraph of G spanned by all genes in S. The average clustering coefficient C in these subgraphs serves as a measure of the connectivity of this subgraph. The metabolic network coherence MC is the z-score of C computed with respect to a null model of randomly drawn gene sets with the same size as S. In this way, MC has an intuitive interpretation: The value of MC indicates, how many standard deviations away from randomness the clustering of the subgraph

spanned by the observed gene set S actually is. The genome-scale metabolic models employed here are the generic human metabolic model Recon 222. In general, different network measures can be used for evaluation of MC. In the scope of this study, we have tested several of them, but opted for average clustering coefficient C, as it yielded strongest statistical signal.

2.3.4 GCTOF data acquisition and processing

Derivatized samples were analyzed on an Agilent 7890A gas chromatograph (Santa Clara, CA) with a 30m long, 0.25mm i.d. Rtx5Sil-MS column with 0.25µm 5% diphenyl film with an additional 10m integrated guard column (Restek, Bellefonte PA)[11,16]. An aliquot (0.5µL) was injected at 50°C (ramped to 250°C) in splitless mode with a 25 sec splitless time. The chromatographic gradient consisted of a constant flow of 1mL/min, ramping the oven temperature from 50°C to 330°C over 22 min. Mass spectrometry was performed using a Leco Pegasus IV time-of-flight mass spectrometer, 230°C transfer line temperature, electron ionization at −70V, and an ion source temperature of 250°C. Mass spectra were acquired at 1800V detector voltage at m/z 85-500 with 17 spectra/sec. Acquired spectra were further processed using the BinBase database[17-18]. Briefly, output results were filtered based on multiple parameters to exclude noisy or inconsistent peaks[16]. Detailed criteria for peak reporting included mass spectral matching, spectral purity, signal-to-noise ratio, and retention time[17]. All entries in BinBase were matched against the Fiehn mass spectral library of 1,200 authentic metabolite spectra using retention index and mass spectrum information or the NIST11 commercial library. All samples were analyzed in one batch, and data quality and instrument performance were constantly monitored using quality control and reference plasma samples (National Institute of Standards and Technology 2011). Quality controls were comprised of a mixture of standards and analyzed every 10 samples, were monitored for changes in the ratio of the analyte peak heights, and used to ensure equivalent conditions within the instrument ($p>0.05$, t-Test comparing observed to expected ratios of analyte response factors) over the duration of the sample acquisition[11]. Pooled plasma samples (n=9) were included and served as additional quality controls to assess normalization efficiency. Metabolites were reported if present in at least 50% of the samples. Data reported as quantitative ion peak heights were normalized by the sum intensity of all annotated metabolites and used for further statistical analysis.

2.3.5 Targeted metabolomics analyses of non-esterified fatty acids and endocannabinoids: Non-esterified fatty acid sample preparation, data acquisition, and processing

Plasma NEFA were isolated as previously described[19-20]. Specifically, plasma aliquots (100mL) were enriched with 5mL 0.2mg/mL butylated hydroxytoluene/EDTA in 1:1 methanol/water, and a suite of extraction surrogates, which included deuterated-tri-palmitoyl glycerol (d31-16:0-TG; CDN Isotopes, Pointe-Claire, Quebec, Canada), deuterated distearoylphosphotidylcholine (d35-18:0-PC; Avanti Polar Lipids, Alabaster, Alabama), dodeca-(9E)-enoyl cholesterylesters (22:1n9-CE; NuChek Prep, Elysian MN) and dodecatrienoic acid (22:3n3; NuChek Prep). Lipids were then

extracted with cyclohexane/2-propanol/ammonium acetate (10:8:11). Enriched samples were mixed with cyclopropane/2-propanol (10:8:11) and the phases split with ammonium acetate. The organic phase was isolated and the aqueous phase was re-extracted with cyclohexane. The combined organic total lipid extract was reduced to dryness and reconstituted in 200µL of methanol/toluene (1:1), and the total lipid extract was used to quantify plasma fatty acids as methyl esters by GC-MS. Extracted samples were spiked with 15:1n5 free acid to track methylation efficiency, brought to a final volume of 200mL with 90:10 methanol/toluene (v/v), and left at room temperature for 30 min before being dried. The remaining fatty acid methyl esters were re-constituted in a hexane (300mL)/44mM tricosanoate methyl ester (23:0; NuChek Prep) (10µL) solution (30,000:1) and vortexed. A 100µL aliquot was transferred to a GC-MS vial for analysis (Agilent 6890/5973N MSD, Agilent Technologies, San Jose, CA) with electron impact ionization and in simultaneous-selected, ion monitoring/full scan mode. Analytes were separated on a 30m/0.25mm/0.25µm DB-225ms column. Analytes were quantified with ChemStation vE.02.14 (Agilent Technologies) using internal standard methodologies against 5 to 8 point calibration curves.

2.3.6 Endocannabinoid sample preparation, data acquisition, and processing

Endocannabinoids were isolated by solid phase extraction on 10mg Waters Oasis-HLB cartridges (Milford, MA) as previously described[21]. Prior to extraction, cartridges were washed with 1 column volume ethyl acetate followed by 2 column volumes methanol, and conditioned with 2mL of 95:5 (v/v) water/methanol (MeOH) with 0.1% acetic acid. The column reservoir was spiked with 5µL anti-oxidant solution, (0.2mg/mL BHT/EDTA in 1:1 MeOH/water), and 10µL 1000nM analytical surrogates. Sample aliquots (250µL media) were then introduced to the column reservoir and diluted with 1 column volume wash solution (5% MeOH, 0.1% acetic acid). The sample was gravity extracted and the sorbent bed was washed with 1 column volume of 20% methanol and 0.1% acetic acid. The solid-phase extraction cartridges were dried by vacuum (@ -7.5 in. Hg for 20 min). Analytes were then eluted by gravity with 0.2mL MeOH, followed by 0.5mL acetonitrile, followed by 0.5mL ethyl acetate into 2mL autosampler vials containing 10µL of a 20% glycerol/MeOH solution. Eluent was dried by vacuum evaporation for 35 min, and residues were re-constituted with 100µL of 100nM internal standard solution containing 1-cyclohexylureido, 3-dodecanoic acid (CUDA), in 50:50 MeOH/acetonitrile. Vials were vortexed for 1 min to dissolve residues, chilled 15 min on wet ice, and extracts transferred to a centrifugal filter (0.1µm Durapore, Millipore, Billerica, MA). After centrifugation (3 min at <4500g and 6°C), the extracts were transferred to 150µL glass inserts in 2mL amber vials, capped, and stored at −20°C until analysis by UPLC-MS/MS. The internal standard was used to quantify the recovery of the deuterated extraction surrogates by ratio response.

2.3.7 Endocannabinoid analysis

Analytes in a 10µL injection of extract were separated with an Aquity C18 Ethylene Bridged Hybrid (BEH) 1.7µm, 150mm × 2.1mm column utilizing a

Waters Acquity UPLC (Waters, Milford, MA). The solvent gradient is described in Table 1 with a slight modification from Shearer et al.[22] The autosampler was maintained at 10°C. Resolved analytes were detected by positive mode electrospray ionization and multiple reaction monitoring on an API 4000 QTrap (AB Sciex, Framingham, MA, USA) using the following operating parameters: curtain gas = 20.0 psi, temperature = 500°C, ion-spray voltage = 5500.00V, collision gas = high, ion source gas 1 & 2 = 40.0 psi, collision cell exit potential = 10.0V, and entrance potential = 10.0V. Analyte retention times, mass transitions, optimized collision and declustering potential voltages, dwell times, and analytical surrogate associations for each analyte are shown in Supplemental Table 1. Analytes were quantified using isotope dilution and internal standard methodology with 5 to 7 point calibration curves ($R2 \geq 0.997$). Calibrants and internal standards were either synthesized [CUDA] or purchased from commercial sources (Cayman Chemical, Ann Arbor, MI or Avanti Polar Lipids Inc., Alabaster, AL), unless otherwise indicated. Data was processed utilizing AB Sciex Analyst version 1.6.2.

2.4 Statistical analyses

All statistical analyses were performed using R version 3.0.1. The area under the curve (AUC) for t= 0, 10, 30, 60, and 120 min for each metabolite as a function of time post-insulin infusion at each fasting period was calculated based on trapezoidal rule integration. Calculated AUC values were used to summarize the relative change in metabolite concentrations as a function of time for each sample. Variance in AUC values accurately reflects the variance in sample-wise metabolite trends over time. Therefore, the AUC values represent efficient mathematical representations of the original data and enable comparisons between samples' metabolite concentrations over time. However, there is no assumed biochemical context encoded by the AUC method. Independent sample t-tests were conducted with adjustment for unequal variance. The probability of the test statistics (p-values) were adjusted for multiple hypotheses tested (adjusted p-value)[23] and the false discovery rate was independently estimated (q-value).

Cluster analysis was conducted using k-means on a self-organizing map (SOM). SOM was calculated on a 10 × 10 hexagonal grid from mean time course patterns for early or late fasting groups. The combined data set of early and late metabolite time course patterns were used to identify similarities between early and late groups. Cluster analysis was conducted using k-means on the 100 generated self-organizing map codebooks. The k-means cluster number was selected based on an evaluation of within-cluster distance for 2 to 50 clusters, with 7 clusters identified as the optimal cluster number. Metabolite to k-means cluster assignments were recovered based on their assignment to SOM codebooks.

Multivariate analyses, principal component analysis (PCA) and orthogonal partial least squares discriminant analysis (O-PLS-DA) were conducted on combined metabolite baseline and AUC values, which were mean centered and scaled to unit variance. PCA was calculated based on the singular value

decomposition[24]. PCA sample leverage (distance to center of mass in the PCA plane) and $D_{mod}X$ (projected distance to the PCA plane) were used to evaluate potential extreme and moderate outliers, respectively. O-PLSDA was used to build a classification model to discriminate between early and late fasting animal baseline and AUC patterns and to identify the top 10% of all variable contributions to the observed class discrimination between the two classes (feature selection). Leave-one-out cross-validation was used to fit a preliminary 2 latent variable (LV) O-PLS-DA model.

The top 10% of all AUC and baseline discriminants (features) were selected based on fulfilling two criteria: (1) correlation with model scores[25] (Spearman's rho, $P \leq 0.1$) and (2) the absolute value of the model loading on the first latent variable 1 (LV1) ≥ 90th quantile[26], where LV1 is the model component capturing the maximum difference between early and late fasting groups. The classification performance of the selected and excluded feature models was validated and compared using Monte Carlo cross-validation (MCCV) and permutation testing. MCCV was carried out by randomly selecting 2/3 of the animals as a training set (to build models) and using 1/3 of the animals to test the models, while maintaining the proportion of late and early samples in the full dataset. This procedure was repeated 100 times and used to estimate distributions for the model performance statistics. Permutation testing (prediction of randomly assigned phenotype labels) was combined with the described MCCV model cross-validation and used to estimate the probability of achieving the model's predictive performance by chance, through comparison of the actual model Q2, AUC, sensitivity, and specificity to those of the NULL hypothesis as defined by the permuted models. Permutation p-values[27] were calculated to describe the proportion of cross-validation results showing favorable (less than or greater than, depending on the specific metric) performance for the actual model compared to the permuted (random early or late class labels) and selected vs. excluded feature models.

Metabolic trajectory analysis[28] was carried out to display geometric differences in early and late fasting animals' response to insulin infusion. PCA was calculated on baseline (T_0) adjusted, centered, and scaled to unit variance metabolomic measurements for t = 0, 10, 30, 60 and 120 min. Separate models were calculated based on all measurements or only the top 10% of all O-PLS-DA selected metabolic discriminants between early and late fasting animals. PCA scores were annotated with median scores and standard errors for each group/time-point pair.

Network analysis was used to assess statistically significant results within a biochemical context. A biochemical and chemical similarity network[29] was calculated for all measured metabolites with KEGG[30] and PubChem CID[31] identifiers using MetaMapR[32]. Enzymatic interactions were determined based on product-precursor relationships defined in the KEGG RPAIR database. Molecules not directly involved in biochemical transformations, but sharing structural properties, based on PubChem Substructure Fingerprints[33] were connected at a Tanimoto similarity threshold ≥ 0.7. Pathway enrichment analysis was conducted using Metaboanalyst 3.0[34]. Significantly different metabolites between early and late-fasting mammals were matched against the

Homo sapiens pathway library and analyzed using hypergeometric tests with out-degree centrality.

2.5 Transcriptome profiling of Huh7 and Huh7-*GCK*$^{+}$/*HK2*$^{-}$ cell lines

Transcriptome profiling was performed by next-generation sequencing (ProfileXpert, Lyon, France). Briefly, Total RNA was extracted and purified from cell pellets using Direct-zol RNA purification kit (Zymo Research). 700 ng of total RNA were amplified (NextFlex Rapid Directional mRNA-Seq, PerkinElmer) to generate mRNA-seq libraries. Then, gene expression was analyzed by next-generation sequencing (NGS) using Illumina NextSeq500. Reads were mapped on the reference genome *Homo sapiens* GRCh37/hg19. Raw data were processed using the DESeq2 pipeline[35] to identify differentially expressed genes. See Supporting Information and Gene Expression Omnibus database with the accession number GSE144214 for entire raw data.

2.5.1 Pathway analysis

The list of transcripts differentially expressed in Huh7 and Huh7-*GCK*$^{+}$/*HK2*$^{-}$ cell lines was analyzed by gene set enrichment analysis (IPA, Build version: 486617 M, Qiagen) weighted by their corresponding fold change and p value. The fold change cut-off of mean expression for each transcript was set at 2 with an adjusted p value<0.05. The list of genes associated with "Type I-IFN signaling pathway" was defined in the AmiGO 2 database. Expression data of these genes were retrieved from the transcriptomes of Huh7-*GCK*$^{+}$/*HK2*$^{-}$ and Huh7, and correspond for each gene to the most differentially expressed transcript.

2.6 References

1. Ran FA, Hsu PD, Wright J, Agarwala V, Scott DA, Zhang F. Genome editing using the CRISPR-Cas9 system. *Nat Protoc*. 2013;8(11):2281-2308. PMID: 24157548.

2. Kuang Y, Schomisch SJ, Chandramouli V, Lee Z. Hexokinase and glucose-6-phosphatase activity in woodchuck model of hepatitis virus-induced hepatocellular carcinoma. *Comp Biochem Physiol C Toxicol Pharmacol*. 2006;143(2):225-31. PMID: 16581304.

3. Ramière C, Rodriguez J, Enache LS, Lotteau V, André P, Diaz O. Activity of hexokinase is increased by its interaction with hepatitis C virus protein NS5A. *J Virol*. 2014;88(6):3246-3254. PMID: 24390321.

4. Perrin-Cocon L, Aublin-Gex A, Diaz O, et al. Toll-like receptor 4-induced glycolytic burst in human monocyte-derived dendritic cells results from p38-dependent stabilization of HIF-1α and increased hexokinase II expression. *J Immunol*. 2018;201(5):1510-1521. PMID: 30037846.

5. Payne J, Morris JG. Pyruvate carboxylase in *Rhodopseudomonas spheroides*. *J Gen Microbiol*. 1969;59(1):97-101. PMID: 5365367.

6. Scholtes C, Ramière C, Rainteau D, et al. High plasma level of nucleocapsid-free envelope glycoprotein-positive lipoproteins in hepatitis C patients. *Hepatology*. 2012;56(1):39-48. PMID: 22290760.

7. Viscarra JA, Champagne CD, Crocker DE, Ortiz RM. 5'AMP-activated protein kinase activity is increased in adipose tissue of Northern elephant seal pups during prolonged fasting-induced insulin resistance. *J Endocrinol*. 2011;209(3):317-325. PMID: 21429964.

8. Viscarra JA, Vázquez-Medina JP, Crocker DE, Ortiz RM. Glut4 is upregulated despite decreased insulin signaling during prolonged fasting in Northern elephant seal pups. *Am J Physiol Regul Integr Comp Physiol*. 2011;300(1):R150-154. PMID: 20980624.

9. Viscarra JA, Rodriguez R, Vázquez-Medina JP, et al. Insulin and GLP-1 infusions demonstrate the onset of adipose-specific insulin resistance in a large fasting mammal: potential glucogenic role for GLP-1. *Physiol Rep*. 2013;1(2):e00023. PMID: 23997935.

10. Champagne CD, Houser DS, Fowler MA, Costa DP, Crocker DE. Gluconeogenesis is associated with high rates of tricarboxylic acid and pyruvate cycling in fasting Northern elephant seals. *Am J Physiol Regul Integr Comp Physiol*. 2012;303(3):R340-52. PMID: 22673783.

11. Fiehn O. Extending the breadth of metabolite profiling by gas chromatography coupled to mass spectrometry. *Trends Analyt Chem*. 2008;27(3):261-269. PMID: 18497891.

12. Lanning NJ, Castle JP, Singh SJ, et al. Metabolic profiling of triple-negative breast cancer cells reveals metabolic vulnerabilities. *Cancer Metab*. 2017;5:6. PMID: 28852500.

13. Shah R, Singh SJ, Eddy K, Filipp FV, Chen S. Concurrent targeting of glutaminolysis and metabotropic glutamate receptor 1 (GRM1) reduces glutamate bioavailability in GRM1$^+$ melanoma. *Cancer Res*. 2019;79(8):1799-1809. PMID: 30987979.

14. Filipp FV, Scott DA, Ronai ZA, Osterman AL, Smith JW. Reverse TCA cycle flux through isocitrate dehydrogenases 1 and 2 is required for lipogenesis in hypoxic melanoma cells. *Pigment Cell Melanoma Res*. 2012;25(3):375-83. PMID: 22360810.

15. Sonnenschein N, Geertz M, Muskhelishvili G, Hütt M. Analog regulation of metabolic demand. *BMC Syst Biol*. 2011;5:40. PMID: 21406074.

16. Kind T, Tolstikov V, Fiehn O, Weiss RH. A comprehensive urinary metabolomic approach for identifying kidney cancer. *Anal Biochem*. 2007;363(2):185-195. PMID: 17316536.

17. Fiehn O, Wohlgemuth G, Scholz M. Setup and annotation of metabolomic experiments by integrating biological and mass spectrometric metadata. *Proc Lect Notes Bioinformatics*. 2005;224-239.

18. Scholz M, Fiehn O. SetupX – a public study design database for metabolomic projects. *Pac Symp Biocomput*. 2007;169-180. PMID: 17990490.

19. Smedes F. Determination of total lipid using non-chlorinated solvents. *Analyst*. 1999;124:1711-1718.

20. Gladine C, Newman JW, Durand T, et al. Lipid profiling following intake of the omega 3 fatty acid DHA identifies the peroxidized metabolites F4-neuroprostanes as the best predictors of atherosclerosis prevention. *PLoS One*. 2014;9(2):e89393. PMID: 24558496.

21. Luria A, Weldon SM, Kabcenell AK, et al. Compensatory mechanism for homeostatic blood pressure regulation in Ephx2 gene-disrupted mice. *J Biol Chem*. 2007;282(5):2891-2898. PMID: 17135253.

22. Shearer GC, Harris WS, Pedersen TL, Newman JW. Detection of omega-3 oxylipins in human plasma and response to treatment with omega-3 acid ethyl esters. *J Lipid Res*. 2010;51(8):2074-2081. PMID: 19671931.

23. Benjamini Y, Hochberg Y. Controlling the false discovery rate: a practical and powerful approach to multiple testing. *J R Stat Soc Series B Stat Methodol*. 1995;57(1):289-300.

24. Stacklies W, Redestig H, Scholz M, Walther D, Selbig J. pcaMethods – a bioconductor package providing PCA methods for incomplete data. *Bioinformatics*. 2007;23(9):1164-1167. PMID: 17344241.

25. Wiklund S, Johansson E, Sjöström L, et al. Visualization of GC/TOF-MS-based metabolomics data for identification of biochemically interesting compounds using OPLS class models. *Anal Chem*. 2008;80(1):115-122. PMID: 18027910.

26. Palermo G, Piraino P, Zucht HD. Performance of PLS regression coefficients in selecting variables for each response of a multivariate PLS for omics-type data. *Adv Appl Bioinform Chem*. 2009;2:57-70. PMID: 21918616.

27. Phipson B, Smyth GK. Permutation P-values should never be zero: calculating exact P-values when permutations are randomly drawn. *Stat Appl Genet Mol Biol*. 2010;9:Article39. PMID: 21044043.

28. Keun HC, Ebbels TM, Bollard ME, et al. Geometric trajectory analysis of metabolic responses to toxicity can define treatment specific profiles. *Chem Res Toxicol*. 2004;17(5):579-587. PMID: 15144214.

29. Barupal DK, Haldiya PK, Wohlgemuth G, et al. MetaMapp: mapping and visualizing metabolomic data by integrating information from biochemical pathways and chemical and mass spectral similarity. *BMC Bioinformatics*. 2012;13:99. PMID: 22591066.

30. Kanehisa M, Sato Y, Kawashima M, Furumichi M, Tanabe M. KEGG as a reference resource for gene and protein annotation. *Nucleic Acids Res*. 2016;44(D1):D457-462. PMID: 26476454.

31. Kim S, Thiessen PA, Bolton EE, et al. PubChem substance and compound databases. *Nucleic Acids Res*. 2016;44(D1):D1202-1213. PMID: 26400175.

32. Grapov D, Wanichthanarak K, Fiehn O. MetaMapR: pathway independent metabolomic network analysis incorporating unknowns. *Bioinformatics*. 2015;31(16):2757-2760. PMID: 25847005.

33. Cao Y, Jiang T, Girke T. A maximum common substructure-based algorithm for searching and predicting drug-like compounds. *Bioinformatics*. 2008;24(13):i366-374. PMID: 18586736.

34. Xia J, Wishart DS. Web-based inference of biological patterns, functions and pathways from metabolomic data using MetaboAnalyst. *Nat Protoc*. 2011;6(6):743-760. PMID: 21637195.

35. Love MI, Huber W, Anders S. Moderated estimation of fold change and dispersion for RNA-seq data with DESeq2. *Genome Biol*. 2014;15(12):550. PMID: 25516281.

Chapter Three: Insulin induces a shift in lipid and primary carbon metabolites in a model of fasting-induced insulin resistance

Prolonged fasting in Northern elephant seals (NES) is characterized by a reliance on lipid metabolism, conservation of protein, and reduced plasma insulin. During early fasting, glucose infusion previously reduced plasma free fatty acids (FFA); however, during late-fasting, it induced an atypical elevation in FFA despite comparable increases in insulin during both periods suggestive of a dynamic shift in tissue responsiveness to glucose-stimulated insulin secretion. To better assess the contribution of insulin to this fasting-associated shift in substrate metabolism, we compared the responses of plasma metabolites (amino acids (AA), FFA, endocannabinoids (EC), and primary carbon metabolites (PCM)) to an insulin infusion (65 mU/kg) in early- and late-fasted NES pups (n = 5/group).

In early fasting, the majority (72%) of metabolite trajectories return to baseline levels within 2 h, but not in late fasting indicative of an increase in tissue sensitivity to insulin. In late fasting, increases in FFA and ketone pools, coupled with decreases in AA and PCM, indicate a shift toward lipolysis, beta-oxidation, ketone metabolism, and decreased protein catabolism. Conversely, insulin increased PCM AUC in late fasting suggesting that gluconeogenic pathways are activated. Insulin also decreased FFA AUC between early and late fasting suggesting that insulin suppresses triglyceride hydrolysis.

Naturally adapted tolerance to prolonged fasting in these mammals is likely accomplished by suppressing insulin levels and activity, providing novel insight on the evolution of insulin during a condition of temporary, reversible insulin resistance.

Chapter Three: Insulin induces a shift in lipid and primary carbon metabolites in a model of fasting-induced insulin resistance

Keedrian I. Olmstead[1,2], Michael R. La Frano[3,4,5], Johannes Fahrmann[3,6], Dmitry Grapov[3], Jose A. Viscarra[2], John W. Newman[3,4], Oliver Fiehn[3,7], Daniel E. Crocker[8], Fabian V. Filipp[1,2,3,*], and Rudy M. Ortiz[2,*]

[1]Systems Biology and Cancer Metabolism, Program for Quantitative Systems Biology, University of California, Merced

[2]Molecular Cell Biology, School of Natural Sciences, University of California, Merced, USA

[3]NIH West Coast Metabolomics Center, University of California, Davis

[4]Obesity and Metabolism Research Unit, USDA-Agricultural Research Service Western Human Nutrition Research Center, University of California, Davis, USA

[5]Department of Food Science and Nutrition, California Polytechnic State University, San Luis Obispo, USA

[6]Cancer Treatment Center, UT MD Anderson, Houston, USA

[7]Biochemistry Department, King Abdulaziz University, Jeddah, Saudi Arabia

[8]Biology, Sonoma State University, Rohnert Park, USA

*Corresponding Authors: Fabian V. Filipp, filipp@ucmerced.edu, Rudy M. Ortiz, rortiz@ucmerced.edu.

Abstract

Introduction— Prolonged fasting in Northern elephant seals (NES) is characterized by a reliance on lipid metabolism, conservation of protein, and reduced plasma insulin. During early fasting, glucose infusion previously reduced plasma free fatty acids (FFA); however, during late-fasting, it induced an atypical elevation in FFA despite comparable increases in insulin during both periods suggestive of a dynamic shift in tissue responsiveness to glucose-stimulated insulin secretion.

Objective— To better assess the contribution of insulin to this fasting-associated shift in substrate metabolism.

Methods— We compared the responses of plasma metabolites (amino acids (AA), FFA, endocannabinoids (EC), and primary carbon metabolites (PCM)) to an insulin infusion (65 mU/kg) in early- and late-fasted NES pups (n = 5/group). Plasma samples were collected prior to infusion (T_0) and at 10, 30, 60, and 120 min post-infusion, and underwent untargeted and targeted metabolomics analyses utilizing a variety of GC-MS and LC-MS technologies.

Results— In early fasting, the majority (72%) of metabolite trajectories return to baseline levels within 2 h, but not in late fasting indicative of an increase in tissue sensitivity to insulin. In late fasting, increases in FFA and ketone pools, coupled with decreases in AA and PCM, indicate a shift toward lipolysis, beta-oxidation, ketone metabolism, and decreased protein catabolism. Conversely, insulin increased PCM AUC in late fasting suggesting that gluconeogenic pathways are activated. Insulin also decreased FFA AUC between early and late fasting suggesting that insulin suppresses triglyceride hydrolysis.

Conclusion— Naturally adapted tolerance to prolonged fasting in these mammals is likely accomplished by suppressing insulin levels and activity, providing novel insight on the evolution of insulin during a condition of temporary, reversible insulin resistance.

Keywords— Endocannabinoids; Fatty acids; Lipidomics; Metabolomics; Substrate metabolism

3.1 Introduction

The classical actions of insulin are to stimulate cellular glucose uptake and promote anabolic processes[1]. Thus, during periods of starvation or extended food deprivation, insulin and insulin signaling are suppressed to help preserve circulating glucose to support the energetic burdens imposed by the caloric restriction/reduction[2]. Therefore, brief and acute bouts of reversible insulin resistance are adaptive in most vertebrates to ameliorate the stress of short-term or abbreviated periods of food deprivation. However, prolonged (2-3 months) fasting is a natural component of the life history of the Northern elephant seal (NES) that is characterized by reliance on lipid oxidation, conservation of protein, and reversible adipose-specific insulin resistance[3-7].

Glucose-stimulated insulin secretion, similar to what is achieved during an oral glucose tolerance test (oGTT), typically reduces plasma non-esterified free fatty acids (NEFA)[8], and this response is consistent during early fasting in NES pups[9]. However, during late fasting, an oGTT induced an atypical elevation in NEFA suggesting that prolonged fasting in seals initiates a dynamic shift in substrate utilization, especially as it relates to lipid metabolism. This phenotype in late-fasted seal pups is consistent with the development of adipose-specific insulin resistance and demonstrates the remarkable plasticity of their metabolic network (being able to switch between extreme stages of body mass gain and prolonged fasting independent of consequences on energy balance). Furthermore, a detailed acylcarnitine profile in early- and late-fasted NES pups revealed that total plasma acylcarnitine and acyl:free carnitine ratio increased, indicative of increased accumulation of plasma fatty acylcarnitines and of a higher degree of incomplete β-oxidation with fasting-induced insulin resistance[10]. The fasting-associated increase in plasma acyl:free carnitine ratio suggests that a temporal change in the dynamics of mitochondrial β-oxidation occurs with fasting duration in NES pups[11]. This acylcarnitine profile also revealed higher levels of medium-chain fatty acid acylcarnitine derivatives that are consistent with those observed in insulin-resistant mice[12] and type 2

diabetic humans[13]. These patterns of acylcarnitine derivatives are also indicative of increased lipid metabolism and decreased protein catabolism[10]. Thus, high-throughput analyses such as acylcarnitine profiles are extremely useful in helping to elucidate potential cellular mechanisms and more thoroughly describe dynamic shifts in substrate utilization and metabolism.

Extensive metabolomic studies in diabetic subjects[14-19] and animals[12,20], and the metabolomic response to an oGTT in humans have been performed[21-24]. These studies demonstrate distinct alterations in amino acid and branched-chain fatty acid metabolism between normoglycemic and insulin resistant/diabetic subjects[14-19,25]. Furthermore, the difference in metabolomic response to an oGTT between normal weight/glycemic subjects and their obese/diabetic counterparts is strikingly distinct and can offer significant insight as to which cellular mechanisms are perturbed (i.e., TCA cycle, mitochondrial β-oxidation, gluconeogenesis, lipolysis etc.). However, during an oGTT, circulating insulin is elevated via glucose-stimulated insulin secretion, making it difficult to differentiate the direct glucose from the insulin-mediated effects. Unfortunately, to the best of our knowledge, the metabolomic and lipidomic responses to insulin infusion have not been reported. Therefore, to better assess this insulin-associated shift in substrate metabolism, we compared the response of plasma metabolites to insulin infusion in early- and late-fasted NES pups, which exhibit a unique insulin resistance-like metabolic phenotype with fasting duration.

3.2 Methods

3.2.1 Animals

All procedures were reviewed and approved by the Institutional Animal Care and Use Committees of the University of California, Merced and California State University, Sonoma. Northern elephant seal pups constituting two different cohorts at Año Nuevo State Reserve were studied at two postweaning periods (n = 5/period): early (1-2 weeks postweaning; 127 ± 1 kg) and late (6-7 weeks postweaning; 93 ± 4 kg). Pups were weighed, sedated, and infused in the field as previously described[5,9,26]. Briefly, pups were sedated with 1mg/kg Telazol (tiletamine/ zolazepam HCl, Fort Dodge Labs, Ft Dodge, IA) administered intramuscularly. Once immobilized, an 18 gauge, 3.5 inch spinal needle was inserted into the extradural vein. Blood samples were obtained, and infusions performed from this site. Continuous immobilization was maintained with ~100mg bolus intravenous injections of ketamine as needed[27].

3.2.2 Insulin infusion protocol

To determine the metabolomic and lipidomic responses to insulin as a function of fasting-induced, adipose-specific insulin resistance, fasting seal pups were infused (i.v.) with a mass-specific dose (0.065 U insulin/kg) (Humulin; Eli Lilly, Indianapolis, IN) as previously described[5]. Time-course responses to insulin by comparing the differences of the area under the curve (AUC) values yield information about the metabolic plasticity of the animals in the context of fasting duration. Prior to each infusion, a pre-infusion blood sample (i.v.) was collected

(baseline or T_0). Following the bolus infusion of insulin, blood samples collected at 10, 30, 60, and 120 min were used for this suite of metabolomic/lipidomic analyses. Procedures were terminated at 120 min out of concern for the safety of the animals. Immediately following the collection of the 120 min samples, glucose was infused slowly to assist in the restoration of pre-infusion levels. Blood samples were centrifuged on site for 15 min at 3000g, and the plasma was transferred to cryo-vials, frozen by immersion in liquid nitrogen, and stored at −80°C.

3.2.3 Analysis of primary metabolites

The MiniX database[28] was used as a Laboratory Information Management System (LIMS) and for sample randomization prior to all analytical procedures.

3.2.4 Sample preparation

Aliquots of plasma (30µL) stored at −80°C were thawed, extracted, derivatized, and the metabolite abundances quantified by gas chromatography time-of-flight (GCTOF) mass spectrometry (MS) as previously described[29]. Briefly, the aliquots were extracted with 1mL of degassed acetonitrile/isopropanol/water (3:3:2) solution at −20°C, centrifuged, the supernatant removed, and solvents evaporated to dryness under reduced pressure. To remove membrane lipids and triglycerides, dried samples were reconstituted with acetonitrile/water (1:1), decanted and taken to dryness under reduced pressure. Internal standards, C8-C30 fatty acid methyl esters, were added to samples and derivatized with methoxyamine hydrochloride in pyridine and subsequently by N-methyl-N-(trimethylsilyl) trifluoroacetamide (Sigma-Aldrich) for trimethylsilylation of acidic protons.

3.2.5 GCTOF data acquisition and processing

Derivatized samples were analyzed on an Agilent 7890A gas chromatograph (Santa Clara, CA) with a 30m long, 0.25mm i.d. Rtx5Sil-MS column with 0.25µm 5% diphenyl film with an additional 10m integrated guard column (Restek, Bellefonte PA)[29-30]. An aliquot (0.5µL) was injected at 50°C (ramped to 250°C) in splitless mode with a 25 sec splitless time. The chromatographic gradient consisted of a constant flow of 1mL/ min, ramping the oven temperature from 50°C to 330°C over 22 min. Mass spectrometry was performed using a Leco Pegasus IV time-of-flight mass spectrometer, 230°C transfer line temperature, electron ionization at −70V, and an ion source temperature of 250°C. Mass spectra were acquired at 1800V detector voltage at m/z 85-500 with 17 spectra/sec. Acquired spectra were further processed using the BinBase database[28,31]. Briefly, output results were filtered based on multiple parameters to exclude noisy or inconsistent peaks[30]. Detailed criteria for peak reporting included mass spectral matching, spectral purity, signal-to-noise ratio, and retention time[31]. All entries in BinBase were matched against the Fiehn mass spectral library of 1,200 authentic metabolite spectra using retention index and mass spectrum information or the NIST11 commercial library. All samples were analyzed in one batch, and data quality and instrument performance were constantly monitored using quality control and reference plasma samples (National Institute of Standards and Technology 2011). Quality controls were

comprised of a mixture of standards and analyzed every 10 samples, were monitored for changes in the ratio of the analyte peak heights, and used to ensure equivalent conditions within the instrument ($p>0.05$, t-Test comparing observed to expected ratios of analyte response factors) over the duration of the sample acquisition[29]. Pooled plasma samples (n=9) were included and served as additional quality controls to assess normalization efficiency. Metabolites were reported if present in at least 50% of the samples. Data reported as quantitative ion peak heights were normalized by the sum intensity of all annotated metabolites and used for further statistical analysis.

3.2.6 Targeted metabolomics analyses of non-esterified fatty acids and endocannabinoids: Non-esterified fatty acid sample preparation, data acquisition, and processing

Plasma NEFA were isolated as previously described[32-33]. Specifically, plasma aliquots (100mL) were enriched with 5mL 0.2mg/mL butylated hydroxytoluene/EDTA in 1:1 methanol/water, and a suite of extraction surrogates, which included deuterated-tri-palmitoyl glycerol (d31-16:0-TG; CDN Isotopes, Pointe-Claire, Quebec, Canada), deuterated distearoylphosphotidylcholine (d35-18:0-PC; Avanti Polar Lipids, Alabaster, Alabama), dodeca-(9E)-enoyl cholesterylesters (22:1n9-CE; NuChek Prep, Elysian MN) and dodecatrienoic acid (22:3n3; NuChek Prep). Lipids were then extracted with cyclohexane/2-propanol/ammonium acetate (10:8:11). Enriched samples were mixed with cyclopropane/2-propanol (10:8:11) and the phases split with ammonium acetate. The organic phase was isolated and the aqueous phase was re-extracted with cyclohexane. The combined organic total lipid extract was reduced to dryness and reconstituted in 200µL of methanol/toluene (1:1), and the total lipid extract was used to quantify plasma fatty acids as methyl esters by GC-MS. Extracted samples were spiked with 15:1n5 free acid to track methylation efficiency, brought to a final volume of 200mL with 90:10 methanol/toluene (v/v), and left at room temperature for 30 min before being dried. The remaining fatty acid methyl esters were re-constituted in a hexane (300mL)/44mM tricosanoate methyl ester (23:0; NuChek Prep) (10µL) solution (30,000:1) and vortexed. A 100µL aliquot was transferred to a GC-MS vial for analysis (Agilent 6890/5973N MSD, Agilent Technologies, San Jose, CA) with electron impact ionization and in simultaneous-selected, ion monitoring/ full scan mode. Analytes were separated on a 30m/0.25mm/0.25µm DB-225ms column. Analytes were quantified with ChemStation vE.02.14 (Agilent Technologies) using internal standard methodologies against 5 to 8 point calibration curves.

3.2.7 Endocannabinoid sample preparation, data acquisition, and processing

Endocannabinoids were isolated by solid phase extraction on 10mg Waters Oasis-HLB cartridges (Milford, MA) as previously described[34]. Prior to extraction, cartridges were washed with 1 column volume ethyl acetate followed by 2 column volumes methanol, and conditioned with 2mL of 95:5 (v/v) water/methanol (MeOH) with 0.1% acetic acid. The column reservoir was spiked with 5µL anti-oxidant solution, (0.2mg/mL BHT/EDTA in 1:1

MeOH/water), and 10µL 1000nM analytical surrogates. Sample aliquots (250µL media) were then introduced to the column reservoir and diluted with 1 column volume wash solution (5% MeOH, 0.1% acetic acid). The sample was gravity extracted and the sorbent bed was washed with 1 column volume of 20% methanol and 0.1% acetic acid. The solid-phase extraction cartridges were dried by vacuum (@ -7.5 in. Hg for 20 min). Analytes were then eluted by gravity with 0.2mL MeOH, followed by 0.5mL acetonitrile, followed by 0.5mL ethyl acetate into 2mL autosampler vials containing 10µL of a 20% glycerol/MeOH solution. Eluent was dried by vacuum evaporation for 35 min, and residues were re-constituted with 100µL of 100nM internal standard solution containing 1cyclohexylureido, 3-dodecanoic acid (CUDA), in 50:50 MeOH/acetonitrile. Vials were vortexed for 1 min to dissolve residues, chilled 15 min on wet ice, and extracts transferred to a centrifugal filter (0.1µm Durapore, Millipore, Billerica, MA). After centrifugation (3 min at <4500g and 6°C), the extracts were transferred to 150µL glass inserts in 2mL amber vials, capped, and stored at −20°C until analysis by UPLC-MS/MS. The internal standard was used to quantify the recovery of the deuterated extraction surrogates by ratio response.

3.2.8 Endocannabinoid analysis

Analytes in a 10µL injection of extract were separated with an Aquity C18 Ethylene Bridged Hybrid (BEH) 1.7µm, 150mm × 2.1mm column utilizing a Waters Acquity UPLC (Waters, Milford, MA). The solvent gradient is described in Table 1 with a slight modification from Shearer et al.[35] The autosampler was maintained at 10°C. Resolved analytes were detected by positive mode electrospray ionization and multiple reaction monitoring on an API 4000 QTrap (AB Sciex, Framingham, MA, USA) using the following operating parameters: curtain gas = 20.0 psi, temperature = 500°C, ion-spray voltage = 5500.00V, collision gas = high, ion source gas 1 & 2 = 40.0 psi, collision cell exit potential = 10.0V, and entrance potential = 10.0V. Analyte retention times, mass transitions, optimized collision and declustering potential voltages, dwell times, and analytical surrogate associations for each analyte are shown in Supplemental Table 1. Analytes were quantified using isotope dilution and internal standard methodology with 5 to 7 point calibration curves ($R2 \geq 0.997$). Calibrants and internal standards were either synthesized [CUDA] or purchased from commercial sources (Cayman Chemical, Ann Arbor, MI or Avanti Polar Lipids Inc., Alabaster, AL), unless otherwise indicated. Data was processed utilizing AB Sciex Analyst version 1.6.2. Surrogate recoveries are in Supplemental Table 1.

3.2.9 Statistical analyses

All statistical analyses were performed using R version 3.0.1. The area under the curve (AUC) for t= 0, 10, 30, 60, and 120 min for each metabolite as a function of time post-insulin infusion at each fasting period was calculated based on trapezoidal rule integration. Calculated AUC values were used to summarize the relative change in metabolite concentrations as a function of time for each sample. Variance in AUC values accurately reflects the variance in sample-wise metabolite trends over time. Therefore, the AUC values represent efficient mathematical representations of the original data and enable

comparisons between samples' metabolite concentrations over time. However, there is no assumed biochemical context encoded by the AUC method. Independent sample t-tests were conducted with adjustment for unequal variance. The probability of the test statistics (p-values) were adjusted for multiple hypotheses tested (adjusted p-value)[36] and the false discovery rate was independently estimated (q-value).

Cluster analysis was conducted using k-means on a self-organizing map (SOM). SOM was calculated on a 10 × 10 hexagonal grid from mean time course patterns for early or late fasting groups. The combined data set of early and late metabolite time course patterns were used to identify similarities between early and late groups. Cluster analysis was conducted using k-means on the 100 generated self-organizing map codebooks. The k-means cluster number was selected based on an evaluation of within-cluster distance for 2 to 50 clusters, with 7 clusters identified as the optimal cluster number. Metabolite to k-means cluster assignments were recovered based on their assignment to SOM codebooks.

Multivariate analyses, principal component analysis (PCA) and orthogonal partial least squares discriminant analysis (O-PLS-DA) were conducted on combined metabolite baseline and AUC values, which were mean centered and scaled to unit variance. PCA was calculated based on the singular value decomposition (Stacklies et al. 2007). PCA sample leverage (distance to center of mass in the PCA plane) and $D_{mod}X$ (projected distance to the PCA plane) were used to evaluate potential extreme and moderate outliers, respectively. O-PLSDA was used to build a classification model to discriminate between early and late fasting animal baseline and AUC patterns and to identify the top 10% of all variable contributions to the observed class discrimination between the two classes (feature selection). Leave-one-out cross-validation was used to fit a preliminary 2 latent variable (LV) O-PLS-DA model.

The top 10% of all AUC and baseline discriminants (features) were selected based on fulfilling two criteria: (1) correlation with model scores[38] (Spearman's rho, $P \leq 0.1$) and (2) the absolute value of the model loading on the first latent variable 1 (LV1) ≥ 90th quantile[39], where LV1 is the model component capturing the maximum difference between early and late fasting groups. The classification performance of the selected and excluded feature models was validated and compared using Monte Carlo cross-validation (MCCV) and permutation testing. MCCV was carried out by randomly selecting 2/3 of the animals as a training set (to build models) and using 1/3 of the animals to test the models, while maintaining the proportion of late and early samples in the full dataset. This procedure was repeated 100 times and used to estimate distributions for the model performance statistics. Permutation testing (prediction of randomly assigned phenotype labels) was combined with the described MCCV model cross-validation and used to estimate the probability of achieving the model's predictive performance by chance, through comparison of the actual model Q2, AUC, sensitivity, and specificity to those of the NULL hypothesis as defined by the permuted models. Permutation p-values[40] were calculated to describe the proportion of cross-validation results showing favorable (less than or greater than, depending on the specific metric)

performance for the actual model compared to the permuted (random early or late class labels) and selected vs. excluded feature models.

Metabolic trajectory analysis[41] was carried out to display geometric differences in early and late fasting animals' response to insulin infusion. PCA was calculated on baseline (T_0) adjusted, centered, and scaled to unit variance metabolomic measurements for t = 0, 10, 30, 60 and 120 min. Separate models were calculated based on all measurements or only the top 10% of all O-PLS-DA selected metabolic discriminants between early and late fasting animals. PCA scores were annotated with median scores and standard errors for each group/time-point pair.

Network analysis was used to assess statistically significant results within a biochemical context. A biochemical and chemical similarity network[42] was calculated for all measured metabolites with KEGG[43] and PubChem CID[44] identifiers using MetaMapR[45]. Enzymatic interactions were determined based on product-precursor relationships defined in the KEGG RPAIR database. Molecules not directly involved in biochemical transformations, but sharing structural properties, based on PubChem Substructure Fingerprints[46] were connected at a Tanimoto similarity threshold ≥ 0.7. Pathway enrichment analysis was conducted using Metaboanalyst 3.0[47]. Significantly different metabolites between early and late-fasting mammals were matched against the *Homo sapiens* pathway library and analyzed using hypergeometric tests with out-degree centrality.

3.3 Results

3.3.1 Prolonged fasting increases β-oxidation and spares lean tissue

We identified 41 out of 171 known metabolites that changed significantly in baseline (T0) values between early and late fasting ($p<0.05$) (Figure 1 and Supplemental Table 1). These metabolites clustered into seven distinct biochemical categories for analysis: **(1)** amino acids, **(2)** endocannabinoids, **(3)** fatty acids, **(4)** glucose, **(5)** ketone bodies, **(6)** organic acids, and **(7)** primary carbon metabolites (Figure 1). Prolonged fasting was associated with the most profound changes in FFA. The increases in baseline fatty acid concentrations ranged from 28% (palmitic acid) to 144% (elaidic acid). Similarly, the ketones acetoacetate and 3hydroxybutyric acid increased 133% and 347% in late fasting, respectively.

Conversely, there were mixed changes with other primary metabolites and endocannabinoids over this time (Fig. 1 and Supplemental Table 1). The primary metabolite 1,5anhydroglucitol and endocannabinoid anandamide increased by 37% and 74%, respectively. Several of these metabolites are downstream products of lipid oxidation, providing additional evidence of upregulated lipid oxidation in late fasting. In contrast, endocannabinoid-like DHEA and SEA and glucogenic/ketogenic amino acids alanine, asparagine, cysteine, tryptophan, tyrosine and valine decreased.

When baseline levels were normalized to the animal's plasma volume (estimated by body mass) to correct for changes associated with fasting duration[48], this correction had only a subtle effect on our results. The effect of this correction was observed in a few metabolites related to lipid oxidation. However, since many lipid oxidation products were significant without plasma volume adjustment, this did not change our interpretation of the results. Pathway enrichment analysis of significantly perturbed metabolites ($p < 0.05$) indicated 9 biochemical pathways that were significantly deregulated between early and late fasting in seals ($p<0.05$) (Supplemental Table 2). The most perturbed pathways included ketone and branched-chain amino acid metabolism.

Collectively, the changes in baseline concentrations and path analyses demonstrate an increase in fatty acid and ketone pool size, coupled with a decrease in amino acids and primary metabolites in late-fasted seals indicating that fasting duration shifts substrate metabolism toward an increase in lipolysis, β-oxidation, and ketone metabolism as the primary sources of energy, associated with a robust conservation of protein (lean tissue) (Figure 1).

3.3.2 Despite protracted fasting, insulin facilitates a shift toward fatty acid metabolism

The time course trajectories following insulin infusion identified 23 of 171 metabolites with significantly ($p<0.05$) perturbed AUC values between early and late fasting (Table 1) indicating that fasting duration alters the tissue's responsiveness to insulin. Fatty acid metabolism in response to insulin is characterized by decreased AUC values between early and late fasting, with all AUC values of FFA in late fasting being negative (Table 1). The responses of ketones and EC to the insulin infusion were similar suggesting that lipolytic and endocannabinoid pathways share common insulin-mediated processes (Figure 2). In early fasting, these metabolite levels decreased, reaching a nadir at 30 min post-infusion. For FFA, levels returned to baseline by 60 min and remained so for the rest of the measurement period, whereas ketones and EC peaked at 60 min before returning to baseline at 120 min (Figure 2). Initially, insulin increased primary metabolites and amino acids before levels reached a nadir at 60 min and returned to baseline by 120 min (Figure 2).

In late fasting, FFA and EC decreased similarly, reaching a nadir at 60 min before returning to baseline by 120 min (Figure 2). Ketones displayed a transient increase before a nadir at 60 min and returning to baseline by 120 min (Figure 2). Primary metabolites and amino acids AUC values increased (with all values being positive with the exception of isoleucine). In contrast to the early fasting response, insulin increased amino acid levels reaching a peak at 60 min before decreasing to baseline at 120 min (Figure 2).

Principal component analysis (PCA) revealed that the maximum geometric distance occurred at 60 min for both early and late fasting, regardless of trajectory (Figure 3A, C). In the early fast the majority (72%) of metabolite trajectories return to baseline (+/− 30% of baseline) at 120 min. In contrast, the majority of metabolite concentrations in the late fast (53%) did not return to baseline (+/− 30% of baseline), and present a residual difference at 120 min

post-infusion. Collectively, the integrated insulin responses (AUC) and PCA data reveal that in late-fasted animals (characterized by insulin resistance) the available pool of free fatty acids is depleted quickly, and likely shuttled into the TCA cycle. Conversely, the insulin-induced increases in primary metabolites (AUCs) are indicative of activation of gluconeogenic precursors (Figures 3C–D, 4C–D).

3.3.4 Fasting duration alters the metabolic response to insulin

Hierarchical clustering identified groups of metabolites with similar trajectories in both early and late fasting as well as in a joined cohort of both early and late fast. The seven main classes of metabolites grouped into four distinct clusters in early and 4 clusters in late fasting (Figure 4C–D). Clustering based on hierarchical (Figure 4C–D) and non-hierarchical methods on self-organizing maps (Figure 4A–B) aligned well with each other. In early fasting, ketone, EC, and TCA cycle metabolite profiles demonstrated a common peak and clustered together. Trajectories for amino acids and primary metabolites were closely related. The FFA profiles were characterized by a rapid, initial decrease recovering by 60 min, which was distinctive from the profiles for amino acids and primary metabolites.

In late fasting, FFA and EC were correlated and clustered together with a decrease at 60 min (Figure 4C–D). A comparison of the metabolomic profiles between early- and late-fasted animals in response to the insulin infusion demonstrated profound shifts in cellular metabolism and biochemical processes as a function of fasting duration. Cluster analysis allowed for assessment of the transition from negative to positive AUC values with fasting duration.

3.4 Discussion

The reliance of the elephant seal on lipid oxidation (RQ = 0.73)[7,49] to meet its energetic demands during their prolonged bouts of fasting, which are a natural and evolved component of the animal's life history, is unorthodox, if not unique. Animals, including humans, shift from reliance on one substrate (usually glucose initially) to another (lipids followed by protein) over the course of food deprivation or scarcity[50], but rarely is the RQ fixed over a prolonged period of food deprivation. What makes this evolved behavior even more fascinating is that the animals develop *reversible, tissue-specific* insulin resistance[5,9-10,26]. Furthermore, fasting duration is associated with a decrease in plasma insulin[9,26,51] suggesting that target tissues may be desensitized to insulin during this time to help maintain circulating glucose levels over the protracted fast. Despite exhibiting an insulin resistance-like phenotype and tolerating circumstances that would otherwise be considered detrimental, the fact that elephant seal pups developmentally thrive is truly remarkable. Here we show that: **(1)** despite an evolved mechanism to suppress circulating insulin with fasting duration, tissues remain responsive to insulin, **(2)** despite the reliance on lipid oxidation to fulfill their energetic needs, insulin has profound effects on endocannabinoids, ketones, and primary carbon metabolites, and **(3)** fasting

duration (and thus the development of insulin resistance) has remarkable effects on modulating insulin-mediated metabolism of endocannabinoids, fatty acids and TCA cycle components. These findings are significant because they shed light on the evolution of insulin actions on substrate metabolism in an animal model of reversible insulin resistance at a time when the identification of alternative models for the study of metabolic disorders is at a premium.

An important and significant component of the current study was the use of a combination of untargeted and targeted metabolomics with the aims of identifying metabolic alterations associated with fasting status and insulin resistance in a large mammal. Furthermore, a thorough examination of the metabolic responses of early- and late-fasted seals to exogenous insulin provides previously unrealized insight into the metabolic programming or biochemical shifts induced by insulin.

3.4.1 Fasting Duration Shifts the Metabolic Trajectories to Insulin Infusion

An important and very compelling finding stemming from the insulin infusion studies is the extensive metabolomic characterization of the effects of fasting duration (and thus IR-like condition) on the cellular responses to insulin. Early- and late-fasted seals exhibit different metabolic profiles in responses to insulin indicating that fasting duration shifts the cellular sensitivity to insulin. The most striking distinctions were the responses in circulating FFAs, endocannabinoid and endocannabinoid-like metabolites, and ketones. In late-fasted seals, FFAs and the endocannabinoids, AEA and OEA, decreased during the first 60 min of insulin infusion followed by a return to baseline values. In hibernating bears, the growth hormone induced increase in insulin was associated with nearly a fourfold increase in FFA 7 days post-infusion suggestive of increased lipolysis[52]. The corresponding reductions in AEA and OEA are consistent with previous data demonstrating that endocannabinoid and N-acylethanolamides reflect changes in FFA concentrations[53]. On the contrary, 3-hydroxybutyric acid decreased during the first 60 min of insulin infusion and remained suppressed suggesting that under normal conditions insulin promotes the complete metabolism of ketones so that they do not accumulate. In contrast, the growth hormone-induced increase in insulin stimulated over a 6-fold increase in plasma β-hydroxy butyrate in hibernating bears[52]. The differential responses compared to hibernating bears most likely reflect differences in energetic demands between the two animals as hibernating bears are hypothermic and metabolically quiescent while fasting seal pups are metabolically active and normothermic.

A consequence of diabetes is the accumulation of ketones, which may be the result of increased hepatic production and/or incomplete metabolism by extrahepatic tissues[54]. Furthermore, the corresponding trajectories in FFAs were inversely mirrored by carbohydrates suggesting that exogenous insulin in late-fasted seals facilitates a preferential switch from lipid oxidation to glucose utilization and the promotion of glycolysis consistent with the Randle cycle[55]. This is further supported by an increase in pyruvic acid with insulin infusion in late-fasted seals, which was not observed in early-fasted seals, suggesting that this shift toward a Randle cycle may be a significant metabolic shift to facilitate

the adipose-specific insulin resistance[56-57]. Many of the TCA intermediates exhibited a similar response to insulin suggesting that these intermediates are derived from carbohydrate metabolism rather than fatty acid oxidation or amino acid catabolism. If insulin has the potential to preferentially shift substrate utilization as suggested by the data, then this may help explain why insulin levels remain relatively low and decrease with fasting duration, ultimately, helping to support a fixed RQ of 0.73. Conversely, when the animals begin to feed in cold-water environments, a shift toward a reduced metabolic dependence on lipid oxidation would allow the seals to conserve fat stores (insulation), and increase carbohydrate metabolism. Nonetheless, these data demonstrate the very dynamic effects of insulin that would otherwise be masked by attempts to reconcile based solely on plasma levels.

The switch to glucose and related-carbohydrate metabolism in late-fasted seals during insulin infusion may also explain the observed trajectories in most amino acids, particularly alanine. During baseline, late-fasted seals exhibited marked reductions in several amino acids compared to early-fasted seals, likely due to a combination of increased anaplerosis of ketogenic and gluconeogenic precursors, and a decrease in proteolysis (protein catabolism/ lean-tissue sparing). This is consistent with what has been reported previously[4,6,58]. However, during insulin infusion amino acids, particularly alanine, mimicked the metabolic trajectories of carbohydrates. Alanine is particularly relevant given its importance in protein synthesis (mainly in the muscles) as well as nitrogen disposal from peripheral tissue to the liver (where it is transaminated back to pyruvate). Pyruvate can then either be oxidized or converted to glucose via gluconeogenesis[59]. Collectively, the aforementioned changes in late-fasted seals during insulin infusion suggest that: **(1)** the reliance on fatty acid oxidation is decreased, **(2)** the utilization of carbohydrates is increased, **(3)** circulating amino acids for protein synthesis is altered, and **(4)** nitrogen disposal is increased, all of which may be a consequence of the buildup of nitrogenous waste associated with amino acid catabolism that occurs with food deprivation or starvation[50,60].

Also of note is the apparent lag in response to insulin infusion in late- compared to early-fasted seals. During early fasting, insulin infusion most often resulted in rapid, acute changes in metabolite concentrations that returned to baseline within the measurement period. Conversely, in late-fasted seals the responses were mostly either inverse, in cases where preferential usage of metabolic pathways changed, or their behaviors were similar with the exception that there was a lag affect in which concentrations did not return to baseline over the measurement period. This difference in the timing of responses to insulin between early- and late-fasted seals suggests that fasting duration alters the initiation of compensatory biochemical mechanisms that contribute to the maintenance of substrate homeostasis, particularly glucose. Given insulin's profound effects on perturbing metabolic pathways in elephant seal pups, this may partially explain the natural decrease in plasma insulin as an evolved adaptation to prolonged fasting as a means to: **(1)** alleviate the insulin-induced suppression of lipolysis, **(2)** abate increased cellular metabolism and the subsequent energetic burden (i.e., insulin-induced anabolism) in the absence of caloric intake, and **(3)** facilitate cellular homeostasis. If so, this would help

explain why impaired insulin signaling has such dire consequences on cellular metabolism and appropriate substrate metabolism in non-adapted mammals.

3.4.2 Late fasted seals model an insulin resistance-like phenotype

The increase in baseline free fatty acid values in late fasting, along with the concomitant decrease in primary carbon metabolites, is indicative of an insulin resistance-like (IR-like) phenotype. Temporary and reversible insulin resistance (IR) is a common response in mammals to conserve circulating glucose, but the fasting durations between those mammals and seals are not comparable. Additionally, the unique metabolic network constructed for seals here provides a framework to differentiate reversible, long-term IR-like phenotype and true insulin resistance. Similar to IR, the IR-like phenotype observed in seals is characterized by elevated plasma FFA and glucose levels. While the data clearly demonstrate that tissues remain responsive to insulin, the changes in plasma metabolites in response to insulin are shifted by approximately 30 minutes suggesting that the sensitivity to insulin in peripheral target tissues is decreased. Thus, in addition to relatively low plasma insulin concentrations in fasting seal pups[5,9,26-27,51] a decrease in tissue sensitivity is an adaptation to facilitate the development of an IR-like condition, which collectively, is important for the maintenance of circulating glucose to support the metabolism of glucose-dependent tissues.

Additional comparisons of response curves to insulin reveal further unique differences. Notably, insulin increased plasma amino acid levels indicative of protein catabolism, which is not typically seen in other models of insulin resistance. However, this unique response is likely an evolved adaptation to facilitate the development of an IR-like phenotype that is not associated with detrimental outcomes. It is also important to note that the amino acid response to insulin is the opposite of their unstimulated, fasting metabolic state where protein is rigorously conserved. Collectively, these data define an IR-like phenotype that may characterize an intermediary phenotype and differentiate it from the human condition, which is associated with severe metabolic derangements and consequences, and the current condition, which is evolved and a natural component of the animal's life history and absent of irrecoverable metabolic detriments.

3.4.3 Baseline Changes

Consistent with the findings by others[5,10,61-63], we observed an increase in baseline plasma free medium- (caprate and myristate) and long-chain (oleate, vaccinate, linoleate, EPA, and palmitate) fatty acids in late-fasted seals indicating that lipolysis increased, likely as a consequence of the increased demand for energy derived from the oxidation of FFA. Our findings are corroborated by previous data demonstrating that adipose lipases (LPL and ATGL) involved in regulation of non-esterified fatty acids (NEFA) are elevated with fasting in elephant seal pups[10]. Additionally, circulating ketones (acetoacetate and 3-hydroxybutyric acid) increased in late compared to early fasting animals[64]. During food deprivation and insulin resistance, ketones are frequently elevated, a consequence of the increased reliance on beta-oxidation of FFA and amino acid catabolism[65].

In addition to the increase in ketones and FFAs, the endocannabinoid AEA was increased in late-fasted pups. Insulin resistance or diabetes is known to impact endocannabinoid metabolism[66-67]. The regulation of the endocannabinoids in adipocytes is compromised during insulin resistance, leading to enhanced endocannabinoid signaling[66]. Consequently, this dysregulation of ECs impairs metabolism resulting in changes in fatty acid synthesis and utilization, insulin sensitivity, and glucose utilization[68]. The impact of alterations in EC and EC-like metabolism on insulin sensitivity and metabolic syndrome is of particular interest and remains a focal point in future studies.

It has been postulated that up-regulation of the TCA cycle accommodates increased rates of FFA oxidation to prevent ketoacidosis via the accumulation of ketone bodies and to maintain endogenous glucose production[27]. Specifically, when glucose is limited or being preserved, anaplerotic reactions can supply the TCA cycle with intermediates[27]. In our study, ketogenic (tryptophan and threonine) and gluconeogenic precursors (alanine, asparagine, tryptophan, and threonine) decreased in late-fasted seals suggesting that the use of anaplerotic pathways increased with fasting[69]. Interestingly, the characteristic increase in circulating branched-chain amino acids with the exception of isoleucine, commonly observed in insulin resistant, obese diabetics[63,70-71], was not observed in fasting seals. On the contrary, valine decreased in late-fasted seals. However, similar to previously published observations of decreased glucose and insulin levels in late-fasted seals[5], not all metabolic changes resembled an obesity-related, insulin resistance phenotype. Thus, the observed alterations in branched-chain amino acid metabolism may have evolved differentially in elephant seals to provide a unique metabolic pathway during prolonged fasting that compensates for the fasting-associated insulin resistance described in fasting seal pups[10].

Consistent with the observed and previously reported[26] decreases in glucose with fasting duration, other circulating sugars and sugar-alcohols were also reduced in late- versus early-fasted seals. This may suggest that utilization of other carbohydrate sources is increased to conserve circulating glucose levels as much as possible for use by glucose-dependent tissues. Circulating 1,5-anhydroglucitol, a marker of glycemic control[64,72-73], was increased in late-fasted seals consistent with previously reported changes in both lactating and post-weaned pups[64]. The lack of a change in 1,5-anhydroglucitol in response to insulin suggests that any perturbations in carbohydrate metabolism (i.e., glycogenolysis) by insulin were not sufficient to induce detectable changes in 1,5-anhydroglucitol, which is consistent with the fasting-associated increases in baseline levels in the presence of decreasing insulin levels[51,64].

3.4.4 Perspectives

The present study describes the shifts in numerous metabolic pathways in fasted, insulin-infused Northern elephant seal pups that are characterized by temporary, reversible insulin resistance[10]. In particular, increases in fasting plasma ECs, FFAs, and ketones as well as decreased substrates for glutathione production were representative of this seemingly pathological, however, well-adapted condition. Nonetheless, the increase in 1,5-

anhydroglucitol and decrease in AAs suggest that seal muscle may be comparatively more insulin sensitive than their adipose tissue, a contention supported by assessment of the phosphorylation of insulin receptor and other signaling proteins in adipose and muscle[5,10]. Previously published data on gene expression, enzyme activity, and endocrine regulation as well as glucose and triglyceride metabolism support the metabolomics results described herein[5,26-27,49]. Thus, metabolomics proved to be an insightful tool to more thoroughly characterize this metabolic phenotype and to complement results gathered previously. Likewise, the results further support the establishment of the Northern elephant seal as a useful, tractable large mammalian model for the investigation of temporary, reversible insulin resistance. The use of metabolomic approaches to compliment the suite of other studies in seals clearly illustrates the dynamic effects of insulin and its potential importance in regulating substrate metabolism during prolonged food deprivation in a large mammal naturally adapted to such an extreme behavior.

3.5 Significance Statement

Insulin resistance is a complicated biological process, but it can be temporary and reversible in many mammals. Here we employed a metabolomics approach to illustrate the shifts in numerous metabolic pathways in fasted, insulin-infused Northern elephant seal pups that are characterized by temporary, reversible insulin resistance. The evolution of insulin effects appears to be extremely dynamic and potentially very perplexing especially in a large mammal that naturally exhibits relatively low levels. The present study highlights how the use of plasma levels alone to interpret the hormone's function could be problematic, and the dynamic effects of insulin and its potential importance in regulating substrate metabolism during prolonged food deprivation in a large mammal naturally adapted to such an extreme behavior.

3.6 Supplementary Material

Refer to Web version on PubMed Central for supplementary material.

3.7 Acknowledgments

We thank M. Thorwald for assisting with sample collection.

Funding: J.A.V. was supported by a National Institutes of Health National Heart, Lung, and Blood Institute

Supplement to Support Diversity (R01HL09176-S). R.M.O. was partially supported by N.I.H. N.H.L.B.I. Career Development Award (K02HL103787). F.V.F. is grateful for the support of grant CA154887 from the National

Institutes of Health, National Cancer Institute, University of California, Cancer Research Coordinating Committee

CRN-17-427258, National Science Foundation, University of California Senate Graduate Research Council, and

Health Science Research Institute program grants. Research funded by N.I.H. N.H.L.B.I. (R01HL09176), and N.I.H. West Coast Metabolomics Center (U24 DK097154). Additional support was provided to J.W.N by the USDA (Intramural Project 2032-51530-022-00D). The USDA is an equal opportunity employer and provider.

3.8 References

1. Sonksen P, Sonksen J. Insulin: understanding its action in health and disease. *Br J Anaesth*. 2000;85(1):69-79. PMID: 10927996.

2. DeFronzo RA, Soman V, Sherwin RS, Hendler R, Felig P. Insulin binding to monocytes and insulin action in human obesity, starvation, and refeeding. *J Clin Invest*. 1978;62(1):204-213. PMID: 350903.

3. Adams SH, Costa DP. Water conservation and protein metabolism in Northern elephant seal pups during the postweaning fast. *J Comp Physiol B*. 1993;163(5):367-373. PMID: 8254117.

4. Houser DS, Costa DP. Protein catabolism in suckling and fasting Northern elephant seal pups (*Mirounga anglstirostris*). *J Comp Physiol B*. 2001;171(8):635-642. PMID: 11765972.

5. Viscarra JA, Rodriguez R, Vázquez-Medina JP, et al. Insulin and GLP-1 infusions demonstrate the onset of adipose-specific insulin resistance in a large fasting mammal: potential glucogenic role for GLP-1. *Physiol Rep*. 2013;1(2):e00023. PMID: 23997935.

6. Crocker DE, Webb PM, Costa DP, Le Boeuf BJ. Protein catabolism and renal function in lactating Northern elephant seals. *Physiol Zool*. 1998;71(5):485-491. PMID: 9754525.

7. Ortiz CL, Costa DP, Le Boeuf BJ. Water and energy flux in elephant seal pups fasting under natural conditions. *Physiol Zool*. 1978;51(2):166-178.

8. Karpe F, Dickmann J, Frayn KN. Fatty acids, obesity, and insulin resistance: time for a reevaluation. *Diabetes*. 2011;60(10):2441-9. PMID: 21948998.

9. Viscarra JA, Champagne CD, Crocker DE, Ortiz RM. 5'AMP-activated protein kinase activity is increased in adipose tissue of Northern elephant seal pups during prolonged fasting-induced insulin resistance. *J Endocrinol*. 2011;209(3):317-325. PMID: 21429964.

10. Viscarra JA, Vázquez-Medina J, Rodriguez R, et al. Decreased expression of adipose CD36 and FATP1 are associated with increased plasma non-esterified fatty acids during prolonged fasting in Northern elephant seal pups (*Mirounga angustirostris*). *J Exp Biol*. 2012;215(Pt 14):2455-64. PMID: 22723485.

11. Adams SH, Costa DP, Winter SC. Plasma carnitine in fasting neonatal and adult Northern elephant seals. *Am J Physiol*. 1992;263(3 Pt 1):E570-574. PMID: 1415538.

12. Koves TR, Ussher JR, Noland RC, et al. Mitochondrial overload and incomplete fatty acid oxidation contribute to skeletal muscle insulin resistance. *Cell Metab*. 2008;7(1):45-56. PMID: 18177724.

13. Adams SH, Hoppel CL, Lok KH, et al. Plasma acylcarnitine profiles suggest incomplete long-chain fatty acid beta-oxidation and altered tricarboxylic acid cycle activity in type 2 diabetic African-American women. *J Nutr*. 2009;139(6):1073-1081. PMID: 19369366.

14. Rhee EP, Cheng S, Larson MG, et al. Lipid profiling identifies a triacylglycerol signature of insulin resistance and improves diabetes prediction in humans. *J Clin Invest*. 2011;121(4):1402-1411. PMID: 21403394.

15. Wang TJ, Larson MG, Vasan RS, et al. Metabolite profiles and the risk of developing diabetes. *Nat Med*. 2011;17(4):448-453. PMID: 21423183.

16. Mihalik SJ, Michaliszyn SF, de las Heras J, et al. Metabolomic profiling of fatty acid and amino acid metabolism in youth with obesity and type 2 diabetes: evidence for enhanced mitochondrial oxidation. *Diabetes Care*. 2012;35(3):605-611. PMID: 22266733.

17. Floegel A, Stefan N, Yu Z, et al. Identification of serum metabolites associated with risk of type 2 diabetes using a targeted metabolomic approach. *Diabetes*. 2013;62(2):639-648. PMID: 23043162.

18. Liu L, Feng R, Guo F, Li Y, Jiao J, Sun C. Targeted metabolomic analysis reveals the association between the postprandial change in palmitic acid, branched-chain amino acids and insulin resistance in young obese subjects. *Diabetes Res Clin Pract*. 2015;108(1):84-93. PMID: 25700627.

19. Palmer ND, Stevens RD, Antinozzi PA, et al. Metabolomic profile associated with insulin resistance and conversion to diabetes in the Insulin Resistance Atherosclerosis Study. *J Clin Endocrinol Metab*. 2015;100(3):E463-468. PMID: 25423564.

20. Li LO, Hu YF, Wang L, Mitchell M, Berger A, Coleman RA. Early hepatic insulin resistance in mice: a metabolomics analysis. *Mol Endocrinol*. 2010;24(3):657-666. PMID: 20150186.

21. Wopereis S, Rubingh CM, van Erk MJ, et al. Metabolic profiling of the response to an oral glucose tolerance test detects subtle metabolic changes. *PLoS One*. 2009;4(2):e4525. PMID: 19242536.

22. Zhao X, Peter A, Fritsche J, et al. Changes of the plasma metabolome during an oral glucose tolerance test: is there more than glucose to look at? *Am J Physiol Endocrinol Metab*. 2009;296(2):E384-393. PMID: 19066319.

23. Lanza IR, Zhang S, Ward LE, Karakelides H, Raftery D, Nair KS. Quantitative metabolomics by HNMR and LC-MS/MS confirms altered metabolic pathways in diabetes. *PLoS One*. 2010;5(5):e10538. PMID: 20479934.

24. Spégel P, Danielsson APH, Bacos K, et al. Metabolomic analysis of a human oral glucose tolerance test reveals fatty acids as reliable indicators of regulated metabolism. *Metabolomics*. 2010;6:56-66.

25. Du F, Virtue A, Wang H, Yang XF. Metabolomic analyses for atherosclerosis, diabetes, and obesity. *Biomark Res*. 2013;1(1):17. PMID: 24252331.

26. Viscarra JA, Vázquez-Medina JP, Crocker DE, Ortiz RM. Glut4 is upregulated despite decreased insulin signaling during prolonged fasting in Northern elephant seal pups. *Am J Physiol Regul Integr Comp Physiol*. 2011;300(1):R150-154. PMID: 20980624.

27. Champagne CD, Houser DS, Fowler MA, Costa DP, Crocker DE. Gluconeogenesis is associated with high rates of tricarboxylic acid and pyruvate cycling in fasting Northern elephant seals. *Am J Physiol Regul Integr Comp Physiol*. 2012;303(3):R340-52. PMID: 22673783.

28. Scholz M, Fiehn O. SetupX – a public study design database for metabolomic projects. *Pac Symp Biocomput*. 2007;169-180. PMID: 17990490.

29. Fiehn O. Extending the breadth of metabolite profiling by gas chromatography coupled to mass spectrometry. *Trends Analyt Chem*. 2008;27(3):261-269. PMID: 18497891.

30. Kind T, Tolstikov V, Fiehn O, Weiss RH. A comprehensive urinary metabolomic approach for identifying kidney cancer. *Anal Biochem*. 2007;363(2):185-195. PMID: 17316536.

31. Fiehn O, Wohlgemuth G, Scholz M. Setup and annotation of metabolomic experiments by integrating biological and mass spectrometric metadata. *Proc Lect Notes Bioinformatics*. 2005;224-239.

32. Smedes F. Determination of total lipid using non-chlorinated solvents. *Analyst*. 1999;124:1711-1718.

33. Gladine C, Newman JW, Durand T, et al. Lipid profiling following intake of the omega 3 fatty acid DHA identifies the peroxidized metabolites F4-neuroprostanes as the best predictors of atherosclerosis prevention. *PLoS One*. 2014;9(2):e89393. PMID: 24558496.

34. Luria A, Weldon SM, Kabcenell AK, et al. Compensatory mechanism for homeostatic blood pressure regulation in Ephx2 gene-disrupted mice. *J Biol Chem*. 2007;282(5):2891-2898. PMID: 17135253.

35. Shearer GC, Harris WS, Pedersen TL, Newman JW. Detection of omega-3 oxylipins in human plasma and response to treatment with omega-3 acid ethyl esters. *J Lipid Res*. 2010;51(8):2074-2081. PMID: 19671931.

36. Benjamini Y, Hochberg Y. Controlling the false discovery rate: a practical and powerful approach to multiple testing. *J R Stat Soc Series B Stat Methodol*. 1995;57(1):289-300.

37. Stacklies W, Redestig H, Scholz M, Walther D, Selbig J. pcaMethods – a bioconductor package providing PCA methods for incomplete data. *Bioinformatics*. 2007;23(9):1164-1167. PMID: 17344241.

38. Wiklund S, Johansson E, Sjöström L, et al. Visualization of GC/TOF-MS-based metabolomics data for identification of biochemically interesting compounds using OPLS class models. *Anal Chem*. 2008;80(1):115-122. PMID: 18027910.

39. Palermo G, Piraino P, Zucht HD. Performance of PLS regression coefficients in selecting variables for each response of a multivariate PLS for omics-type data. *Adv Appl Bioinform Chem*. 2009;2:57-70. PMID: 21918616.

40. Phipson B, Smyth GK. Permutation P-values should never be zero: calculating exact P-values when permutations are randomly drawn. *Stat Appl Genet Mol Biol*. 2010;9:Article39. PMID: 21044043.

41. Keun HC, Ebbels TM, Bollard ME, et al. Geometric trajectory analysis of metabolic responses to toxicity can define treatment specific profiles. *Chem Res Toxicol*. 2004;17(5):579-587. PMID: 15144214.

42. Barupal DK, Haldiya PK, Wohlgemuth G, et al. MetaMapp: mapping and visualizing metabolomic data by integrating information from biochemical pathways and chemical and mass spectral similarity. *BMC Bioinformatics*. 2012;13:99. PMID: 22591066.

43. Kanehisa M, Sato Y, Kawashima M, Furumichi M, Tanabe M. KEGG as a reference resource for gene and protein annotation. *Nucleic Acids Res*. 2016;44(D1):D457-462. PMID: 26476454.

44. Kim S, Thiessen PA, Bolton EE, et al. PubChem substance and compound databases. *Nucleic Acids Res*. 2016;44(D1):D1202-1213. PMID: 26400175.

45. Grapov D, Wanichthanarak K, Fiehn O. MetaMapR: pathway independent metabolomic network analysis incorporating unknowns. *Bioinformatics*. 2015;31(16):2757-2760. PMID: 25847005.

46. Cao Y, Jiang T, Girke T. A maximum common substructure-based algorithm for searching and predicting drug-like compounds. *Bioinformatics*. 2008;24(13):i366-374. PMID: 18586736.

47. Xia J, Wishart DS. Web-based inference of biological patterns, functions and pathways from metabolomic data using MetaboAnalyst. *Nat Protoc*. 2011;6(6):743-760. PMID: 21637195.

48. Somo DA, Ensminger DC, Sharick JT, Kanatous SB, Crocker DE. Development of dive capacity in Northern elephant seals (*Mirounga angustirostris*): reduced body reserves at weaning are associated with elevated body oxygen stores during the postweaning fast. *Physiol Biochem Zool*. 2015;88(5):471-482. PMID: 26658245.

49. Houser DS, Crocker DE, Tift MS, Champagne CD. Glucose oxidation and nonoxidative glucose disposal during prolonged fasts of the Northern elephant seal pup (*Mirounga angustirostris*). *Am J Physiol Regul Integr Comp Physiol*. 2012;303(5):R562-570. PMID: 22814669.

50. Cahill GF Jr. Starvation in man. *N Engl J Med*. 1970;282(12):668-75. PMID: 4915800.

51. Ortiz RM, Noren DP, Ortiz CL, Talamantes F. GH and ghrelin increase with fasting in a naturally adapted species, the Northern elephant seal (*Mirounga angustirostris*). *J Endocrinol*. 2003;178(3):533-9. PMID: 12967344.

52. Blumenthal S, Morgan-Boyd R, Nelson R, Garshelis DL, Turyk ME, Unterman T. Seasonal regulation of the growth hormone-insulin-like growth factor-I axis in the American black bear (*Ursus americanus*). *Am J Physiol Endocrinol Metab*. 2011;301(4):E628-636. PMID: 21730258.

53. Joosten MM, Balvers MG, Verhoeckx KC, Hendriks HF, Witkamp RF. Plasma anandamide and other N-acylethanolamines are correlated with their corresponding free fatty acid levels under both fasting and non-fasting conditions in women. *Nutr Metab (Lond)*. 2010;7(49). PMID: 20546561.

54. Jefferies CA, Nakhla M, Derraik JG, Gunn AJ, Daneman D, Cutfield WS. Preventing diabetic ketoacidosis. *Pediatr Clin North Am*. 2015;62(4):857-871. PMID: 26210621.

55. Hue L, Taegtmeyer H. The Randle cycle revisited: a new head for an old hat. *Am J Physiol Endocrinol Metab*. 2009;297(3):E578-591. PMID: 19531645.

56. McGarry JD. Glucose-fatty acid interactions in health and disease. *Am J Clin Nutr*. 1998;67(3 Suppl):500S-504S. PMID: 9497160.

57. McGarry JD. Banting lecture 2001: dysregulation of fatty acid metabolism in the etiology of type 2 diabetes. *Diabetes*. 2002;51(1):7-18. PMID: 11756317.

58. Houser DS, Crocker DE. Age, sex, and reproductive state influence free amino acid concentrations in the fasting elephant seal. *Physiol Biochem Zool*. 2004;77(5):838-846. PMID: 15547801.

59. Rosen F, Roberts NR, Nichol CA. Glucocorticosteroids and transaminase activity. I. Increased activity of glutamicpyruvic transaminase in four conditions associated with gluconeogenesis. *J Biol Chem*. 1959;234(3):476-480. PMID: 13641244.

60. Goodman MN, Larsen PR, Kaplan MM, Aoki TT, Young VR, Ruderman NB. Starvation in the rat. II. Effect of age and obesity on protein sparing and fuel metabolism. *Am J Physiol*. 1980;239(4):E277-E286. PMID: 7425120.

61. Tsatsoulis A, Mantzaris MD, Bellou S, Andrikoula M. Insulin resistance: an adaptive mechanism becomes maladaptive in the current environment - an evolutionary perspective. *Metabolism*. 2013;62(5):622-633. PMID: 23260798.

62. Houser DS, Champagne CD, Crocker DE. A non-traditional model of the metabolic syndrome: the adaptive significance of insulin resistance in fasting-adapted seals. *Front Endocrinol (Lausanne)*. 2013;4:164. PMID: 24198811.

63. Friedrich N. Metabolomics in diabetes research. *J Endocrinol*. 2012;215(1):29-42. PMID: 22718433.

64. Champagne CD, Boaz SM, Fowler MA, Houser DS, Costa DP, Crocker DE. A profile of carbohydrate metabolites in the fasting Northern elephant seal. *Comp Biochem Physiol Part D Genomics Proteomics*. 2013;8(2):141-151. PMID: 23542762.

65. Stojanovic V, Ihle S. Role of beta-hydroxybutyric acid in diabetic ketoacidosis: a review. *Can Vet J*. 2011;52(4):426-430. PMID: 21731100.

66. D'Eon TM, Pierce KA, Roix JJ, Tyler A, Chen H, Teixeira SR. The role of adipocyte insulin resistance in the pathogenesis of obesity-related elevations in endocannabinoids. *Diabetes*. 2008;57(5):1262-1268. PMID: 18276766.

67. Di Marzo V, Verrijken A, Hakkarainen A, et al. Role of insulin as a negative regulator of plasma endocannabinoid levels in obese and nonobese subjects. *Eur J Endocrinol*. 2009;161(5):715-722. PMID: 19745037.

68. Naughton SS, Mathai ML, Hryciw DH, McAinch AJ. Fatty acid modulation of the endocannabinoid system and the effect on food intake and metabolism. *Int J Endocrinol*. 2013;2013:361895. PMID: 23762050.

69. Owen OE, Kalhan SC, Hanson RW. The key role of anaplerosis and cataplerosis for citric acid cycle function. *J Biol Chem*. 2002;277(34):30409-30412. PMID: 12087111.

70. McCormack SE, Shaham O, McCarthy MA, et al. Circulating branched-chain amino acid concentrations are associated with obesity and future insulin resistance in children and adolescents. *Pediatr Obes*. 2013;8(1):52-61. PMID: 22961720.

71. Adams SH. Emerging perspectives on essential amino acid metabolism in obesity and the insulin resistant state. *Adv Nutr*. 2011;2(6):445-456. PMID: 22332087.

72. Yamanouchi T, Ogata N, Tagaya T, et al. Clinical usefulness of serum 1,5-anhydroglucitol in monitoring glycaemic control. *Lancet*. 1996;347(9014):1514-1518. PMID: 8684103.

73. Buse JB, Freeman JL, Edelman SV, Jovanovic L, McGill JB. Serum 1,5-anhydroglucitol (GlycoMark): a short-term glycemic marker. *Diabetes Technol Ther*. 2003;5(3):355-363. PMID: 12828817.

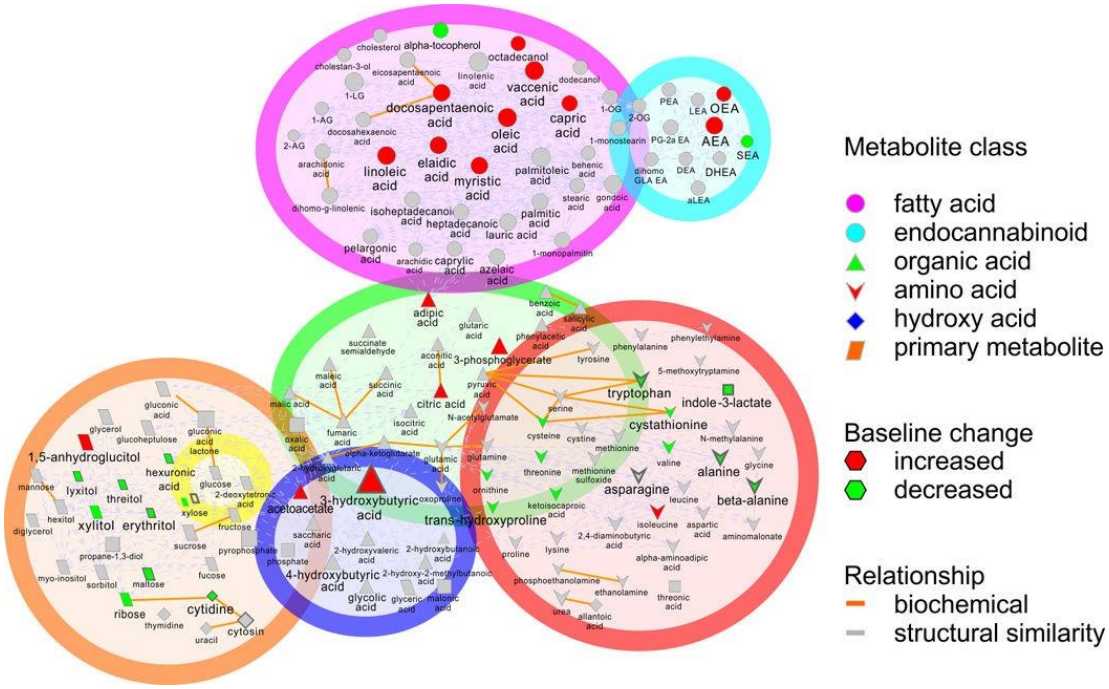

Figure 3.1.

Map of the seven plasma metabolite classes (amino acids, endocannabinoids, fatty acids, glucose, hydroxy acids, organic acids, and primary carbon metabolites) measured illustrating specific metabolites that were significantly different with adjusted p-values below 0.05 at baseline (T_0) between early and late fasting periods in Northern elephant seal pups. The metabolite's pathway and metabolite class are identified.

[a]Mean AUC ± standard deviation

[b]Endocannabinoid concentrations are in nM

[c]Fatty acids concentrations are in μM

[d]FDR adjusted p-value < 0.05

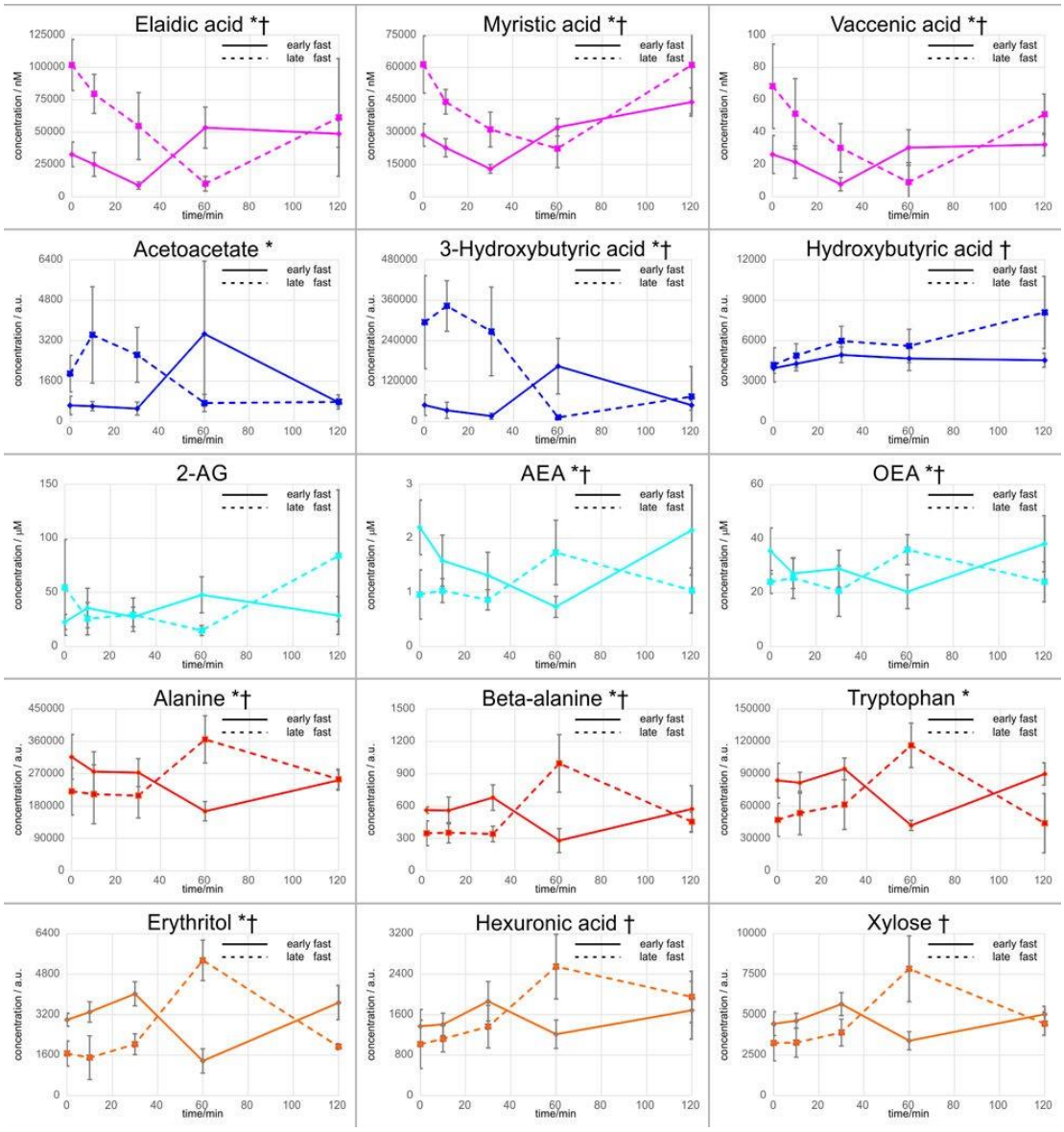

Figure 3.2.

Mean abundances ± standard deviation of metabolic trajectories (t = 0 to 120 min) for those metabolites which indicated significantly (raw p-value < 0.05) different AUCs (Table 1) during insulin infusion between early to late fasting mammals is shown.

†Endocannabinoid and Endocannabinoid-like compounds are presented as nM; *free fatty acids are presented as µM

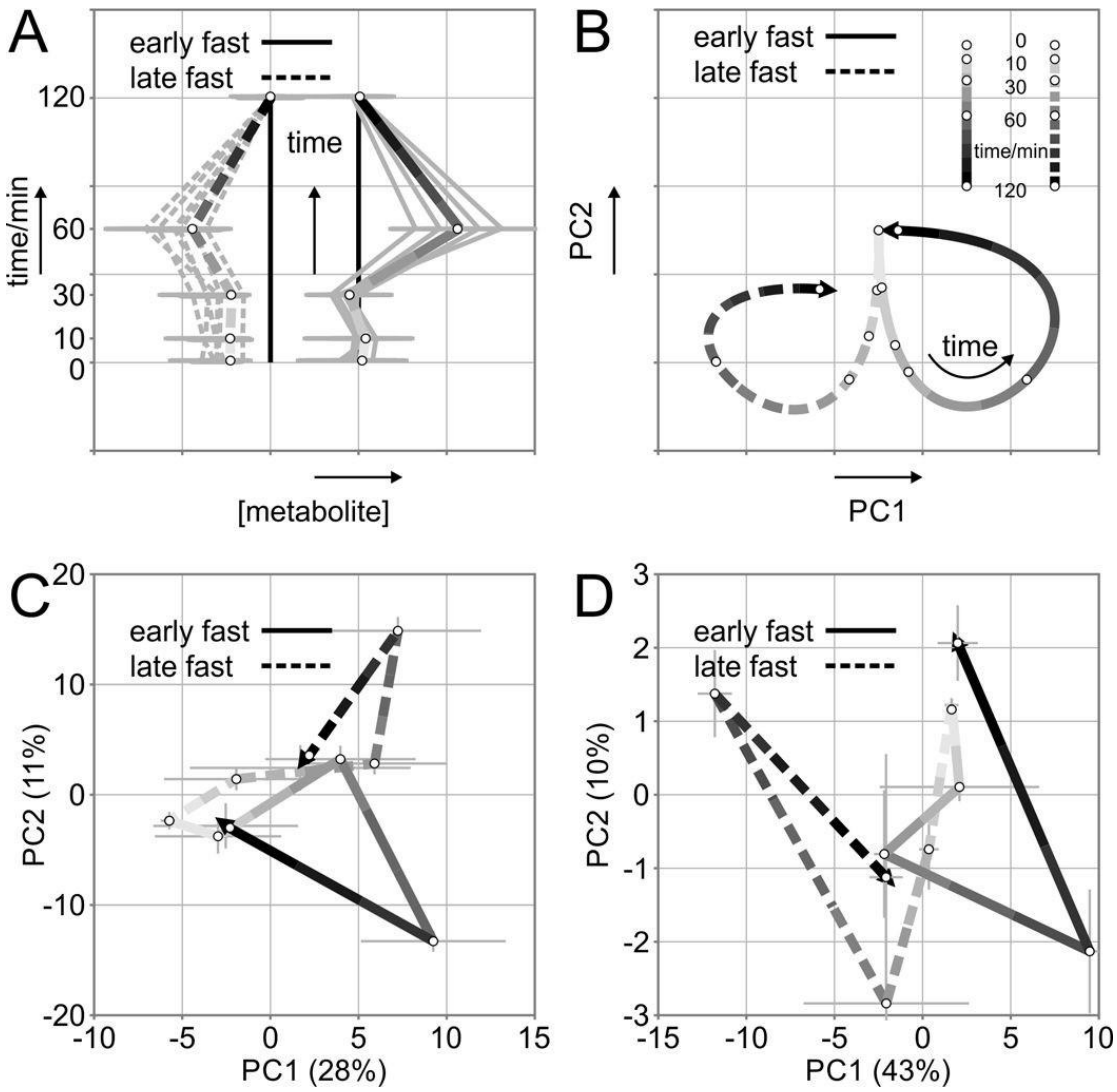

Figure 3.3.

Schematic representation of **a)** metabolite trajectories, and **b)** principal component analysis plot explaining difference in outcome and direction of early- (solid line) and late-fasted (dashed line) response over time. Principal component analysis scores displaying the median points (±standard error) for early- and late-fasted Northern elephant seal pups in response to exogenous insulin infusion for **c)** all measured metabolites and **d)** orthogonal partial least squares discriminant analysis selected top 10% of all discriminating metabolites. The line color becomes darker as the time course runs from the first point (t = 0) to the end point (t = 120 min, arrowhead). Solid lines = early fast, dashed lines = late fast.

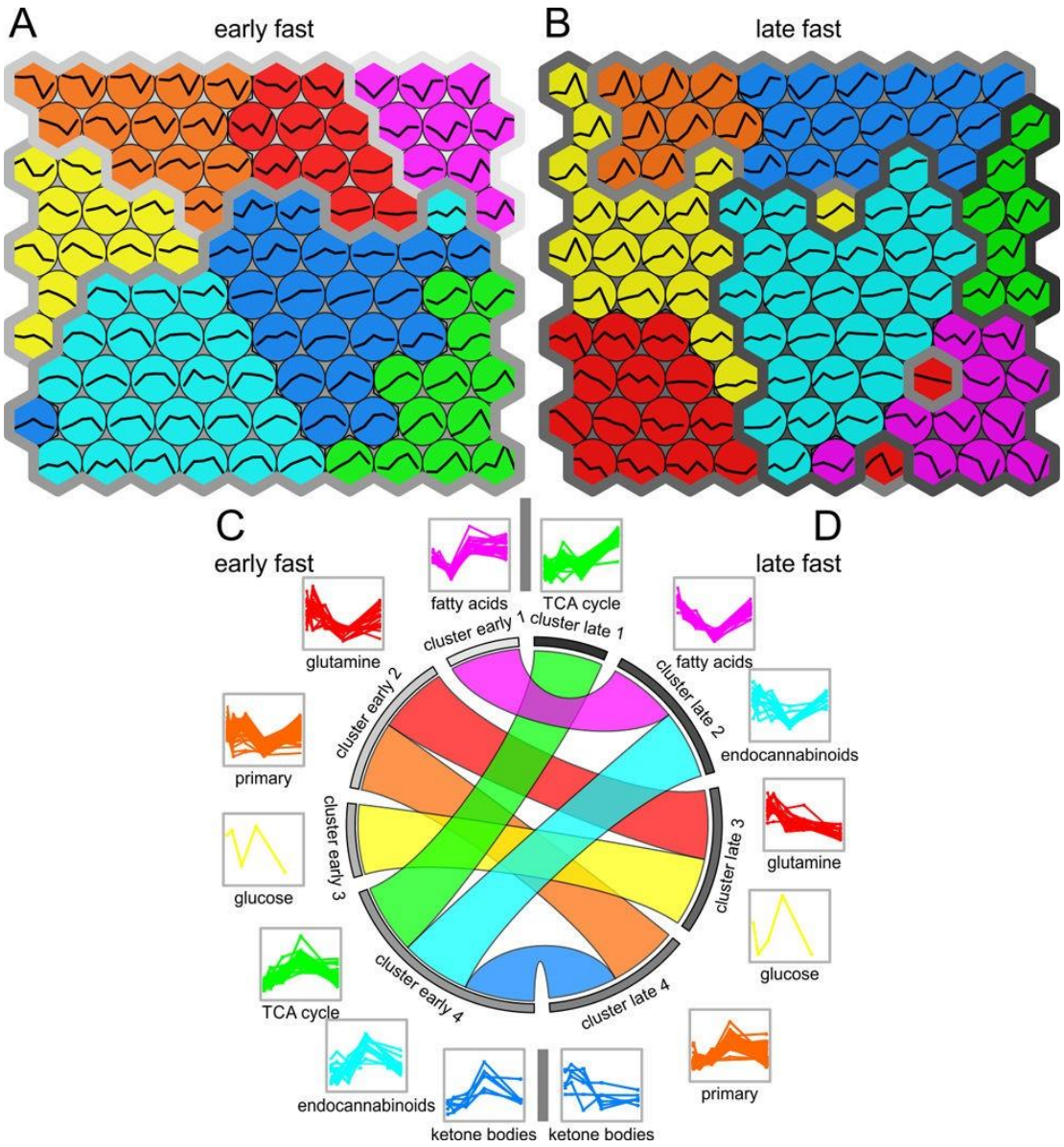

Figure 3.4.

Self-organizing maps of the seven plasma metabolite classes (amino acids, endocannabinoids, fatty acids, glucose, hydroxy acids, organic acids, and primary carbon metabolites) measured for **a)** early- and **b)** late-fasted Northern elephant seal pups following an exogenous insulin infusion. Metabolite trajectories are shown within the map nodes. The seven metabolite classes were grouped by area under the curve (AUC) using hierarchical clustering into four clusters in both **c)** early and **d)** late fast. The circular diagram shows how each metabolite class transitions into a new cluster from early fast (left hemisphere) to late fast (right hemisphere). The metabolite classes are arranged according to their response to insulin with increasing values for AUC from top to bottom.

Table 3.1.

Mean area under the curves (AUC; ± SD) for significantly different ($p < 0.05$) metabolites from the plasma metabolite classes (endocannabinoids, fatty acids, amino acids, carbohydrates, ketone bodies, and organic acids) measured for early- and late-fasted Northern elephant seal pups. The metabolite's pathway and metabolite class are identified.

Metabolite	Pathway	Metabolite class	Early	Late
Anandamide (AEA)	Endocannabinoid metabolism	Endocannabinoid	27 ± 71	−73 ± 27
Oleoylethanolamide (OEA)	Endocannabinoid metabolism	Endocannabinoid	269 ± 690	−627 ± 490
Myristic acid (C14:0)	Lipid metabolism	Fatty acid	36600 ± 7.2e+05	−2.4e+06 ± 1.7e+06
Palmitic Acid (C16:0)	Lipid metabolism	Fatty acid	−3320 ± 6000	−13700 ± 6400*
Isoheptadecanoic acid (C17:0)	Lipid metabolism	Fatty acid	−7910 ± 110000	−137000 ± 47000
Vaccenic Acid (C18:1n7)	Lipid metabolism	Fatty acid	−304 ± 1700	−3380 ± 2400
Elaidic acid (C18:1n9)	Lipid metabolism	Fatty acid	4.2e+06 ± 1.6e+06	−5.5e+06 ± 2.3e+06*
Oleic Acid (C18:1n9)	Lipid metabolism	Fatty acid	−3350 ± 11000	−29300 ± 12000*
Linoleic Acid (C18:2n6)	Lipid metabolism	Fatty acid	−93 ± 540	−1290 ± 830
Alanine	Amino acid metabolism	Amino acid	−9.7e+06 ± 4.6e+06	5e+06 ± 6.5e+06
Beta-alanine	Pantothenate and pyrimidine metabolism	Amino acid	−5740 ± 16000	21400 ± 8100
Isoleucine	Amino acid metabolism	Amino acid	−1670000 ± 1e+06	−3.6e+06 ± 1.2e+06
N-acetylglutamate	Amino acid metabolism	Amino acid	−9120 ± 9000	9730 ± 13000
Erythritol	Carbohydrate metabolism	Carbohydrate	607 ± 75000	125000 ± 75000
Hexuronic acid	Carbohydrate metabolism, pentose phosphate pathway, ascorbic acid metabolism	Carbohydrate	18600 ± 31000	81800 ± 43000
Isothreonic acid	Carbohydrate metabolism, ascorbic acid metabolism	Carbohydrate	28400 ± 35000	103000 ± 38000
D-arabitol	Carbohydrate metabolism, pentose phosphate pathway	Carbohydrate	9500 ± 28000	52000 ± 15000
Maltose	Carbohydrate metabolism	Carbohydrate	−78600 ± 51000	34300 ± 87000

D-Xylose	Carbohydrate metabolism	Carbohydrate	21100 ± 90000	179000 ± 78000*
3-Hydroxybutyric acid	Ketogenesis, Ketolysis	Ketone body	3.3e+06 ± 5.7e+06	−1.4e+07 ± 7.2e+06
Hydroxybutyric acid	Ketogenesis, Ketolysis	Ketone body	82600 ± 35000	194000 ± 85000*
Indole-3-lactate	Amino acid metabolism	Organic acid	−2110 ± 31000	58200 ± 24000*
Pyruvic acid	Glycolysis, gluconeogenesis, pyruvate metabolism	Organic acid	6.5e+05 ± 4.9e+05	2.1e+06 ± 7.6e+05*

Symbol

*FDR adjusted p-value <0.05

Chapter Four: A hexokinase isoenzyme switch in human liver cancer cells promotes lipogenesis and enhances innate immunity

During the cancerous transformation of normal hepatocytes into hepatocellular carcinoma (HCC), the enzyme catalyzing the first rate-limiting step of glycolysis, namely the glucokinase (GCK), is replaced by the higher affinity isoenzyme, hexokinase 2 (HK2). Here, we show that in HCC tumors the highest expression level of *HK2* is inversely correlated to GCK expression, and is associated to poor prognosis for patient survival. To further explore functional consequences of the GCK-to-HK2 isoenzyme switch occurring during carcinogenesis, *HK2* was knocked-out in the HCC cell line Huh7 and replaced by *GCK*, to generate the Huh7-*GCK*$^{+}$/*HK2*$^{-}$ cell line. HK2 knockdown and GCK expression rewired central carbon metabolism, stimulated mitochondrial respiration and restored essential metabolic functions of normal hepatocytes such as lipogenesis, VLDL secretion, glycogen storage. It also reactivated innate immune responses and sensitivity to natural killer cells, showing that consequences of the HK switch extend beyond metabolic reprogramming.

Chapter Four: A hexokinase isoenzyme switch in human liver cancer cells promotes lipogenesis and enhances innate immunity

Laure Perrin-Cocon[1,9], Pierre-Olivier Vidalain[1,9], Clémence Jacquemin[1], Anne Aublin-Gex[1], Keedrian Olmstead[2], Baptiste Panthu[1,3], Gilles Jeans Philippe Rautureau[4], Patrice André[1], Piotr Nyczka[5], Marc-Thorsten Hütt[5], Nivea Amoedo[6], Rodrigue Rossignol[6,7], Fabian Volker Filipp[2,8], Vincent Lotteau[1,10] & Olivier Diaz[1,10]

[1]CIRI, Centre International de Recherche en Infectiologie, Univ Lyon, Inserm, U1111, Université Claude Bernard Lyon 1, CNRS, UMR5308, ENS de Lyon, 21 Avenue Tony Garnier, Lyon F-69007, France.

[2]Cancer Systems Biology, Institute for Diabetes and Cancer, Helmholtz Zentrum München, Ingolstädter Landstraße 1, München D-85764, Germany.

[3]Univ Lyon, CarMeN Laboratory, Inserm, INRA, INSA Lyon, Université Claude Bernard Lyon 1, Hôpital Lyon Sud, Bâtiment CENS ELI-2D, 165 Chemin du grand Revoyet, Pierre-Bénite F-69310, France.

[4]Université de Lyon, CNRS, Université Claude Bernard Lyon 1, ENS de Lyon, Centre de RMN à Très Hauts Champs (CRMN), FRE 2034, 5 rue de la Doua, Villeurbanne F-69100, France.

[5]Department of Life Sciences and Chemistry, Jacobs University, Campus Ring 1, Bremen D-28759, Germany.

[6]CELLOMET, Centre de Génomique Fonctionnelle de Bordeaux, 146 Rue Léo Saignat, Bordeaux F-33000, France.

[7]Univ. Bordeaux, Inserm U1211, MRGM, Centre hospitalier universitaire Pellegrin, place Amélie Raba Léon, Bordeaux F-33076, France.

[8]School of Life Sciences Weihenstephan, Technical University München, Maximus-von-Imhof-Forum 3, Freising D-85354, Germany.

[9]These authors contributed equally: Laure Perrin-Cocon, Pierre-Olivier Vidalain.

[10]These authors jointly supervised: Vincent Lotteau, Olivier Diaz. email: vincent.lotteau@inserm.fr; olivier.diaz@inserm.fr

Abstract

During the cancerous transformation of normal hepatocytes into hepatocellular carcinoma (HCC), the enzyme catalyzing the first rate-limiting step of glycolysis, namely glucokinase (GCK), is replaced by the higher affinity isoenzyme, hexokinase 2 (HK2). Here, we show that in HCC tumors the highest expression level of *HK2* is inversely correlated to *GCK* expression, and is associated with poor prognosis for patient survival. To further explore functional consequences of the GCK-to-HK2 isoenzyme switch occurring during carcinogenesis, *HK2*

was knocked out in the HCC cell line Huh7 and replaced by *GCK*, to generate the Huh7-*GCK*$^{+}$/*HK2*$^{-}$ cell line. HK2 knockdown and GCK expression rewired central carbon metabolism, stimulated mitochondrial respiration and restored essential metabolic functions of normal hepatocytes such as lipogenesis, VLDL secretion, glycogen storage. It also reactivated innate immune responses and sensitivity to natural killer cells, showing that consequences of the HK switch extend beyond metabolic reprogramming.

4.1 Introduction

Hepatocellular carcinoma (HCC) is the most common liver cancer and the fourth leading cause of cancer-related death[1]. HCC is closely linked to chronic liver inflammation, chronic viral hepatitis, exposure to toxins, and metabolic dysfunction such as non-alcoholic steatohepatitis (NASH). HCC is of poor prognosis, and treatments are essentially based on surgical resection, liver transplantation or aggressive chemo and/ or radiotherapy. In patients with advanced HCC, broad-spectrum kinase inhibitors are approved[2] but with limited benefit[3]. Effective personalized therapies are needed but their development is impeded by our poor understanding of molecular mechanisms underlying HCC onset and progression. Efforts to characterize the disease on the basis of etiology and outcomes revealed metabolic deregulation as a hallmark of HCC progression[4]. Indeed, metabolic remodeling is critically required for tumor growth, since bioenergetic requirements and anabolic demands drastically increase[5-7]. For instance, HCC cells have lost their ability to secrete very low-density lipoproteins (VLDL), a highly specialized function of hepatocyte and can only secrete low-density lipoproteins (LDL)-like lipoproteins, indicating a defective lipogenesis and/or lipoprotein assembly[8].

Metabolic reprogramming in cancer cells involves the modulation of several enzymes by oncogenic drivers[6]. Targeting these enzymes is now considered as a therapeutic strategy for several types of cancers[6]. Among these enzymes, hexokinase 2 (HK2) stands out because of its elevated or induced expression in numerous cancers, including HCC[9]. Hexokinases control the first rate-limiting step of glucose catabolism by phosphorylating glucose to glucose-6-phosphate (G6P), fueling glycolysis as well as glycogen, pentose phosphate and triglyceride synthesis. The human genome contains four genes encoding distinct hexokinase isoenzymes, named HK1 to HK4 (HK4 is also known as glucokinase or GCK), with distinct enzymatic kinetics and tissue distributions. A fifth putative hexokinase enzyme was recently discovered but has not been fully characterized yet[10]. A switch from GCK to HK2 isoenzymes is occurring during the transition from primary to tumor hepatocytes so that HCC cell lines express HK2 but no longer GCK. HK2 expression level has been correlated with disease progression and dedifferentiation of HCC cells[11]. When HK2 is artificially knocked down in HCC cell lines, glycolysis is repressed, and tumorigenesis is inhibited while cell death increases[9]. In addition, hexokinase function extends beyond metabolism towards autophagy, cell migration, and immunity, suggesting that the GCK-to-HK2 isoenzyme switch has broader consequences than initially suspected[12-15]. Here, we analyzed transcriptomic

data of HCC biopsies and correlated hexokinase isoenzyme expression level with patient survival. This led us to generate a new cellular model of human HCC expressing *GCK* instead of *HK2*. A comparative analysis of *GCK*$^+$ vs *HK2*$^+$ HCC cell lines provided a unique opportunity to look into HK isoenzyme-dependent metabolic features, lipoprotein production and resistance to immune signals of liver cancer cells.

4.2 Results

4.2.1 Relative expression level of GCK and HK2 in HCC patients.

Although an isoenzyme switch from GCK to HK2 has been observed during the carcinogenesis process[16], whether hexokinase isoenzymes expression is predictive of patient survival is unclear. We first analyzed the transcriptomes (RNA-seq data) of 365 HCC biopsies from The Cancer Genome Atlas (TCGA) database[17-18] (Supplementary Data 1). For each HK, the individual gene expression level was used to stratify patients into two subgroups according to Uhlen et al.[18] and overall survival in the two subgroups was determined using a Kaplan-Meier's estimator. Although *HK1* or *HK3* expression level were not associated to patient survival rate (Fig. 1a), highest expression levels of *HK2* as previously described[19] and lowest expression levels of *GCK* in the tumors were associated with a lower survival rate. We thus stratified patients based on the *GCK*/*HK2* expression ratio to combine these two markers (Fig. 1b). When patients were stratified on the basis of *HK2* or *GCK* expression levels, the median survival between the corresponding subgroups differed by 33.8 and 36.5 months, respectively (Fig. 1a). This difference reached 42.8 months when the stratification of patients was based on the *GCK*/*HK2* ratio (Fig. 1b). This demonstrated that the *GCK*/*HK2* ratio outperforms *HK2* or *GCK* expression alone as predictor of patient survival. Finally, correlation coefficients between patient survival in months and *HK2* or *GCK* expression level were determined. For this, we only considered the subset of 130 patients for whom the period between diagnosis and death is precisely known (uncensored data), and performed a Spearman's rank correlation test (Fig. 1c). Patient survival was positively correlated to *GCK* expression but inversely correlated to *HK2* expression in line with the Kaplan-Meier analysis. In addition, *GCK* and *HK2* expression tends to be inversely correlated in tumor samples (Fig. 1c). Therefore, there is a trend for mutual exclusion of *GCK* and *HK2* expression in HCC tumors, and this profile is associated to clinical outcome.

4.2.2 Engineering a cellular model of the hexokinase isoenzyme switch.

To decipher functional consequences of GCK or HK2 expression in a HCC model, we restored GCK expression by lentiviral transduction in the reference HCC cell line Huh7, and knocked-out the endogenous *HK2* gene by CRISPR/Cas9. The exclusive expression of HK2 and GCK in Huh7 and Huh7-*GCK*$^+$/*HK2*$^-$ cell lines, respectively, was validated, while HK1 and HK3 were not expressed (Fig. 2a and Supplementary Fig. 1). The hexokinase activity in the presence of increasing concentration of glucose was determined in protein lysates from the two respective cell lines. Hexokinase activity in Huh7 lysate

reached its maximum at low glucose concentration, presenting a saturation curve according to Michaelis-Menten kinetics (Fig. 2b). In contrast, the hexokinase activity in Huh7-*GCK*$^{+}$/*HK2*$^{-}$ lysates followed a pseudo-allosteric response to glucose[20-21]. Thus, the expected HK2 and GCK activities were observed in the Huh7 and Huh7-*GCK*$^{+}$/*HK2*$^{-}$ cells respectively. The cell proliferation capacity remained identical between the two cell lines (Supplementary Fig. 2). We then compared the genome edited Huh7-*GCK*$^{+}$/*HK2*$^{-}$ and the parental Huh7 cell lines at a transcriptomic, metabolic and immunological level.

4.2.3 Differential lipid metabolism in Huh7 and Huh7-*GCK*$^{+}$/*HK2*$^{-}$.

The intracellular lipid content of the two cell lines was further analyzed. In Huh7-*GCK*$^{+}$/*HK2*$^{-}$, an enrichment in phosphatidylcholine, cholesterol, triglycerides (TG) and free fatty acids was observed compared to Huh7 (Fig. 4a). One major function of hepatocytes is to secrete triglyceride-rich VLDL and this function is altered in HCC cells that secrete smaller lipoproteins with the density of LDL[22-23]. The secretion of lipids and lipoproteins by both cell lines was analyzed after a 24h-culture in the absence of fetal calf serum (FCS) to exclude any participation of exogenous lipids in the production of lipoproteins. Huh7-*GCK*$^{+}$/*HK2*$^{-}$ secreted more free fatty acids than Huh7 while secretion of cholesterol and TG remained unchanged (Fig. 4b).

However, under the same conditions, the secretion of apolipoprotein B (ApoB) by Huh7-*GCK*$^{+}$/*HK2*$^{-}$ was reduced compared to Huh7. Since ApoB is a non-exchangeable protein with only one copy in VLDL and LDL particles, an elevated TG/ApoB ratio indicates that ApoB^{+}-lipoproteins secreted by Huh7-*GCK*$^{+}$/*HK2*$^{-}$ cells are enriched in TG compared to those secreted by Huh7 (Fig. 4c). This was confirmed by the ApoB distribution in density gradient fractions. As expected, lipoproteins secreted by Huh7 sediment at the density of LDL, while those secreted by Huh7-*GCK*$^{+}$/*HK2*$^{-}$ (Fig. 4d) match the density of VLDL found in human plasma or secreted by primary human hepatocytes in culture[24-25]. This indicates that GCK expression is essential for the VLDL assembly/secretion pathway and could explain the loss of this crucial metabolic pathway in hepatoma cells expressing HK2 instead of GCK[26].

4.2.4 Differential activity of the tricarboxylic acid cycle (TCA) in Huh7 and Huh7-*GCK*$^{+}$/*HK2*$^{-}$.

We observed that GCK expression increased the intracellular content in lipids, resulting in accumulation of lipid droplets and secretion of VLDL. A rewiring of cellular metabolism towards energy storage in Huh7-*GCK*$^{+}$/*HK2*$^{-}$ was thus suspected and confirmed by the accumulation of glycogen, creatine and creatine-P (Fig. 5a, b), a feature of functional hepatocytes. To further determine the consequences of replacing HK2 by GCK, we quantified prominent intracellular metabolites via gas chromatography coupled to triple-quadrupole (QQQ) mass spectrometry (GC-MS). Figure 5c shows relative intracellular quantities of metabolites that are significantly different between Huh7 and Huh7-*GCK*$^{+}$/*HK2*$^{-}$. Among differentially represented metabolites, higher levels of glucose, glycerol-3-phosphate and lactic acid were detected in Huh7-*GCK*$^{+}$/*HK2*$^{-}$ cells. Several intermediates of the TCA cycle (succinic acid,

fumaric acid, alpha-ketoglutaric acid), and metabolites directly connected to it (GABA, glutamic acid, glutamine, aspartic acid) were also differentially present between the two cell lines. This supports a modulation of central carbon metabolism at both the level of glycolysis and TCA cycle. This led to investigate glucose catabolism in further details. Glucose consumption and stable isotope incorporation from [U-^{13}C]-glucose into pyruvate were both increased in Huh7-*GCK*$^{+}$/*HK2*$^{-}$ compared to Huh7 cells (Fig. 5d, e). This increased glycolytic flux together with a reduced lactate secretion (Fig. 5d) is likely to account for the elevation of lactate levels and suggest that the increased pyruvate production essentially fuels mitochondrial TCA cycle in Huh7-*GCK*$^{+}$/*HK2*$^{-}$ cells.

Pyruvate entering the mitochondria downstream of glycolysis can be either oxidized by pyruvate dehydrogenase (PDH), producing acetyl-CoA, or converted into oxaloacetate (OAA) by pyruvate carboxylase (PC). Acetyl-CoA and OAA are then combined in the TCA cycle to form citrate. *De novo* lipogenesis requires citrate egress from the TCA cycle to serve as a precursor of cytosolic acetyl-CoA for further synthesis of fatty acids. In Huh7-*GCK*$^{+}$/*HK2*$^{-}$ cells, we observed both an increased activity of PC (Fig. 5f) without changes in protein expression (Fig. 5g and Supplementary Fig. 7a) and an increased phosphorylation of pyruvate dehydrogenase (PDH), which is indicative of a reduced activity of this enzyme (Fig. 5h and Supplementary Fig. 7b). This is consistent with the increased expression of the PDH kinase PDK2 and the decreased expression of the PDH phosphatase PDP2 in Huh7-*GCK*$^{+}$/*HK2*$^{-}$ cells that regulate the PDH phosphorylation state (Fig. 5i). A rebalanced usage of pyruvate in Huh7-*GCK*$^{+}$/*HK2*$^{-}$ cells maintains a functional TCA cycle and supports lipogenesis. In Huh7-*GCK*$^{+}$/*HK2*$^{-}$ cells, we also observed an increased phosphorylation of ATP citrate lyase (ACLY), the first enzyme of the fatty acid synthesis pathway, indicating an enhanced activity of this enzyme (Fig. 5j and Supplementary Fig. 7c). This reaction also regenerates OAA in the cytosolic compartment. Interestingly, transcriptomic data show that PCK1 which converts OAA to phosphoenolpyruvate (PEP), is overexpressed in Huh7-*GCK*$^{+}$/*HK2*$^{-}$ cells compared to Huh7 (FC = 32).

A shift from pyruvate oxidation to carboxylation is observed in cancer cells where succinate dehydrogenase (SDH) is inactivated by mutation and OAA can only be generated through PC activity[27]. SDH inhibition leads to succinate accumulation, especially in activated immune cells[28]. Interestingly, higher levels of succinate and a reduced activity of SDH were measured in Huh7-*GCK*$^{+}$/*HK2*$^{-}$ compared to Huh7 cells (Fig. 5k, l). Even though SDH is also part of the complex II of the mitochondrial respiratory chain, we observed that the overall oxygen consumption was increased in Huh7-*GCK*$^{+}$/*HK2*$^{-}$ (Fig. 5m) with increased basal and maximal respiration, ATP production and spare respiration capacity (Supplementary Fig. 8). Functional analysis of the respiratory chain showed that oxygen consumption in Huh7 and Huh7-*GCK*$^{+}$/*HK2*$^{-}$ cells was mainly dependent on complex I activity (Fig. 5m, n). Thereby, the HK isoenzyme switch rewired the TCA cycle promoting carboxylation of pyruvate into OAA in the presence of a reduced SDH activity and increased respiration through complex I.

4.3 Discussion

Metabolic network rewiring is a hallmark of cancer, although for most tumors, mechanisms at the origin of this metabolic reprogramming have not been elucidated. While GCK, but not HK2, is expressed in normal hepatocytes, the expression of HK2 occurs during cirrhosis and increases as the disease progresses to carcinoma. Several signaling pathways such as hypoxia inducible factors (HIF), peroxisome proliferator-activated receptors (PPAR) and phosphatidylinositol-4,5-bisphosphate 3-kinase (PI3K) might contribute to HK2 induction in fatty liver disease and its evolution towards cirrhosis and carcinogenesis[29-31]. Consequently, HK2 induction has been proposed as a risk marker of HCC development[16]. Analyzing TCGA data from human HCC tumors, we observed that not only high levels of *HK2* but also low levels of *GCK* are of poor prognosis. In contrast, neither *HK1* nor *HK3* expression levels were correlated with survival of HCC patients. GCK expression is very low or not detected in biopsies from a majority of patients (65.8% of patients show RSEM values <10), whereas *HK2* is widely expressed[16] (only 5.8% of patients show RSEM values <10). This probably explains that HK2 expression is a better prognostic marker than GCK for HCC. However, when GCK and HK2 expression were combined into a single ratio, this prognostic marker outperformed HK2 or GCK expression alone. This suggests that both HK2 induction and GCK loss play a role in HCC progression. As HK2 and GCK expression tend to be mutually exclusive, both HK2 induction and GCK downregulation might have consequences on the metabolic reprogramming during malignant transformation of hepatocytes. To compare the functional consequences of the HK isoenzyme switch in HCC, we therefore expressed GCK in the reference HCC cell line Huh7 and knocked-down HK2 expression. Our comparative transcriptomic, metabolic and functional studies demonstrate that the replacement of HK2 by GCK not only restored some essential metabolic functions of normal hepatocytes such as lipogenesis, VLDL secretion and glycogen storage but also reactivated innate immune responses and sensitivity to NK-mediated cell lysis.

HCC cell lines predominantly secrete LDL-like particles, unlike normal hepatocytes, which secrete VLDL. Lipid loading of Huh7 cells with oleic acid can boost the secretion of $ApoB^+$ particles but does not induce a shift from LDL to VLDL density, indicating that intracellular fatty acid accumulation of exogenous origin cannot rescue VLDL production[26]. Here we show that replacing HK2 by GCK in Huh7 cells restored de novo fatty acid synthesis, allowing VLDL assembly/secretion in the absence of exogenous lipids. To our knowledge Huh7-GCK^+/$HK2^-$ is the first human cell model with a functional VLDL secretion pathway. Such a tool will strongly benefit the field of cardiovascular diseases and hepatic steatosis.

De novo fatty acid synthesis from carbohydrates requires an adequate supply in metabolic substrates, especially citrate that is produced by the TCA cycle from incoming pyruvate. The glycolytic entry point into the TCA cycle is controlled by PDH and PC that convert pyruvate into acetyl-CoA or OAA, respectively. Our data revealed that in addition to the increased production of pyruvate from glucose, PC activity is increased whereas PDH is inhibited. This

suggests that pyruvate metabolism is rebalanced in favor of OAA in Huh7-*GCK*$^{+}$/*HK2*$^{-}$ cells, as described in healthy liver. Such a mechanism of anaplerosis is known to replenish TCA cycle intermediates and compensate citrate export out of the mitochondria for lipogenesis fueling. Increased PC activity is observed in both normal and pathological situations, mainly as a result of an increased transcription of the PC gene. In our model, mRNA and protein levels were not affected, indicating that PC activity can be regulated by alternative mechanisms depending on HK isoenzyme expression. This may relate to lower levels of oxalate, a known inhibitor of PC activity, in Huh7-*GCK*$^{+}$/*HK2*$^{-}$ cells (Fig. 5c and Fig. 7 discussed below).

A rebalanced pyruvate usage in favor of OAA is also described for instance in SDH-deficient neuroendocrine tumor cells, where succinate accumulates and PC activity is increased to maintain OAA production, replenish the oxidative TCA cycle and support aspartate synthesis[27]. Interestingly, in comparison to Huh7 cells, succinate and aspartate levels are elevated in Huh7-*GCK*$^{+}$/*HK2*$^{-}$ where SDH activity is reduced, suggesting a direct link between PC and SDH activity in hepatocytes. Several mechanisms inhibiting SDH have been described[32]. Modification of the expression of SDH subunits is unlikely as no variation was observed at the transcriptomic level. Itaconate is a weak inhibitor of SDH produced from aconitate by Immune-responsive gene 1 protein (IRG1; encoded by *ACOD1*), but this metabolite was not detected and IRG1 mRNA was absent from the transcriptome of both cell lines. Whether fumarate or other metabolites are responsible for the reduced SDH activity in GCK-expressing cells remains to be investigated. Finally, SDH-deficient cells and LPS-stimulated macrophages have been shown to elicit a hypoxic-like phenotype through accumulation of large amounts of succinate and stabilization of HIF-1α[33-34]. Despite an elevated succinate steady-state level in Huh7-*GCK*$^{+}$/*HK2*$^{-}$ compared to Huh7 cells, we observed no difference in HIF-1α stabilization neither at basal level nor upon induction (Supplementary Fig. 12). This suggested that the reduction of SDH activity in Huh7-*GCK*$^{+}$/*HK2*$^{-}$ cells was not strong enough to induce such a pseudo-hypoxic phenotype.

Our gene-centric metabolic analysis of transcriptomic data revealed a wide spreading of metabolic modifications resulting from HK isoenzyme switch. Illustrating these modifications, Fig. 7 is an attempt to integrate the observed changes in central carbon metabolism and closely connected metabolic pathways. In particular, decreased level of alanine and increased aspartate concentration in Huh7-*GCK*$^{+}$/*HK2*$^{-}$ cells could be an indirect effect of PC activation that uses pyruvate for the synthesis of OAA. As a consequence, hepatic transaminases may balance intracellular pools of OAA, aspartate, alanine and pyruvate. Glutamate and GABA levels were also modified, thus supporting anaplerosis of the TCA cycle through glutamine consumption and the GABA shunt pathway, respectively. We also observed lower levels of oxalate, an end-product of glyoxylate degradation. In Huh7-*GCK*$^{+}$/*HK2*$^{-}$ cells, increased levels of alanine-glyoxylate and serine-pyruvate aminotransferase (*AGXT*) could account for this phenotype as it converts alanine and glyoxylate into pyruvate and glycine, which is also increased. Interestingly, high level of *AGXT* is a good prognostic marker for HCC[35]. Consistently, it was found that oxalate inhibits liver PC, resulting in reduced gluconeogenesis and

lipogenesis[36-37]. Thus, a higher PC activity could be explained by lower levels of oxalate in Huh7-*GCK*$^{+}$/*HK2*$^{-}$ cells. We also observed that isoleucine and valine levels increased while branched chain amino acid transaminase 1 (*BCAT1*) predominant transcripts decreased. This suggests a reduced catabolism of branched chain amino acids in Huh7-*GCK*$^{+}$/*HK2*$^{-}$ cells. Again, low levels of *BCAT1* is a good prognostic marker for HCC and oral supplementation with branched chain amino acids has been shown to reduce the risk of liver cancer in cirrhotic patients[38-39]. If some metabolic modifications seem to advocate for the restoration of a normal hepatocyte phenotype following the replacement of HK2 by GCK, it cannot be a general statement. Indeed, the urea cycle was also impacted in Huh7-*GCK*$^{+}$/*HK2*$^{-}$ cells with lower levels of *CPS1* and *OTC*, which are also observed in aggressive HCC tumors[40]. Altogether, our results demonstrate the broad impact of replacing HK2 by GCK in HCC cells, and the key role played by the HK isoenzyme switch in HCC tumor metabolism.

Taken together, our data demonstrate that beyond glycolysis, the hexokinase isoenzyme switch in an HCC model rewires central carbon metabolism, promotes lipogenesis, enhances innate immune functions, and restores sensitivity to natural killer cells.

4.4 Methods

Unless otherwise specified, chemicals were from Merck Sigma-Aldrich. The RIG-I specific ligand 3p-hpRNA and the MDA5/TLR3 ligand poly(I:C) HMW (High Molecular Weight) were from Invivogen.

4.4.1 Cell cultures.

Cell cultures were tested negative for mycoplasma contamination by PCR (mycoplasma check, eurofins). Huh7 cells were authenticated by Eurofins Medigenomix Forensik GmbH using PCR-single-locus-technology. 21 independent PCR-systems Amelogenin, D3S1358, D1S1656, D6S1043, D13S317, Penta E, D16S539, D18S51, D2S1338, CSF1PO, Penta D, TH01, vWA, D21S11, D7S820, D5S818, TPOX, D8S1179, D12S391, D19S433 and FGA (Promega, PowerPlex 21 PCR Kit) were investigated to determine their genetic characteristics. Huh7 cells and derivatives were grown as previously described[41] in DMEM, 10% fetal calf serum (FCS), penicillin/streptomycin, 1 mM pyruvate, 2 mM L-glutamine. Culture medium and additives were from Gibco except FCS (Dominique Dutcher).

4.4.2 Cell lines.

Huh7 cells (15×10^{4}) were transduced for GCK expression at different multiplicities of infection (lentiviral transduction using the pLEX-GCK construct). The Huh7-*GCK*$^{+}$/*HK2*$^{+}$ cells were then cultured for 7 days with puromycin (1 µg/mL) before amplification. HK2 knock-out was achieved using the CRISPR/Cas9 system as previously described[42] to obtain Huh7-*GCK*$^{+}$/*HK2*$^{-}$ cells. Briefly, a single guide RNA (sgRNA) pair was designed for double nicking using the CRISPR Design Tool (http://tools.genome-engineering.org). The guide

sequence oligos (sgRNA$_1$(*HK2*): 5'-CACCGTGACCACATTGCCGAATGCC-3' and sgRNA$_2$(*HK2*): 5'-CACCGTTACCTCGTCTAGTTTAGTC-3') were cloned into a plasmid containing sequences for Cas9 expression and the sgRNA scaffold (pSpCas9(BB)-2A-GFP, Addgene plasmid #48138). 48 h post-transfection, cells were sorted by FACS based on the transient expression of GFP and cloned by limiting dilution. Effective deletion of HK2 was assessed by qPCR.

For *HK2* knock-down, Huh7-*GCK*$^+$/*HK2*$^+$ cells were transduced with lentiviral vectors expressing HK2-targeting shRNAs, and antibiotic selection was applied (hygromycin; 100 µg/ml). The *HK2*-targeting sequence 5'CCGGCCAGAAGACATTAGAGCATCTCTCGAGAGATGCTCTAATGTCTT CTGGTTTTTT-3' was cloned in the pLKO.1 hygro vector (a gift from Bob Weinberg; Addgene plasmid #24150). HK2 expression in Huh7-*GCK*$^+$/*HK2*$^+$ and Huh7-*GCK*$^+$/*HK2*$^-$Sh was analyzed on cell lysates by western blotting (Supplementary Fig. 10).

4.4.3 Enzymatic activity assays.

Cells were trypsinized, washed twice, and cell pellets were stored at −80 °C. Protein extractions and assays were performed in specific buffers for hexokinase and pyruvate carboxylase assays as described below.

4.4.4 Hexokinase activity assay.

The method used for monitoring HK activity in cells lysates was adapted from Kuang et al.[43-45] Cellular pellets stored at −80 °C were thawed and immediately homogenized (2×10^6 cells/100 µl) in precooled reaction buffer. (0.05 M Tris–HCl, 0.25 M sucrose, 0.005 M EDTA, 0.005 M 2-mercaptoethanol, pH = 7.4). After 20 min incubation on ice, homogenates were pulsesonicated 15 s at half power (EpiShear Probe Sonicator). Homogenates were then centrifuged at 500 g for 20 min at 4 °C. Supernatants were immediately used for determination of HK activity, which was measured spectrophotometrically through $NADP^+$ reduction in the glucose 6-phosphate dehydrogenase-coupled reaction. HK activity was assayed in medium containing 50 mM triethanolamine (pH = 7.6), 10 mM $MgCl_2$, 1.4 mM $NADP^+$, with variable concentration of glucose and 1 U glucose 6-phosphate dehydrogenase (*S. cerevisiae*), equilibrated to 37 °C. The reaction was started by addition of ATP (final concentration 1.9 mM), and absorbance was continuously recorded for 30 min at 340 nm (TECAN Infinite M200).

4.4.5 Pyruvate carboxylase activity assay.

The method used for quantification of PC activity was adapted from Payne et al.[46] Briefly, cells were centrifuged, washed twice with ice-cold PBS before homogenization in Tris-HCL 100 mM, pH = 8.0 using a Dounce homogenizer. Homogenates were pulse-sonicated 15 s at half power (EpiShear Probe Sonicator) before centrifugation at 500 g for 5 min. Supernatants were immediately used for the assay. PC activity was assayed in medium containing 100 mM Tris-HCl, 50 mM NaHCO3, 5 mM $MgCl_2$, 0.1 mM Acetyl-CoA, 0.25 mM 6,6'-Dinitro-3,3'-dithiodibenzoic acid (DTNB), 5 mM ATP, 5 mM pyruvate, citrate synthase and cofactors. Reduction of DTNB by the generated free CoA was

measured continuously by Abs at 412 nm and recorded for 30 min (TECAN Infinite M200). The same assay was performed in absence of pyruvate to subtract background signal.

4.4.6 Metabolomics profiling.

Cells were seeded at 13×10^5 cells per 75 cm^2 dishes. After 24 h, supernatant was removed and replaced by fresh culture medium. For quantification of metabolic flux from glucose, culture medium was supplemented with both [U-^{13}C]-glucose (Sigma-Aldrich; 389374-2 G) and unlabeled glucose at a 50:50 ratio (final concentration of 25 mM glucose). After 24 h, cells were harvested, washed twice with ice-cold PBS and cell pellets were frozen at -80 °C until metabolites extraction. Cell pellets were transferred into a pre-chilled microcentrifuge tube with 1 mL cold extraction buffer consisting of 50% methanol (A452, Fisher Scientific) in ultrapure water. Samples were then frozen in liquid nitrogen, thawed, and placed in a shaking dry bath (Thermo Fisher Scientific, Waltham, MA) set to 1100 rpm for 15 min at 4 °C. After centrifugation for 15 min at 12500 g and 4 °C (Sorvall, Thermo Fisher Scientific) using a fixed-angle F21-48×1.5 rotor, supernatants were collected and dried by vacuum centrifugation overnight. Dried metabolites were derivatized by addition of 20 µL of 2.0% methoxyaminehydrochloride in pyridine (MOX, TS-45950, Thermo Fisher Scientific) followed by incubation during 90 min in shaking dry bath at 30 °C and 1100 rpm. Ninety µL of N-methyl-N-trimethylsilyltrifluoroacetamide (MSTFA, 701270.201, MachereyNagel) was added, and samples were incubated and shaken at 37 °C for 30 min before centrifugation for 5 min at 14,000 rpm and 4 °C. Metabolites contained in the supernatant were then separated by gas chromatography (GC, TRACE 1310, Thermo Fisher Scientific) coupled to a triple-quadrupole mass spectrometry system for analysis (QQQ GCMS, TSQ8000EI, TSQ8140403, Thermo Fisher Scientific), equipped with a 0.25 mm inner diameter, 0.25 µm film thickness, 30 m length 5% diphenyl / 95% dimethyl polysiloxane capillary column (OPTIMA 5 MS Accent, 725820.30, Macherey-Nagel) and run under electron ionization at 70 eV. Using established separation methods[47-49], the GC was programed with an injection temperature of 250.0 °C and splitless injection volume of 1.0 µL. The GC oven temperature program started at 50 °C (323.15 K) for 1 min, rising at 10 K/min to 300.0 °C (573.15 K) with a final hold at this temperature for 6 min. The GC flow rate with helium carrier gas (HE, HE 5.0UHP, Praxair) was 1.2 mL/min. The transfer line temperature was set at 290.0 °C and ion source temperature at 295.0 °C. A range of 50-600 m/z was scanned with a scan time of 0.25 s.

4.4.7 Metabolomics data processing.

Metabolites were identified using TraceFinder (v3.3, Thermo Fisher Scientific) based on libraries of metabolite retention times and fragmentation patterns (Metaflux, Merced, CA). Identified metabolites were quantified using the selected ion count peak area for specific mass ions, and standard curves generated from reference standards run in parallel. Peak intensities were median normalized. The mean and standard deviation for each quantified metabolite was calculated for each cell line and treatment condition. A

univariate *t*-test was used to compare treatment conditions for each metabolite and cell line.

4.4.8 Intracellular lipid staining.

For fluorescence microscopy staining of intracellular lipids, cells were seeded and cultured during 48 h before staining with Oil-Red-O. Cells were fixed 15 min at RT with a 4% formaldehyde solution, washed twice with water before a 5 min incubation with isopropanol 60%. Isopropanol was then removed and Oil-Red-O solution (Millipore Sigma-Aldrich) added on cells for 15 min at RT. Cells were then extensively washed with water to remove the exceeding dye before nucleus counterstaining with NucBlue Fixed Cell Stain ReadyProbes reagent (ThermoFisher Scientific) and observation with a Nikon Eclipse Ts2R microscope (x60). For the quantification of intracellular lipid droplets by flow-cytometry, cells were stained with the BODIPY® 493/503 dye (Tocris BioTechne) after 48 h of culture. The cells were washed with PBS before being incubated for 5 min with a 5 µM BODIPY solution in PBS at 37 °C. Cells were then washed with PBS before trypsination and FACS analysis. A 7-AAD (BioLegend) staining of dead cells, prior to FACS analysis, allowed gating on living cells.

4.4.9 Protein, ApoB, and lipid quantification.

Protein concentration was determined using the DC Protein Assay (Bio-Rad). ApoB concentration in medium and gradients fractions was determined by ELISA as previously described[50]. Total concentrations of cholesterol, phospholipids, and triglycerides (TG) were determined using specific assays from Millipore Sigma-Aldrich (ref. MAK043, MAK122 and MAK266 respectively). Free Fatty Acids were quantified using a specific assay kit from Abcam (ref. ab65341).

4.4.10 Iodixanol density gradients.

Iodixanol gradients were prepared as previously described[51]. One mL of culture supernatant was applied to the top of 6 to 56% iodixanol gradients and centrifuged for 10 h at 41,000 rpm and 4 °C in a SW41 rotor. The gradient was harvested by tube puncture from the bottom and collected into 22 fractions (0.5 mL each). The density of each fraction was determined by weighing.

4.4.11 Metabolic network coherence computational analysis.

In order to measure the consistency of differentially expressed genes with a metabolic network, we employed the metabolic network coherence measure introduced by Sonnenschein et al.[52] This approach was previously applied to various disease-related transcriptome profiles[53-54] and for extracting information on the genetic control of metabolic organization[55]. Recently, detailed theoretical analysis of the extended version of the method has been performed by Nyczka and Hütt[56]. Here, we first extracted a gene-centric metabolic network from a given genome-scale metabolic model. This was achieved via the stoichiometric matrix and the gene-reaction associations contained in the metabolic model. We constructed the two projections of the bipartite graph represented by the stoichiometric matrix, yielding a metabolite-

centric and a reaction-centric graph. The metabolite-centric graph allowed us to identify high-degree nodes ('currency metabolites' like H_2O, ATP, etc.), which are not informative about the network-like organization of the metabolic systems and need to be eliminated before interpreting the network architecture (see references[53,57] for details). The degree of a node is the number of neighbors the node has in the network. The percentage of remaining metabolites is one of the parameters of our analysis. Typical values are 90 to 98 percent (i.e., a removal of the highest 2 to 10% of metabolites with the highest degree as currency metabolites). After recomputing the reaction-centric graph based on the reduced number of metabolites (Supplementary Fig. 3), we can now evaluate the gene-reaction associations to arrive at a gene-centric metabolic network (Supplementary Fig. 3). Given a set S of differentially expressed genes and the gene-centric metabolic network G, we can now analyze the subgraph of G spanned by all genes in S. The average clustering coefficient C in these subgraphs serves as a measure of the connectivity of this subgraph. The metabolic network coherence MC is the z-score of C computed with respect to a null model of randomly drawn gene sets with the same size as S (Supplementary Fig. 4). In this way, MC has an intuitive interpretation: The value of MC indicates, how many standard deviations away from randomness the clustering of the subgraph spanned by the observed gene set S actually is (Supplementary Fig. 4 and reference[58]). The genome-scale metabolic models employed here are the generic human metabolic model Recon 2[59]. In general, different network measures can be used for evaluation of MC. In the scope of this study, we have tested several of them, but opted for average clustering coefficient C, as it yielded strongest statistical signal.

4.4.12 Western blot analysis.

Cell lysates from 10^6 cells were prepared in lysis buffer (1% Triton X-100, 5 mM EDTA in PBS with 1% protease inhibitor cocktail (P8340; Millipore Sigma-Aldrich) and 2 mM orthovanadate). After elimination of insoluble material, proteins were quantified, separated by SDS-PAGE and analyzed by western-blot on PVDF membrane. After saturation of the PVDF membrane in PBS-0.1% Tween 20 supplemented with 5% (w/v) non-fat milk powder, blots were incubated 1 h at room temperature with primary antibody in PBS-0.1% Tween 20 (1:2,000 dilution for all antibodies unless specified otherwise). Incubation with secondary antibody was performed after washing for 1 h at room temperature. HRP-labeled anti-goat (Santa Cruz Biotechnology), anti-rabbit (A0545, Millipore Sigma-Aldrich) or anti-mouse (Jackson ImmunoResearch Laboratories) antibodies were diluted 20,000-fold and detected by enhanced chemiluminescence reagents according to the manufacturer's instructions (SuperSignal Chemiluminescent Substrate, Thermo Fisher Scientific). Primary antibodies used for immunoblotting included mouse monoclonal antibody against human GCK (clone G-6, Santa Cruz Biotechnology), rabbit monoclonal antibody against human HK2 (Clone C64G5, Cell Signaling Technology), rabbit monoclonal antibody against human HK1 (C35C4, Cell Signaling), rabbit polyclonal antibody against human HK3 (HPA056743, Millipore Sigma-Aldrich), goat polyclonal antibody against human ACLY (SAB2500845, Millipore Sigma-Aldrich), rabbit polyclonal antibody against human pACLY (phospho S455, Cell Signaling Technology), rabbit monoclonal antibody against human PDH α1

subunit (C54G1, Cell Signaling Technology), rabbit monoclonal antibody against human pPDH E1-alpha subunit (phospho S293, Abcam), goat polyclonal antibody against human PC (SAB2500845, Millipore Sigma-Aldrich), rabbit monoclonal antibody against human GAPDH (D16H11, Cell Signaling Technology) and rabbit polyclonal antibody against human HIF-1α (NB100-134, Novus Biologicals; 1:500 dilution).

4.4.13 Statistics and reproducibility.

All the statistical analyses were performed with GraphPad Prism or Analyse-it software. Details of statistical analyses can be found in figure legends. Two-sided statistical analyses were performed on experiments reproduced at least 3 times independently. The exact p values are indicated either directly in the figure or in the legend. The exact sample size (n) is given in the legend of each figure. The mean ± standard error of the mean (SEM) is displayed, unless otherwise stated. Confidence interval was set to 95% in all statistical tests.

4.4.14 Reporting summary.

Further information on research design is available in the Nature Research Reporting Summary linked to this article.

4.5 Data availability

The data generated or analyzed during this study are included in the article and supplementary files. The transcriptomes of the 365 HCC biopsies analyzed in the current study were obtained from The Cancer Genome Atlas (TCGA) database and are available in Supplementary Data 1. The RNA-seq data for Huh7 and Huh7-*GCK*$^{+}$/*HK*2^{-} cell lines are available in Supplementary Data 2 and at the Gene Expression Omnibus database with the accession number GSE144214 for entire raw data. Source data and calculations for all experiments can be found in Supplementary Data 4. Uncropped images of western are provided in Supplementary Figs. 1 and 7.

Received: 2 May 2020; Accepted: 11 December 2020; Published online: 16 February 2021.

4.6 Acknowledgements

We acknowledge the contribution of the Genomics and Microgenomics platform ProfileXpert (University Lyon 1, SFR santé LYON-EST, UCBL-Inserm US 7-CNRS UMS3453) and SFR Biosciences (UMS3444/CNRS, US8/Inserm, ENS de Lyon, UCBL) facilities: AniRA-Cytometry, AniRA-ImmOs metabolic phenotyping and LYMICPLATIM microscopy. We gratefully thank Laurence Canaple for technical assistance. This work was supported by the Fondation pour la Recherche Médicale (FRM), grant number DEQ20160334893 to VL. F.V.F. is grateful for the support by grants CA154887, GM115293, CRN-17-427258, NSF GRFP, and the Science Alliance on Precision Medicine and Cancer Prevention by the German Federal Foreign Office, implemented by the

Goethe-Institute, Washington, DC, USA, and supported by the Federation of German Industries (BDI), Berlin, Germany.

4.6.1 Author contributions

L.P-C., P-O.V., O.D. and V.L. designed the experiments with critical advices from G.J.P.R., P.A., R.R. and F.V.F.; C.J., A.A-G., K.O., B.P., G.J.P.R., N.A, R.R. and F.V.F. performed experiments and analyzed the data; P.N. and M-T.H. performed metabolic network computational analysis; L.P-C., P-O.V., P.A., F.V.F, V.L. and O.D. analyzed the data, prepared figures and wrote the manuscript.

4.6.2 Competing interests

The authors declare no competing interests.

4.6.3 Additional information

Supplementary information: The online version contains supplementary material available at https://doi.org/10.1038/s42003-021-01749-3.

Correspondence and requests for materials should be addressed to V.L. or O.D.

Reprints and permission information is available at http://www.nature.com/reprints

Publisher's note: Springer Nature remains neutral with regard to jurisdictional claims in published maps and institutional affiliations.

4.7 References

1. Villanueva A. Hepatocellular carcinoma. *N Engl J Med*. 2019;380(15):1450-1462. PMID: 30970190.

2. Kudo M, Finn RS, Qin S, et al. Lenvatinib versus sorafenib in first-line treatment of patients with unresectable hepatocellular carcinoma: a randomised phase 3 non-inferiority trial. *Lancet*. 2018;391(10126):1163-1173. PMID: 29433850.

3. Llovet JM, Montal R, Sia D, Finn RS. Molecular therapies and precision medicine for hepatocellular carcinoma. *Nat Rev Clin Oncol*. 2018;15(10):599-616. PMID: 30061739.

4. De Matteis S, Ragusa A, Marisi G, et al. Aberrant metabolism in hepatocellular carcinoma provides diagnostic and therapeutic opportunities. *Oxid Med Cell Longev*. 2018;2018:7512159. PMID: 30524660.

5. Filipp FV, Ratnikov B, De Ingeniis J, Smith JW, Osterman AL, Scott DA. Glutamine-fueled mitochondrial metabolism is decoupled from glycolysis in melanoma. *Pigment Cell Melanoma Res*. 2012;25(6):732-9. PMID: 22846158.

6. Hay N. Reprogramming glucose metabolism in cancer: can it be exploited for cancer therapy? *Nat Rev Cancer*. 2016;16(10):635-49. PMID: 27634447.

7. Vander Heiden MG, Cantley LC, Thompson CB. Understanding the Warburg effect: the metabolic requirements of cell proliferation. *Science*. 2009;324(5930):1029-33. PMID: 19460998.

8. Jiang J, Nilsson-Ehle P, Xu N. Influence of liver cancer on lipid and lipoprotein metabolism. *Lipids Health Dis*. 2006;5:4. PMID: 16515689.

9. DeWaal D, Nogueira V, Terry AR, et al. Hexokinase-2 depletion inhibits glycolysis and induces oxidative phosphorylation in hepatocellular carcinoma and sensitizes to metformin. *Nat Commun*. 2018;9(1):446. PMID: 29386513.

10. Guo C, Ludvik AE, Arlotto ME, et al. Coordinated regulatory variation associated with gestational hyperglycaemia regulates expression of the novel hexokinase HKDC1. *Nat Commun*. 2015;6:6069. PMID: 25648650.

11. Guzman G, Chennuri R, Chan A, et al. Evidence for heightened hexokinase II immunoexpression in hepatocyte dysplasia and hepatocellular carcinoma. *Dig Dis Sci*. 2015;60(2):420-6. PMID: 25381201.

12. Wolf AJ, Reyes CN, Liang W, et al. Hexokinase is an innate immune receptor for the detection of bacterial peptidoglycan. *Cell*. 2016;166(3):624-636. PMID: 27374331.

13. Tan VP, Miyamoto S. HK2/hexokinase-II integrates glycolysis and autophagy to confer cellular protection. *Autophagy*. 2015;11(6):963-4. PMID: 26075878.

14. Roberts DJ, Tan-Sah VP, Ding EY, Smith JM, Miyamoto S. Hexokinase-II positively regulates glucose starvation-induced autophagy through TORC1 inhibition. *Mol Cell*. 2014;53(4):521-33. PMID: 24462113.

15. Kishore M, Cheung KCP, Fu H, et al. Regulatory T cell migration is dependent on glucokinase-mediated glycolysis. *Immunity*. 2017;47(5):875-889.e10. PMID: 29166588.

16. Lee NCW, Carella MA, Papa S, Bubici C. High expression of glycolytic genes in cirrhosis correlates with the risk of developing liver cancer. *Front Cell Dev Biol*. 2018;6:138. PMID: 30430110.

17. Uhlén M, Fagerberg L, Hallström BM, et al. Proteomics. Tissue-based map of the human proteome. *Science*. 2015;347(6220):1260419. PMID: 25613900.

18. Uhlén M, Zhang C, Lee S, et al. A pathology atlas of the human cancer transcriptome. *Science*. 2017;357(6352):eaan2507. PMID: 28818916.

19. Yoo J-J, Yu SJ, Na J, et al. Hexokinase-II inhibition synergistically augments the anti-tumor efficacy of sorafenib in hepatocellular carcinoma. *Int J Mol Sci*. 2019;20(6):1292. PMID: 30875800.

20. Porter CM, Miller BG. Cooperativity in monomeric enzymes with single ligand-binding sites. *Bioorg Chem*. 2012;43:44-50. PMID: 22137502.

21. Larion M, Salinas RK, Bruschweiler-Li L, Miller BG, Brüschweiler R. Order-disorder transitions govern kinetic cooperativity and allostery of monomeric human glucokinase. *PLoS Biol*. 2012;10(12):e1001452. PMID: 23271955.

22. van den Berghe G. The role of the liver in metabolic homeostasis: Implications for inborn errors of metabolism. *J Inherit Metab Dis*. 1991;14(4):407-20. PMID: 1749209.

23. Berg JM, Tymoczko JL, Stryer L. Biochemistry 5th edition. Ch. 30.2. W H Freeman; 2002.

24. Beilstein F, Lemasson M, Pène V, Rainteau D, Demignot S, Rosenberg AR. Lysophosphatidylcholine acyltransferase 1 is downregulated by hepatitis C virus: impact on production of lipo-viro-particles. *Gut*. 2017;66(12):2160-2169. PMID: 27582510.

25. Ginsberg HN. Lipoprotein physiology. *Endocrinol Metab Clin North Am*. 1998;27(3):503-19. PMID: 9785050.

26. Meex SJR, Andreo U, Sparks JD, Fisher EA. Huh-7 or HepG2 cells: which is the better model for studying human apolipoprotein-B100 assembly and secretion? *J Lipid Res*. 2011;52(1):152-8. PMID: 20956548.

27. Lussey-Lepoutre C, Hollinshead KER, Ludwig C, et al. Loss of succinate dehydrogenase activity results in dependency on pyruvate carboxylation for cellular anabolism. *Nat Commun*. 2015;6:8784. PMID: 26522426.

28. Lampropoulou V, Sergushichev A, Bambouskova M, et al. Itaconate links inhibition of succinate dehydrogenase with macrophage metabolic remodeling and regulation of inflammation. *Cell Metab*. 2016;24(1):158-66. PMID: 27374498.

29. Panasyuk G, Espeillac C, Chauvin C, et al. PPARγ contributes to PKM2 and HK2 expression in fatty liver. *Nat Commun*. 2012;3:672. PMID: 22334075.

30. Mesarwi OA, Shin M-K, Bevans-Fonti S, Schlesinger C, Shaw J, Polotsky VY. Hepatocyte hypoxia inducible factor-1 mediates the development of liver fibrosis in a mouse model of nonalcoholic fatty liver disease. *PLoS One*. 2016;11(12):e0168572. PMID: 28030556.

31. Roberts DJ, Miyamoto S. Hexokinase II integrates energy metabolism and cellular protection: Akting on mitochondria and TORCing to autophagy. *Cell Death Differ*. 2015;22(2):248-57. PMID: 25323588.

32. Van den Bossche J, O'Neill LA, Menon D. Macrophage immunometabolism: where are we (going)? *Trends Immunol*. 2017;38(6):395-406. PMID: 28396078.

33. Tannahill GM, Curtis AM, Adamik J, et al. Succinate is an inflammatory signal that induces IL-1β through HIF-1α. *Nature*. 2013;496(7444):238-42. PMID: 23535595.

34. Kluckova K, Tennant DA. Metabolic implications of hypoxia and pseudohypoxia in pheochromocytoma and paraganglioma. *Cell Tissue Res*. 2018;372(2):367-378. PMID: 29450727.

35. Sun Y, Li W, Shen S, et al. Loss of alanine-glyoxylate and serine-pyruvate aminotransferase expression accelerated the progression of hepatocellular carcinoma and predicted poor prognosis. *J Transl Med*. 2019;17(1):390. PMID: 31771612.

36. Yount EA, Harris RA. Studies on the inhibition of gluconeogenesis by oxalate. *Biochim Biophys Acta*. 1980;633(1):122-33. PMID: 6778509.

37. O'Neill IE, Bannister DW. The effects of oxalate and glucose on lipogenesis by isolated hepatocytes from normal and biotin-deficient chicks (*Gallus domesticus*). *Int J Biochem*. 1984;16(5):517-21. PMID: 6724106.

38. Muto Y, Sato S, Watanabe A, et al. Overweight and obesity increase the risk for liver cancer in patients with liver cirrhosis and long-term oral supplementation with branched-chain amino acid granules inhibits liver carcinogenesis in heavier patients with liver cirrhosis. *Hepatol Res*. 2006;35(3):204-14. PMID: 16737844.

39. Kawaguchi T, Shiraishi K, Ito T, et al. Branched-chain amino acids prevent hepatocarcinogenesis and prolong survival of patients with cirrhosis. *Clin Gastroenterol Hepatol*. 2014;12(6):1012-8.e1. PMID: 24036055.

40. Ally A, Balasundaram M, Carlsen R, et al. Comprehensive and integrative genomic characterization of hepatocellular carcinoma. *Cell*. 2017;169(7):1327-1341.e23. PMID: 28622513.

41. Scholtes C, Diaz O, Icard V, et al. Enhancement of genotype 1 hepatitis C virus replication by bile acids through FXR. *J Hepatol*. 2008;48(2):192-9. PMID: 18096266.

42. Ran FA, Hsu PD, Wright J, Agarwala V, Scott DA, Zhang F. Genome editing using the CRISPR-Cas9 system. *Nat Protoc*. 2013;8(11):2281-2308. PMID: 24157548.

43. Kuang Y, Schomisch SJ, Chandramouli V, Lee Z. Hexokinase and glucose-6-phosphatase activity in woodchuck model of hepatitis virus-induced hepatocellular carcinoma. *Comp Biochem Physiol C Toxicol Pharmacol*. 2006;143(2):225-31. PMID: 16581304.

44. Ramière C, Rodriguez J, Enache LS, Lotteau V, André P, Diaz O. Activity of hexokinase is increased by its interaction with hepatitis C virus protein NS5A. *J Virol*. 2014;88(6):3246-3254. PMID: 24390321.

45. Perrin-Cocon L, Aublin-Gex A, Diaz O, et al. Toll-like receptor 4-induced glycolytic burst in human monocyte-derived dendritic cells results from p38-dependent stabilization of HIF-1α and increased hexokinase II expression. *J Immunol*. 2018;201(5):1510-1521. PMID: 30037846.

46. Payne J, Morris JG. Pyruvate carboxylase in *Rhodopseudomonas spheroides*. *J Gen Microbiol*. 1969;59(1):97-101. PMID: 5365367.

47. Lanning NJ, Castle JP, Singh SJ, et al. Metabolic profiling of triple-negative breast cancer cells reveals metabolic vulnerabilities. *Cancer Metab*. 2017;5:6. PMID: 28852500.

48. Shah R, Singh SJ, Eddy K, Filipp FV, Chen S. Concurrent targeting of glutaminolysis and metabotropic glutamate receptor 1 (GRM1) reduces glutamate bioavailability in GRM1$^+$ melanoma. *Cancer Res*. 2019;79(8):1799-1809. PMID: 30987979.

49. Filipp FV, Scott DA, Ronai ZA, Osterman AL, Smith JW. Reverse TCA cycle flux through isocitrate dehydrogenases 1 and 2 is required for lipogenesis in hypoxic melanoma cells. *Pigment Cell Melanoma Res*. 2012;25(3):375-83. PMID: 22360810.

50. Scholtes C, Ramière C, Rainteau D, et al. High plasma level of nucleocapsid-free envelope glycoprotein-positive lipoproteins in hepatitis C patients. *Hepatology*. 2012;56(1):39-48. PMID: 22290760.

51. Icard V, Diaz O, Scholtes C, et al. Secretion of hepatitis C virus envelope glycoproteins depends on assembly of apolipoprotein B positive lipoproteins. *PLoS One*. 2009;4(1):e4233. PMID: 19156195.

52. Sonnenschein N, Geertz M, Muskhelishvili G, Hütt M. Analog regulation of metabolic demand. *BMC Syst Biol*. 2011;5:40. PMID: 21406074.

53. Sonnenschein N, Dzib JFG, Lesne A, et al. A network perspective on metabolic inconsistency. *BMC Syst Biol*. 2012;6:41. PMID: 22583819.

54. Knecht C, Fretter C, Rosenstiel P, Krawczak M, Hütt M-T. Distinct metabolic network states manifest in the gene expression profiles of pediatric inflammatory bowel disease patients and controls. *Sci Rep*. 2016;6:32584. PMID: 27585741.

55. Schlicht K, Nyczka P, Caliebe A, et al. The metabolic network coherence of human transcriptomes is associated with genetic variation at the cadherin 18 locus. *Hum Genet*. 2019;138(4):375-388. PMID: 30852652.

56. Nyczka P, Hütt M-T. Generative network model of transcriptome patterns in disease cohorts with tunable signal strength. *Phys Rev Res*. 2020;2(3):033130.

57. Ma H, Zeng A-P. Reconstruction of metabolic networks from genome data and analysis of their global structure for various organisms. *Bioinformatics*. 2003;19(2):270-7. PMID: 12538249.

58. Hütt M-T. Understanding genetic variation – the value of systems biology. *Br J Clin Pharmacol*. 2014;77(4):597-605. PMID: 24725073.

59. Thiele I, Swainston N, Fleming RMT, et al. A community-driven global reconstruction of human metabolism. *Nat Biotechnol*. 2013;31(5):419-25. PMID: 23455439.

60. Gao J, Aksoy BA, Dogrusoz U, et al. Integrative analysis of complex cancer genomics and clinical profiles using the cBioPortal. *Sci Signal*. 2013;6(269):pl1. PMID: 23550210.

61. Cerami E, Gao J, Dogrusoz U, et al. The cBio cancer genomics portal: an open platform for exploring multidimensional cancer genomics data. *Cancer Discov*. 2012;2(5):401-4. PMID: 22588877.

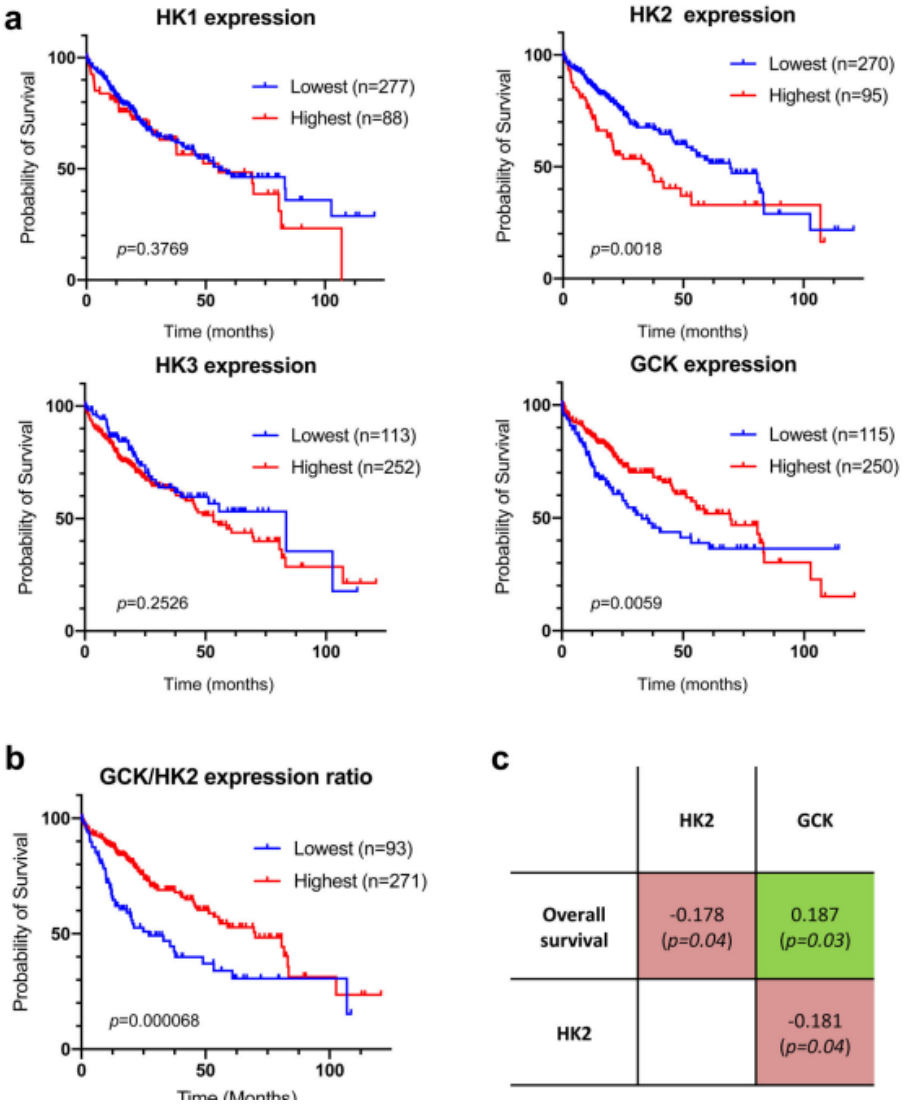

Figure 4.1. Correlation between hexokinase expression levels in HCC tumors and patient survival.

a) Kaplan-Meier estimates of the survival of HCC patients depending on the expression of *HK1*, *HK2*, *HK3* and *GCK* (*HK4*) genes in tumor biopsies (n = 365; diploid samples; TCGA expression data retrieved from cBioPortal; Firehose Legacy)[60-61]. Duplicate analyses from the same patient were removed as well as patients who died when biopsied (overall survival=0 months or not specified). Optimal stratification based on highest and lowest gene expression values was determined using Protein Atlas database[18].

b) Same as above but patients were stratified based on the *GCK*/*HK2* gene expression ratio. The stratification showing the lowest p value when comparing subgroups of patients with the highest to the lowest *GCK*/*HK2* expression ratio is displayed. Patient TCGA-DD-AAE9 exhibiting undetectable levels of *GCK* and *HK2* was removed from this analysis as the *GCK*/*HK2* ratio could not be calculated.

c) Correlations between patient survival, *GCK* expression and *HK2* expression. Spearman's rank correlation test on the subset 130 patients for whom the period between diagnosis and death is precisely known (uncensored data).

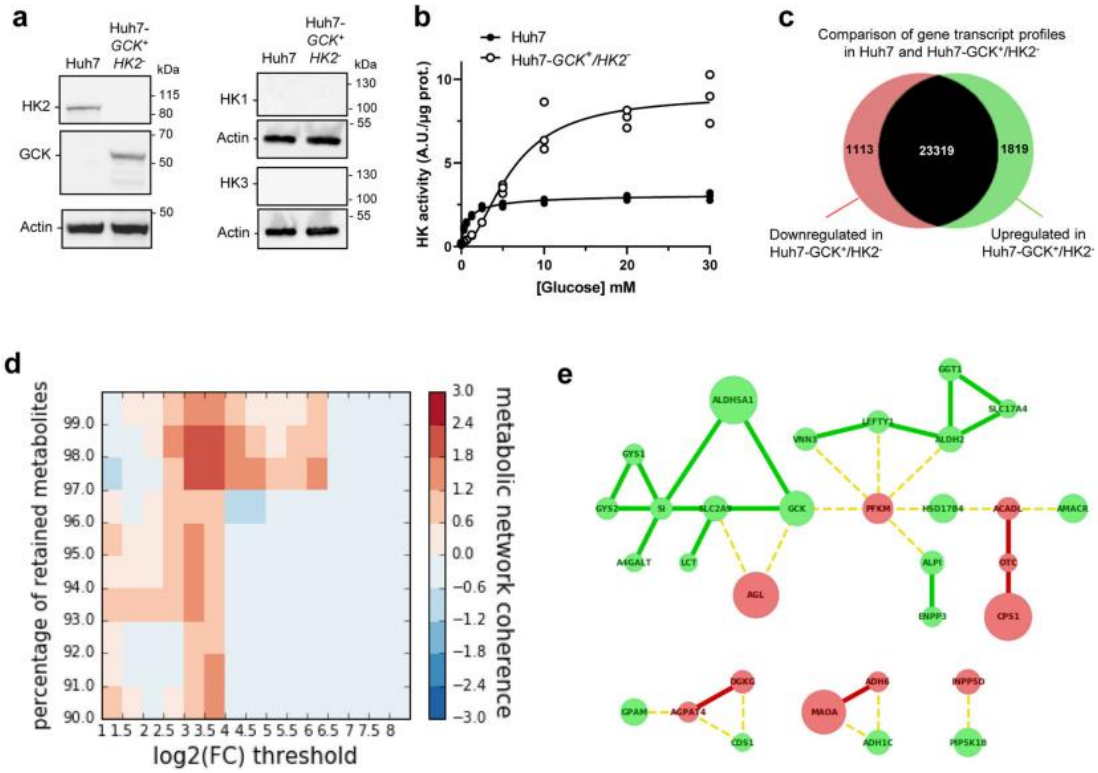

Figure 4.2. Hexokinase isoenzyme switch in Huh7 cells induces extended modifications of metabolic connections.

a) Western blot analysis of HK1, HK2, HK3 and GCK expression in Huh7 and Huh7-*GCK*$^{+}$/*HK2*$^{-}$.

b) Hexokinase activity in homogenates of Huh7 and Huh7-*GCK*$^{+}$/*HK2*$^{-}$ cells. Means ± SEM are presented (*n* = 3).

c) Number of genes changing their expression pattern in Huh7 and Huh7-*GCK*$^{+}$/*HK2*$^{-}$ cells (see Supplementary Data 2 for details).

d) Heatmap showing clustering enrichment scores of the networks obtained when mapping differentially expressed genes to the human metabolic model Recon2. Clustering enrichment scores from the highest in red to the lowest in blue were calculated for different gene expression thresholds (Log_2 | FC |) and percentages of retained currency metabolites.

e) Gene network corresponding to the maximal clustering enrichment score (Log_2 | FC | > 3; removed currency metabolites = 2%). The transcription of nodes in green was upregulated and those in red downregulated in Huh7-*GCK*$^{+}$/*HK2*$^{-}$ compared to Huh7 cells. Plain edges mark co-regulation between nodes and broken edges inverse regulation at the transcriptional level.

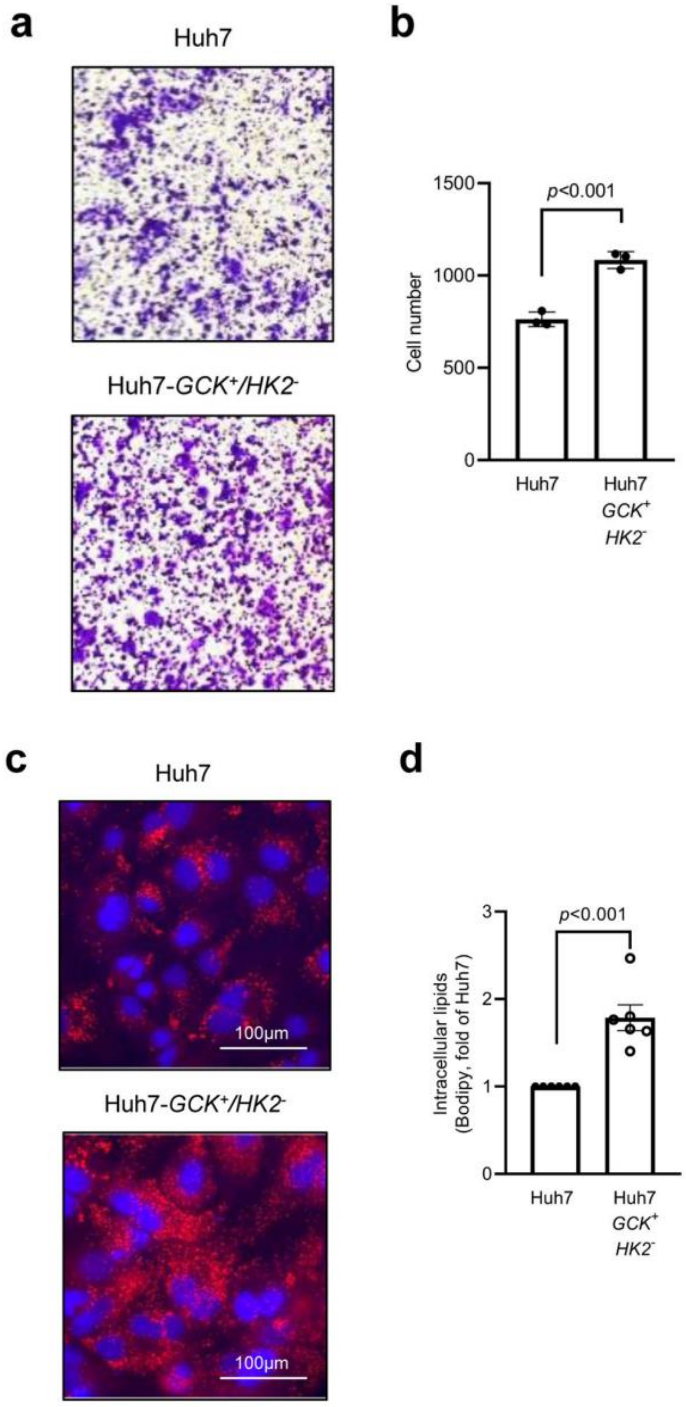

Figure 4.3. Huh7-*GCK*$^{+}$/*HK2*$^{-}$ cells have a higher migration capacity and lipid droplets content.

a), b) Results of transwell migration tests. **a** Representative images and **b** count of migrating cells (n = 3).

c) Oil Red-O staining of lipid droplets (red) with nucleus counterstaining (blue).

d) Quantification of intracellular lipids by FACS after BODIPY staining (n = 6). Means ± SEM are indicated and p values were determined by Student's t-test.

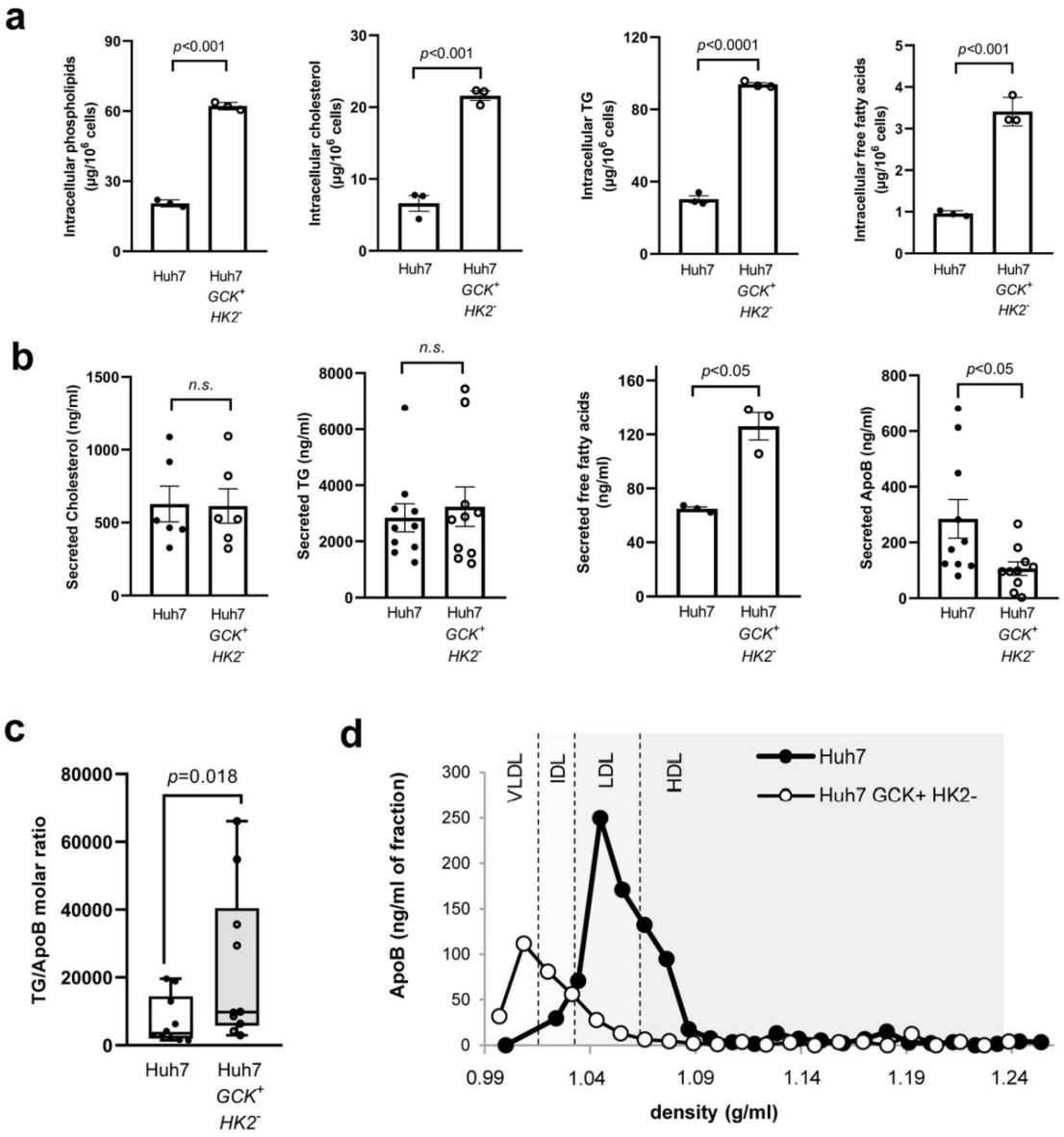

Figure 4.4. Lipogenesis and very-low-density lipoproteins (VLDL) secretion are restored in Huh7-*GCK*$^{+}$/*HK2*$^{-}$ cells.

a) Quantification of intracellular lipids in total cell extracts of Huh7 and Huh7-*GCK*$^{+}$/*HK2*$^{-}$ cells (*n* = 3).

b) Lipids and ApoB secretions in supernatants of cells cultured 24 h without FCS (*n* = 6 for Cholesterol, *n* = 3 for FFA and *n* = 10 for TG and ApoB).

c) TG/ApoB molar ratio calculated from quantifications determined in **b** (*n* =10).

d) Supernatants of Huh7 and Huh7-*GCK*$^{+}$/*HK2*$^{-}$ were analyzed by ultracentrifugation on iodixanol density gradients. ApoB was quantified in each fraction by ELISA (one representative experiment). Presented data correspond to means ± SEM of indicated number of independent experiments and *p* values were determined by Student's *t*-test.

Figure 4.5. TCA rewiring after hexokinase isoenzyme switch in Huh7 cells.

a) Glycogen quantification.

b) Creatinine and creatinine-P quantification.

c) This bubble chart compares intracellular metabolomes of Huh7 and Huh7-*GCK*$^{+}$/*HK2*$^{-}$ cells. Metabolite pool sizes larger in Huh7 are indicated in blue, whereas the one larger in Huh7-*GCK*$^{+}$/*HK2*$^{-}$ are shown in red. The size of bubbles inversely scales with p values between 5.10^{-2} and 1.10^{-17} of differential metabolomics responses.

d) Metabolic fluxes for overall glucose consumption and lactate secretion by Huh7 and Huh7-*GCK*$^{+}$/*HK2*$^{-}$ cells. Indicated values correspond to differences in glucose or lactate concentrations in extracellular culture medium before and after 24 h of culture.

e) Mass isotopomer distribution vector of pyruvate in cells cultured with [U-^{13}C]-glucose. Presented data correspond to n = 24 (**c**, **d**) or n = 16 (**e**) acquired spectra from N = 6 and N = 4 independent specimens, respectively.

f) Pyruvate carboxylase (PC) activity determined in cell homogenates.

g) Western blot analysis of PC expression in Huh7 and Huh7-*GCK*$^{+}$/*HK2*$^{-}$ cells.

h) Western blot analysis of pyruvate dehydrogenase (PDH) E1-alpha subunit phosphorylation at Ser293.

i) RNA-seq quantification of pyruvate dehydrogenase kinase 2 (PDK2) and pyruvate dehydrogenase phosphatase 2 (PDP2) (BH adjusted p value<0.05 from transcriptomic data).

j) Western blot analysis of ATP-citrate Lyase (ACLY) phosphorylation at Ser455.

k) Succinate quantification in cell homogenates.

l) Succinate dehydrogenase (SDH) activity determined in cell homogenates.

m) Oxygen consumption rate (OCR) in Huh7 and Huh7-*GCK*$^{+}$/*HK2*$^{-}$ cells was determined with a Seahorse analyzer before and after the addition of oligomycin (Complex V inhibitor), FCCP (uncoupling agent), rotenone (Complex I inhibitor) and antimycin A (Complex III inhibitor) (n = 5).

n) Non-mitochondrial, complex I-dependent and complex III-dependent maximal OCR were calculated from **m**. Except otherwise indicated, data correspond to means ± SEM of 3 independent experiments and p values were determined by Student's t-test.

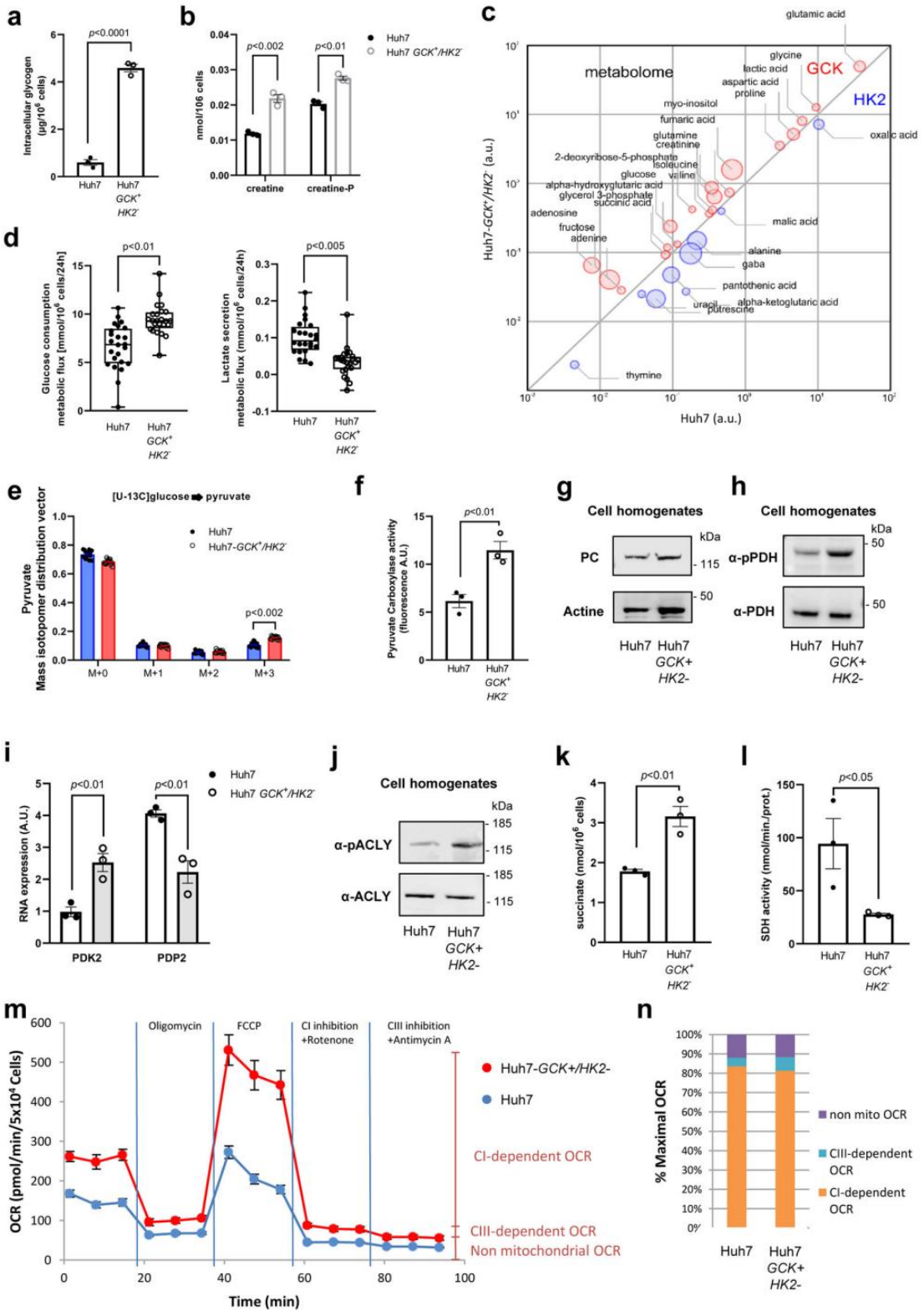
a
b
c
d
e
f
g
h
i
j
k
l
m
n
Intracellular glycogen (µg/10^6 cells)
p<0.0001
Huh7
Huh7 GCK+ HK2-
nmol/106 cells
p<0.002
p<0.01
creatine
creatine-P
Huh7 GCK+/HK2-
metabolome
GCK
HK2
glutamic acid
glycine
lactic acid
aspartic acid
proline
myo-inositol
fumaric acid
glutamine
creatinine
2-deoxyribose-5-phosphate
isoleucine
glucose
valine
alpha-hydroxyglutaric acid
glycerol 3-phosphate
succinic acid
adenosine
fructose
adenine
oxalic acid
malic acid
alanine
gaba
pantothenic acid
uracil
putrescine
alpha-ketoglutaric acid
thymine
Huh7-GCK+/HK2- (a.u.)
Huh7 (a.u.)
Glucose consumption metabolic flux [mmol/10^6 cells/24h]
p<0.01
Lactate secretion metabolic flux (mmol/10^6 cells/24h)
p<0.005
[U-13C]glucose ➡ pyruvate
Pyruvate Mass isotopomer distribution vector
Huh7-GCK+/HK2-
p<0.002
M+0
M+1
M+2
M+3
Pyruvate Carboxylase activity (fluorescence A.U.)
p<0.01
Cell homogenates
kDa
PC
115
Actine
50
α-pPDH
α-PDH
RNA expression (A.U.)
p<0.01
PDK2
PDP2
α-pACLY
α-ACLY
185
succinate (nmol/10^6 cells)
p<0.01
SDH activity (nmol/min./prot.)
p<0.05
OCR (pmol/min/5x10^4 Cells)
Oligomycin
FCCP
CI inhibition +Rotenone
CIII inhibition +Antimycin A
Huh7-GCK+/HK2-
CI-dependent OCR
CIII-dependent OCR
Non mitochondrial OCR
Time (min)
% Maximal OCR
non mito OCR
CIII-dependent OCR
CI-dependent OCR

Figure 4.6. Innate immune response is enhanced in Huh7-*GCK*$^{+}$/*HK2*$^{-}$ cells.

a) Sector chart from the transcriptomic study showing genes included in the GO-term "Type I-IFN signaling pathway".

b) List of genes significantly up-regulated in red or down-regulated in purple (| FC | > 2, BH adjusted *p* value<0.05) in Huh7-*GCK*$^{+}$/*HK2*$^{-}$ compared to Huh7 cells (*n* = 3).

c–e) Cells were stimulated or not for 48 h with 3p-hpRNA (RIG-I ligand) or poly(I:C) (IFIH1/MDA5 ligand). ISRE-luciferase expression was monitored and normalized to Renilla luciferase (**c**, **d**) (*n* = 3 for 3p-hpRNA and *n* = 4 for poly(I:C) treatments). Cell supernatants were assayed for cytokine concentration by multiplex assays (*n* = 3 to 7) (**e**).

f) NK cell mediated lysis of Huh7 or Huh7-*GCK*$^{+}$/*HK2*$^{-}$ cells. Hepatoma cells were seeded 24 h before NK cells addition for 4 h at effector to target (E:T) ratio of 0, 3 or 30. After harvesting, cell lysis was determined by the percentage of PI^{+} cells on gated hepatocytes (*n* = 3). Means ± SEM of indicated *n* independent experiments are presented and p values were obtained from 2-way ANOVA analyses comparing matched cell means with Sidak's correction for multiple comparison, with α = 0.05

a

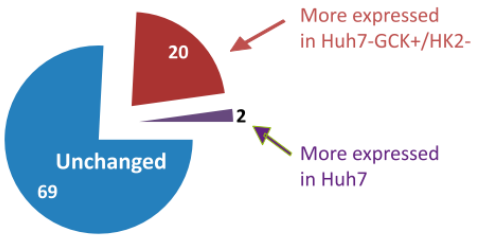

b

Gene ID	Huh7 (mean normalized counts)	Huh7-GCK+/HK2- (mean normalized counts)	FC (calculated by DESeq2 analysis)
EGR1	178,2	537,5	3,0
GBP2	243,0	816,5	3,3
HLA-A	247,2	608,1	2,5
HLA-B	13,4	29,8	2,2
HLA-H	177,8	579,0	3,3
HSP90AB1	0,0	622,9	10000,0
IFI35	50,2	252,5	5,0
IFI6	21,7	142,8	6,6
IFIH1	34,5	106,1	3,1
IFITM3	180,9	1081,4	6,0
IKBKE	0,3	419,4	1284,3
IRF1	212,9	505,2	2,4
IRF3	38,5	84,4	2,2
IRF9	109,3	388,8	3,6
ISG15	89,9	197,6	2,2
MX1	0,0	28,6	10000,0
OAS1	0,8	157,5	173,5
OAS3	195,1	1095,0	5,6
PSMB8	0,0	13,4	80,0
RNASEL	0,0	4,9	10000,0
ABCE1	6559,7	3037,7	-2,2
TRIM6	663,1	263,9	-2,5

c

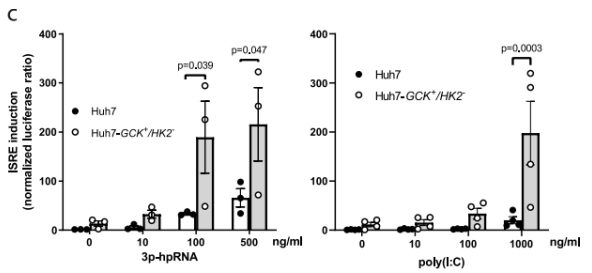

d

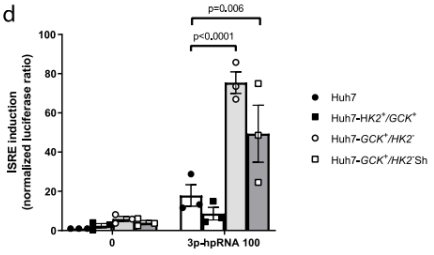

e

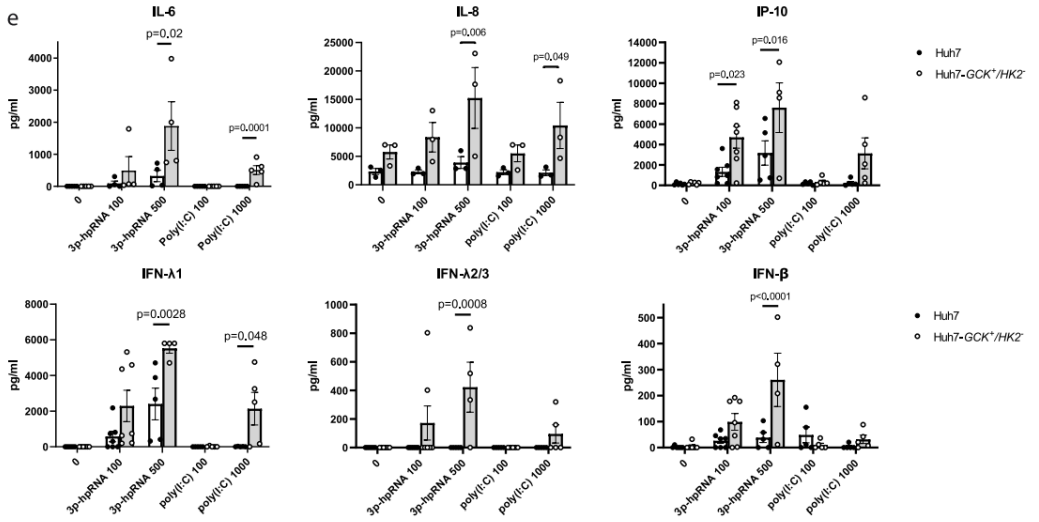

f

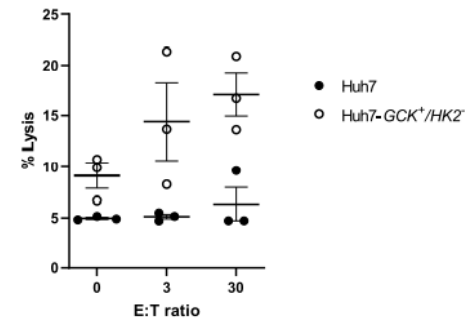

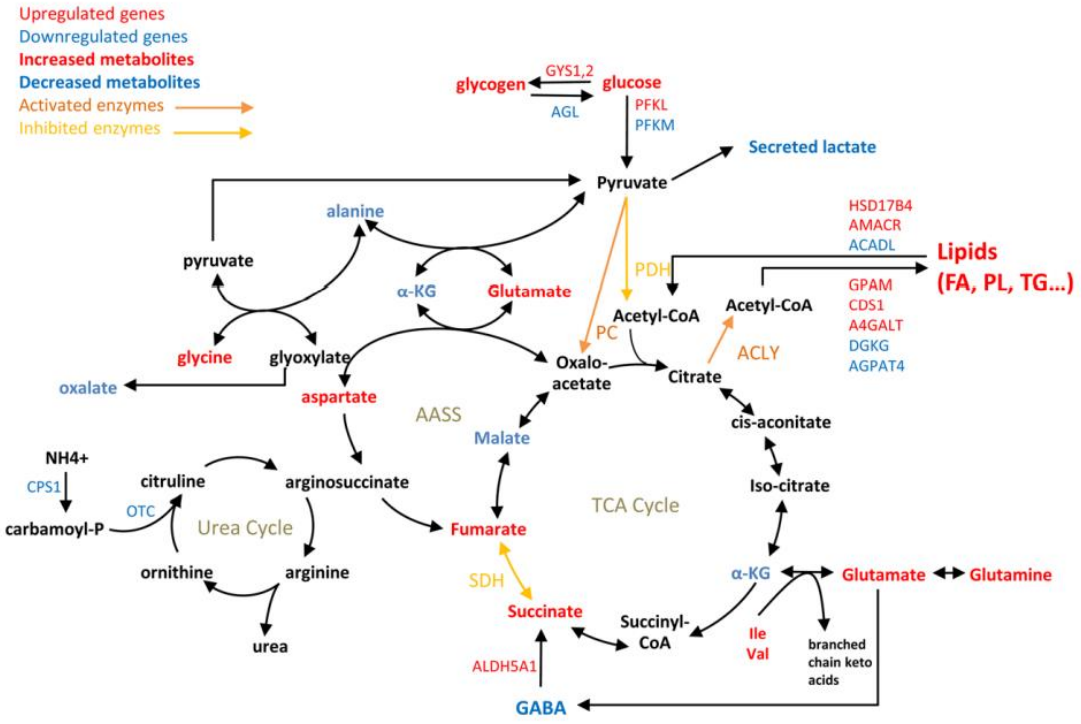

Figure 4.7. Simplified scheme of central carbon metabolism and connected pathways showing differences between Huh7-*GCK*$^{+}$/*HK2*$^{-}$ vs Huh7.

Highlighted metabolites, enzymatic activities, and metabolism-associated genes were selected from transcriptomic (Figure 4.2e), metabolomic (Figure 4.5c) and enzymatic analyses (Figure 4.5f–l).

Table 4.1. Analysis of differentially expressed genes in Huh7 and Huh7-*GCK*$^{+}$/*HK2*$^{-}$ using gene set enrichment analysis (| FC | > 2 with a *p* value <0.05).

Molecular and cellular function*	***p* value range**	**# of genes involved**
Cellular movement	$7.68 \times 10^{-6} – 4.66 \times 10^{-25}$	701
Lipid metabolism	$2.00 \times 10^{-6} – 3.12 \times 10^{-14}$	414
Molecular transport	$5.63 \times 10^{-6} – 3.12 \times 10^{-14}$	361
Small molecule biochemistry	$5.63 \times 10^{-6} – 3.12 \times 10^{-14}$	462
Protein synthesis	$1.87 \times 10^{-6} – 3.42 \times 10^{-14}$	199

*Top-five enriched molecular and cellular functions are presented.

Table 4.2. Top-five ranked IPA-annotations associated to 'cellular movement'.

Cellular movement functional annotations	***p* value**	**# of genes involved**
Migration of cells	4.66×10^{-25}	585
Cell movement	3.48×10^{-24}	642
Cell movement of blood cells	1.52×10^{-18}	276
Leukocyte migration	1.59×10^{-18}	274
Invasion of cells	5.33×10^{-17}	306

Table 4.3. Top-five ranked IPA-annotations associated to 'lipid metabolism'.

Lipid metabolism functional annotations	***p* value**	**# of genes involved**
Concentration of lipid	3.12×10^{-14}	256
Synthesis of lipid	2.37×10^{-10}	233
Fatty acid metabolism	4.31×10^{-10}	166
Quantity of steroid	4.48×10^{-09}	138
Concentration of cholesterol	6.58×10^{-08}	94

Chapter Five: Conclusions

5.1 Summary of contributions

Dysregulated metabolic states in human health are linked to chronic conditions such as diabetes, insulin resistance, cancer, and even chronic obstructive pulmonary disease (COPD)[1]. Additionally, dysregulated metabolism can impair immune function[2], resulting in more severe reactions to acute infection. Studying dysregulated metabolic states is thus a critical aspect in current biomedical research, as an aging population and a rise in emerging infectious diseases (such as COVID-19)[3] mean that the prevention and management of these conditions is more important than ever. However, metabolism is a highly complex physiological phenomenon that is often inextricable in a practical sense from other systems such as immune function or hormone signaling. Therefore, models of altered metabolism are extremely useful for examining the effects of such perturbed metabolic states in comparative isolation, to elucidate the nature, role, and consequences of such states.

The first study of this dissertation explores the use of Northern elephant seals (NES) as a model of insulin resistance. NES undergo temporary, reversible, tissue-specific insulin resistance as a natural component of their life history. Insulin resistance in humans is linked to diabetes, metabolic syndrome, and other chronic conditions, and thus the study of NES may carry implications for all of these.

The second study of this dissertation centers around an engineered cellular model of the hexokinase isoenzyme switch. As hepatocytes transform into hepatocellular carcinoma (HCC) cells during HCC onset and progression, they undergo a shift from HK4 (also known as GCK) to HK2 as the main hexokinase enzyme catalyzing the rate-limiting step in glucose catabolism. To study the effects of the isoenzyme switch, a cellular model was generated by restoring HK4 expression while simultaneously knocking out HK2 in HCC. Such engineered models may be useful in studying very specific metabolic states such as the isoenzyme switch.

In this concluding section, the results from these studies are discussed, along with their use of unique models of metabolism and future directions of study.

5.2 Insulin induces a shift in lipid and primary carbon metabolites in a model of fasting-induced insulin resistance

5.2.1 Summary of results

This study measured plasma concentrations of metabolites over time following insulin infusion in early- and late-fasted Northern elephant seals. Prior research indicated that NES in late fasting displayed elevated plasma levels of free fatty acids (FFA) following glucose-stimulated insulin secretion[4], in contrast to the reduction typically seen in early fasting[5] and mammals in general[6]. This suggested a shift in substrate utilization over the course of the fasting period in

NES. In order to separate the glucose-mediated effects from insulin-mediated effects, the response to direct insulin infusion was studied.

Forty-one plasma metabolites were observed to change significantly in baseline (T_0, pre-infusion) values between the early-fasting group and the late-fasting group. Prolonged fasting was associated with the most profound changes in free fatty acids and ketone bodies, which were dramatically increased in the late-fasted NES.

Conversely, there were mixed changes with other primary metabolites and endocannabinoids (EC). Some, such as primary metabolite 1,5-anhydroglucitol and endocannabinoid anandamide, increased. Several of these elevated metabolites are downstream products of lipid oxidation, providing additional evidence of upregulated lipid oxidation in late fasting. In contrast, endocannabinoid-like DHEA and SEA and glucogenic/ketogenic amino acids alanine, asparagine, cysteine, tryptophan, tyrosine, and valine decreased.

Pathway enrichment analysis of significantly perturbed metabolites ($p<0.05$) indicated 9 biochemical pathways that were significantly deregulated between early and late fasting in seals ($p<0.05$). The most perturbed pathways included ketone and branched-chain amino acid metabolism.

Collectively, the changes in baseline concentrations and pathway analysis demonstrate an increase in fatty acid and ketone pool size, coupled with a decrease in amino acids and primary metabolites in late-fasted seals, indicating that fasting duration shifts substrate metabolism toward an increase in lipolysis, β-oxidation, and ketone metabolism as the primary sources of energy, associated with a robust conservation of protein (lean tissue).

Metabolite concentrations over time following insulin infusion were plotted and the area under the curve (AUC) was calculated as a representation of insulin response. A peak in plasma concentration, followed by a homeostatic return to baseline, is represented by a positive AUC value, while a decrease in plasma concentration in response to insulin infusion returns a negative AUC value. 23 metabolites were observed to have significantly ($p<0.05$) perturbed AUC values between early and late fasting, indicating that fasting duration alters the tissue's responsiveness to insulin.

Fatty acid metabolism in response to insulin is characterized by decreased AUC values between early and late fasting, with all AUC values of FFA in late fasting being negative. The responses of ketones and EC to the insulin infusion were similar, suggesting that lipolytic and endocannabinoid pathways share common insulin-mediated processes. In early fasting, these metabolite levels decreased, reaching a nadir at 30 min post-infusion. For FFA, levels returned to baseline by 60 min and remained so for the rest of the measurement period, whereas ketones and EC peaked at 60 min before returning to baseline at 120 min. Initially, insulin increased primary metabolites and amino acids before levels reached a nadir at 60 min and returned to baseline by 120 min.

In late fasting, FFA and EC decreased similarly, reaching a nadir at 60 min before returning to baseline by 120 min. Ketones displayed a transient increase before a nadir at 60 min and returning to baseline by 120 min. Primary

metabolites and amino acids AUC values increased (with all values being positive except for isoleucine). In contrast to the early fasting response, insulin increased amino acid levels reaching a peak at 60 min before decreasing to baseline at 120 min.

Principal component analysis (PCA) revealed that the maximum geometric distance occurred at 60 min for both early and late fasting, regardless of trajectory. In early fast the majority (72%) of metabolite trajectories return to baseline (+/− 30% of baseline) at 120 min. In contrast, the majority of metabolite concentrations in the late fast (53%) did not return to baseline (+/− 30% of baseline), and present a residual difference at 120 min post-infusion. Collectively, the integrated insulin responses (AUC) and PCA data reveal that in late-fasted animals (characterized by insulin resistance) the available pool of free fatty acids is depleted quickly, and likely shuttled into the TCA cycle. Conversely, the insulin-induced increases in primary metabolites (AUCs) are indicative of activation of gluconeogenic precursors.

Hierarchical clustering identified groups of metabolites with similar trajectories in both early and late fasting as well as in a joined cohort of both early and late fast. The seven main classes of metabolites (amino acids, endocannabinoids, fatty acids, glucose, ketone bodies, organic acids, and primary carbon metabolites) grouped into four distinct clusters in early fasting and four clusters in late fasting. In early fasting, ketone, EC, and TCA cycle metabolite profiles demonstrated a common peak and clustered together. Trajectories for amino acids and primary metabolites were closely related. The FFA profiles were characterized by a rapid, initial decrease recovering by 60 min, which was distinctive from the profiles for amino acids and primary metabolites.

In late fasting, FFA and EC were correlated and clustered together with a decrease at 60 min. A comparison of the metabolomic profiles between early- and late-fasted animals in response to the insulin infusion demonstrated profound shifts in cellular metabolism and biochemical processes as a function of fasting duration. Cluster analysis allowed for assessment of the transition from negative to positive AUC values with fasting duration.

5.2.2 Northern elephant seals as a model of insulin resistance

Insulin resistance is often discussed as a pathological condition associated with metabolic syndrome and type 2 diabetes[7], but it can be temporary and reversible in many mammals. Insulin resistance is often a standard animal response to brief periods of starvation in order to preserve circulating glucose in the absence of a food supply[8]. The examination of the Northern elephant seal in this study elucidates some of the key aspects that make its insulin-resistance-like state unique as exhibited during late fasting. Circulating glucose and FFA levels are elevated, in a manner similar to standard insulin resistance. Likewise, plasma insulin levels are decreased in late fast[9], contributing to the reduction in insulin signaling. As seen in this study, the changes in plasma metabolite concentrations in response to insulin exhibit considerable lag time in late fast, suggesting decreased sensitivity to insulin. However, the tissues still remain responsive to insulin despite the lag time. Additionally, the shift in amino acid plasma concentration response to insulin in late fast indicates a level of protein

catabolism inconsistent with other models of insulin resistance. The increased response of amino acids also suggests that the muscles remain more sensitive to insulin than other tissues such as adipose.

The combined targeted and untargeted metabolomics approach used in this study allowed for the visualization of the dramatic shifts in substrate utilization and insulin response from early to late fast. Although NES rely largely on lipid oxidation for energy during fasting periods, insulin has profound effects on endocannabinoids, ketones, and TCA metabolites, highlighting the extent to which the metabolic network must be remodeled in order to accommodate such fasting periods without lasting deleterious effects. The dynamic effects of insulin on regulating substrate metabolism during fasting, as well as the transient and tissue-specific nature of the insulin-resistant-like state, indicate that the Northern elephant seal can be used to untangle some of the questions about the evolution and regulation of insulin signaling, and provide significant answers to addressing insulin resistance in a clinical context.

The use of engineered cellular models to study insulin resistance is not recommended at present. Much still remains to be understood regarding the genetic regulation of this complex syndrome, in pancreatic cells as well as the various target tissues, so a clear target for knockout is not obvious. The interplay between different organ systems and the implications on whole-body homeostasis mean that insulin resistance is ill-suited to be studied *in vitro*. A model organism such as the Northern elephant seal is a much better system to study the complexity of insulin resistance.

5.2.3 Future perspectives

Northern elephant seals continue to be studied for their uniquely transient state of insulin resistance. This year, studies were published examining oxylipin metabolism[10] and GLP-1 response[11] in late-fasted NES, which have implications for inflammatory signaling and diabetes treatment, respectively.

Animal models, particularly rodents (mice and rats), have long been used to study nutrition and metabolism, including diabetes. However, this approach is not without its limits, as murine physiology differs from humans in a number of ways that can create difficulties in generating useful models or applying the conclusions to human health[12-13]. Generic animal models based on high-calorie diets show significant variation depending on the specific macronutrient profiles of the feed, and may not be generalizable to humans or even comparable to other studies within the field[14]. Thus, there is still a need for useful models of insulin resistance. Swine models see use due to their greater compatibility with human anatomy[15-17]. As noted earlier, the transient and tissue-specific nature of NES insulin resistance sets it apart from other animal models that seek to replicate human biology, and can provide insight into the evolution and regulation of the larger phenomenon of insulin resistance. The fact that NES exhibit insulin resistance as a standard part of their life history means that engineering animal models via techniques such as CRISPR/Cas9 or other, more traditional methods such as artificial selection[18] may be unnecessary, reducing the complexity of any related studies.

5.3 A hexokinase isoenzyme switch in human liver cancer cells promotes lipogenesis and enhances innate immunity

5.3.1 Summary of results

This study focused on the shift in HCC cells from GCK to HK2 as the predominant hexokinase enzyme. Transcriptomic analysis revealed that overexpression of HK2 is negatively correlated with patient survival, as is GCK underexpression; furthermore, the ratio of GCK/HK2 expression outperforms either metric in predicting patient survival. In order to decipher the functional consequences of GCK or HK2 expression in a HCC model, GCK expression was restored by lentiviral transduction in the reference HCC cell line Huh7, and the endogenous *HK2* gene was knocked out by CRISPR/Cas9. The hexokinase activity in the presence of increasing concentration of glucose was determined in protein lysates from the two respective cell lines. The cell proliferation capacity remained identical between the two cell lines. The genome-edited Huh7-*GCK*$^{+}$/*HK2*$^{-}$ and the parental Huh7 cell lines were then compared at a metabolic level.

The intracellular lipid content of the two cell lines was analyzed. In Huh7-*GCK*$^{+}$/*HK2*$^{-}$, an enrichment in phosphatidylcholine, cholesterol, triglycerides (TG) and free fatty acids was observed compared to Huh7. One major function of hepatocytes is to secrete triglyceride-rich VLDL and this function is altered in HCC cells that secrete smaller lipoproteins with the density of LDL. The secretion of lipids and lipoproteins by both cell lines was analyzed after a 24h culture in the absence of fetal calf serum to exclude any participation of exogenous lipids in the production of lipoproteins. Huh7-*GCK*$^{+}$/*HK2*$^{-}$ secreted more free fatty acids than Huh7, while secretion of cholesterol and TG remained unchanged.

However, under the same conditions, the secretion of apolipoprotein B (ApoB) by Huh7-*GCK*$^{+}$/*HK2*$^{-}$ was reduced compared to Huh7. Since ApoB is a non-exchangeable protein with only one copy in VLDL and LDL particles, an elevated TG/ApoB ratio indicates that ApoB^{+}-lipoproteins secreted by Huh7-*GCK*$^{+}$/*HK2*$^{-}$ cells are enriched in TG compared to those secreted by Huh7. This was confirmed by the ApoB distribution in density gradient fractions. As expected, lipoproteins secreted by Huh7 sediment at the density of LDL, while those secreted by Huh7-*GCK*$^{+}$/*HK2*$^{-}$ match the density of VLDL found in human plasma or secreted by primary human hepatocytes in culture. This indicates that GCK expression is essential for the VLDL assembly/secretion pathway and could explain the loss of this crucial metabolic pathway in hepatoma cells expressing HK2 instead of GCK.

GCK expression was observed to increase the intracellular lipid content, resulting in accumulation of lipid droplets and secretion of VLDL. A rewiring of cellular metabolism towards energy storage in Huh7-*GCK*$^{+}$/*HK2*$^{-}$ was thus suspected and confirmed by the accumulation of glycogen, creatine and creatine-P, a feature of functional hepatocytes. To further determine the consequences of replacing HK2 by GCK, we quantified prominent intracellular

metabolites via gas chromatography coupled to triple-quadrupole (QQQ) mass spectrometry (GC-MS). Relative intracellular quantities of metabolites are significantly different between Huh7 and Huh7-*GCK*$^{+}$/*HK2*$^{-}$. Among differentially represented metabolites, higher levels of glucose, glycerol-3-phosphate and lactic acid were detected in Huh7-*GCK*$^{+}$/*HK2*$^{-}$ cells. Several intermediates of the TCA cycle (succinic acid, fumaric acid, alpha-ketoglutaric acid), and metabolites directly connected to it (GABA, glutamic acid, glutamine, aspartic acid) were also differentially present between the two cell lines. This supports a modulation of central carbon metabolism at both the level of glycolysis and TCA cycle. This led to investigate glucose catabolism in further details. Glucose consumption and stable isotope incorporation from [U-^{13}C]-glucose into pyruvate were both increased in Huh7-*GCK*$^{+}$/*HK2*$^{-}$ compared to Huh7 cells. This increased glycolytic flux together with a reduced lactate secretion is likely to account for the elevation of lactate levels and suggest that the increased pyruvate production essentially fuels mitochondrial TCA cycle in Huh7-*GCK*$^{+}$/*HK2*$^{-}$ cells.

Pyruvate entering the mitochondria downstream of glycolysis can be either oxidized by pyruvate dehydrogenase (PDH), producing acetyl-CoA, or converted into oxaloacetate (OAA) by pyruvate carboxylase (PC). Acetyl-CoA and OAA are then combined in the TCA cycle to form citrate. *De novo* lipogenesis requires citrate egress from the TCA cycle to serve as a precursor of cytosolic acetyl-CoA for further synthesis of fatty acids. In Huh7-*GCK*$^{+}$/*HK2*$^{-}$ cells, we observed both an increased activity of PC without changes in protein expression and an increased phosphorylation of pyruvate dehydrogenase (PDH), which is indicative of a reduced activity of this enzyme. This is consistent with the increased expression of the PDH kinase PDK2 and the decreased expression of the PDH phosphatase PDP2 in Huh7-*GCK*$^{+}$/*HK2*$^{-}$ cells that regulate the PDH phosphorylation state. A rebalanced usage of pyruvate in Huh7-*GCK*$^{+}$/*HK2*$^{-}$ cells maintains a functional TCA cycle and supports lipogenesis. In Huh7-*GCK*$^{+}$/*HK2*$^{-}$ cells, we also observed an increased phosphorylation of ATP citrate lyase (ACLY), the first enzyme of the fatty acid synthesis pathway, indicating an enhanced activity of this enzyme. This reaction also regenerates OAA in the cytosolic compartment. Interestingly, transcriptomic data show that PCK1 which converts OAA to phosphoenolpyruvate (PEP), is overexpressed in Huh7-*GCK*$^{+}$/*HK2*$^{-}$ cells compared to Huh7 (FC = 32).

A shift from pyruvate oxidation to carboxylation is observed in cancer cells where succinate dehydrogenase (SDH) is inactivated by mutation and OAA can only be generated through PC activity. SDH inhibition leads to succinate accumulation, especially in activated immune cells. Interestingly, higher levels of succinate and a reduced activity of SDH were measured in Huh7-*GCK*$^{+}$/*HK2*$^{-}$ compared to Huh7 cells. Even though SDH is also part of the complex II of the mitochondrial respiratory chain, we observed that the overall oxygen consumption was increased in Huh7-*GCK*$^{+}$/*HK2*$^{-}$ with increased basal and maximal respiration, ATP production and spare respiration capacity. Functional analysis of the respiratory chain showed that oxygen consumption in Huh7 and Huh7-*GCK*$^{+}$/*HK2*$^{-}$ cells was mainly dependent on complex I activity. Thereby, the HK isoenzyme switch rewired the TCA cycle promoting carboxylation of

pyruvate into OAA in the presence of a reduced SDH activity and increased respiration through complex I.

5.3.2 Engineering cellular models of dysregulated metabolism

Metabolism, by its nature, is a tightly interconnected process, with any one pathway intersecting with many others. Metabolic pathways are not segregated by function; bioenergetic pathways are connected to other pathways involved in biosynthesis, signaling, immune function, gene regulation, and more. As a consequence, isolating specific metabolic phenomena or reactions for study is difficult if not impossible to do in a practical sense.

The rise in molecular biology techniques, especially the CRISPR/Cas9 system, to selectively edit cellular genomes has opened the door to a new era in customizable cellular models. Specific genes can be activated or inactivated with precision, including metabolic enzymes. Such unique cellular models would have taken vastly more time or resources to generate via traditional methods. The ability to use targeted, custom cell lines means that the function of an individual enzyme can be separated from confounding effects such as upstream regulation or substrate availability, greatly reducing the number of variables under study.

The cell model used in this study is the result of two different molecular biology techniques. First, Huh7 cells (a reference HCC cell line) were transduced with a lentiviral vector carrying the GCK gene to induce stable GCK expression. The Huh7-*GCK*$^{+}$ cells were then transfected with a plasmid containing the Cas9 gene and a sgRNA sequence specific to HK2, which knocked out the HK2 gene in the Huh7 cells, resulting in the unique cell line Huh7-*GCK*$^{+}$/*HK2*$^{-}$. This cell line represents a reversal of the hexokinase isoenzyme switch seen in hepatocytes as they transition to HCC cells. Based on transcriptomic data, the ratio of GCK to HK2 expression was the best predictor of patient survival when studying the hexokinase family, so a double-transfection cell line was desired in order to study the role of the isoenzyme switch. The generation of such a double-transfection cellular model increases the complexity of the method: each transfection or transduction event must have its own selection (puromycin resistance and transient GFP expression, in this case) and must be validated separately to ensure that each step is effective. However, with modern molecular biology techniques, the specificity and customizability of cellular models available today represent an immense leap forward from the technical landscape of even a decade prior.

There are multiple strategies for generating custom cellular models. CRISPR/Cas9[19] is the new standard for genome editing, given its ease of use, but zinc-finger nucleases and transcription activator-like effector nucleases (TALENs) still remain viable strategies as well[20]. Knockdown via RNAi (using lentiviral transduction) is also widely used for creating stable cell lines with a given expression phenotype[21].

The use of a model organism to study this particular phenotype is difficult. The fact that the hexokinase isoenzyme switch has such far-ranging effects means that there are many selection pressures and points of interaction with this

simple mutation. While aspects of the hexokinase switch may be elucidated with a broader physiological context, including the tumor microenvironment and further interplay with the immune system, the number of changing variables in the system rises dramatically, increasing the methodological complexity of any experiment. Engineered cellular models are an elegant solution to replicate, observe, and interact with simple and specific perturbations to the metabolic network.

5.3.3 Future perspectives

There are other emerging platforms as well to better study dysregulated metabolism. Mathematical modeling is a powerful approach, able to generate multiple permutations of a metabolic network with various fluxes and highlight potential novel targets for study[22-24]. However, computational models depend on biological elucidation of metabolic networks; without a baseline understanding of the system in question, no model can be generated, and so *in vivo* or *in vitro* models must still be investigated first.

On the topic of the hexokinase isoenzyme switch, there is ongoing work to uncover precisely how HK2 is upregulated in HCC, with current evidence pointing towards nuclear receptor PPARγ[25] and kinases PI3K and Akt[26]. The mechanisms that concomitantly suppress GCK are not fully known.

Other instances of isoenzyme switches are worth investigating. The pyruvate kinase isoform PKM2 is highly upregulated in cancers compared to its splice variant PKM1, and there is evidence this exhibits an isoform switch in specific tissues[27-28], though there are alternate theories[29]. An engineered cellular model of such a hypothetical switch may shed more light on the interplay between the different pyruvate kinase isoforms.

5.4 Conclusions

These studies exhibit two different approaches to cultivating useful model systems in which to study dysregulated metabolism: identifying existing models in nature of organisms with unique metabolic states, parallel to the states under study; and engineering a model specific to the question at hand using molecular biology techniques. Either approach has its advantages, disadvantages, and areas of applicability.

Existing animal models of unique metabolic states has the benefit of simplicity, bypassing the need for technical benchtop approaches that carry the possibility of human error; however, they may not be exact matches for the desired human metabolic state, and care must be taken to not overemphasize their clinical relevance. Additionally, finding such unique animal models in the first place may be challenging, and is certainly not a high-throughput process.

Engineered cellular models offer precision and customizability, as they can be generated and tailored to a specific problem, but are paired with a rise in methodological complexity. Furthermore, *in vitro* systems (as molecular biology techniques are commonly applied) are less applicable than *in vivo* systems, lacking the context of full physiology. *In vitro* cancer studies such as that

described in Chapter Four, for example, do not include the effect of the tumor microenvironment, which has a profound role in carcinogenesis.

Another approach not fully discussed in this dissertation is the use of *in silico* models to describe a metabolic network, along with its permutations and fluxes. These and other model systems must be carefully weighed to determine the best method of replicating a dysregulated metabolic state for study.

5.5 References

1. Chen H, Li Z, Dong L, Wu Y, Shen H, Chen Z. Lipid metabolism in chronic obstructive pulmonary disease. *Int J Chron Obstruct Pulmon Dis*. 2019;14:1009-1018. PMID: 31190786.

2. Daryabor G, Atashzar MR, Kabelitz D, Meri S, Kalantar K. The effects of type 2 diabetes mellitus on organ metabolism and the immune system. *Front Immunol*. 2020;11:1582. PMID: 32793223.

3. Morens DM, Fauci AS. Emerging pandemic diseases: How we got to COVID-19. *Cell*. 2020;182(5):1077-1092. PMID: 32846157.

4. Viscarra JA, Vázquez-Medina J, Rodriguez R, et al. Decreased expression of adipose CD36 and FATP1 are associated with increased plasma non-esterified fatty acids during prolonged fasting in Northern elephant seal pups (*Mirounga angustirostris*). *J Exp Biol*. 2012;215(Pt 14):2455-64. PMID: 22723485.

5. Viscarra JA, Champagne CD, Crocker DE, Ortiz RM. 5'AMP-activated protein kinase activity is increased in adipose tissue of Northern elephant seal pups during prolonged fasting-induced insulin resistance. *J Endocrinol*. 2011;209(3):317-325. PMID: 21429964.

6. Karpe F, Dickmann J, Frayn KN. Fatty acids, obesity, and insulin resistance: time for a reevaluation. *Diabetes*. 2011;60(10):2441-9. PMID: 21948998.

7. Meshkani R, Adeli K. Hepatic insulin resistance, metabolic syndrome and cardiovascular disease. *Clin Biochem*. 2009;42(13-14):1331-46. PMID: 19501581.

8. Newman WP, Brodows RG. Insulin action during acute starvation: evidence for selective insulin resistance in normal man. *Metab*. 1983;32(6):590-6. PMID: 634177.

9. Ortiz RM, Noren DP, Ortiz CL, Talamantes F. GH and ghrelin increase with fasting in a naturally adapted species, the Northern elephant seal (*Mirounga angustirostris*). *J Endocrinol*. 2003;178(3):533-9. PMID: 12967344.

10. Wright DN, Katundu KGH, Viscarra JA, et al. Oxylipin responses to fasting and insulin infusion in a large mammalian model of fasting-induced insulin resistance, the Northern elephant seal. *Am J Physiol Regul Integr Comp Physiol*. 2021;321(4):R537-R546. PMID: 34346724.

11. Dhillon J, Viscarra JA, Newman JW, Fiehn O, Crocker DE, Ortiz RM. Exogenous GLP-1 stimulates TCA cycle and suppresses gluconeogenesis and ketogenesis in late-fasted Northern elephant seals pups. *Am J Physiol Regul Integr Comp Physiol*. 2021;320(4):R393-R403. PMID: 33407018.

12. Guo, S. Insulin signaling, resistance, and the metabolic syndrome: insights from mouse models into disease mechanisms. *J Endocrinol*. 2014;220(2):T1-T23. PMID: 24281010.

13. Azushima K, Gurley SB, Coffman TM. Modelling diabetic nephropathy in mice. *Nat Rev Nephrol*. 2017;14(1):48-56. PMID: 29062142.

14. Small L, Brandon AE, Turner N, Cooney GJ. Modeling insulin resistance in rodents by alterations in diet: what have high-fat and high-calorie diets revealed? *Am J Physiol Endocrinol Metab*. 2018;314(3):E251-E265. PMID: 29118016.

15. Bellinger DA, Merricks EP, Nichols TC. Swine models of type 2 diabetes mellitus: insulin resistance, glucose tolerance, and cardiovascular complications. *ILAR J*. 2006;47(3):243-58. PMID: 16804199.

16. Westover AJ, Johnston KA, Buffington DA, Humes HD. An immunomodulatory device improves insulin resistance in obese porcine model of metabolic syndrome. *J Diabetes Res*. 2016;2016:3486727. PMID: 27819007.

17. Malbert C-H, Horowitz M, Young RL. Low-calorie sweeteners augment tissue-specific insulin sensitivity in a large animal model of obesity. *Eur J Nucl Med Mol Imaging*. 2019;46(11):2380-2391. PMID: 31338548.

18. Peterson RG, Jackson CV, Zimmerman K, de Winter W, Huebert N, Hansen MK. Characterization of the ZDSD rat: a translational model for the study of metabolic syndrome and type 2 diabetes. *J Diabetes Res.* 2015;2015:487816. PMID: 25961053.

19. Ran FA, Hsu PD, Wright J, Agarwala V, Scott DA, Zhang F. Genome editing using the CRISPR-Cas9 system. *Nat Protoc*. 2013;8(11):2281-2308. PMID: 24157548.

20. Zhang H, Zhang Y, Yin H. Genome editing with mRNA encoding ZFN, TALEN, and Cas9. *Mol Ther*. 2019;27(4):735-746. PMID: 30803822.

21. Geiling B, Vandal G, Posner AR, et al. A modular lentiviral and retroviral construction system to rapidly generate vectors for gene expression and gene knockdown *in vitro* and *in vivo*. *PLoS One*. 2013;8(10):e76279. PMID: 24146852.

22. Lewis NE, Abdel-Haleem AM. The evolution of genome-scale models of cancer metabolism. *Front Physiol*. 2013;4:237. PMID: 24027532.

23. Sharma AK, König R. Metabolic network modeling approaches for investigating the "hungry cancer". *Semin Cancer Biol*. 2013;23(4):227-34. PMID: 23680724.

24. Yilmaz LS, Walhout AJ. Metabolic network modeling with model organisms. *Curr Opin Chem Biol*. 2017;36:32-39. PMID: 28088694.

25. Panasyuk G, Espeillac C, Chauvin C, et al. PPARγ contributes to PKM2 and HK2 expression in fatty liver. *Nat Commun*. 2012;3:672. PMID: 22334075.

26. Roberts DJ, Miyamoto S. Hexokinase II integrates energy metabolism and cellular protection: Akting on mitochondria and TORCing to autophagy. *Cell Death Differ*. 2015;22(2):248-57. PMID: 25323588.

27. Desai S, Ding M, Wang B, et al. Tissue-specific isoform switch and DNA hypomethylation of the pyruvate kinase PKM gene in human cancers. *Oncotarget*. 2014;5(18):8202-10. PMID: 24077665.

28. Williams, AL, Khadka V, Tang M, et al. HIF1 mediates a switch in pyruvate kinase isoforms after myocardial infarction." *Physiol Genomics*. 2018;50(7):479-494. PMID: 29652636.

29. Zhan C, Yan L, Wang L, et al. Isoform switch of pyruvate kinase M1 indeed occurs but not to pyruvate kinase M2 in human tumorigenesis. *PLoS One*. 2015;10(3):e0118663. PMID: 25738776.